Registration of Magnetic Resonance and Ultrasound Images for Guiding Prostate Cancer Interventions

HU, Yipeng

A dissertation submitted in partial fulfilment of the requirement for the degree of Doctor of Philosophy

Centre for Medical Image Computing

Department of Medical Physics and Bioengineering

University College London

2013

I, Yipeng Hu, confirm that the work presented in this thesis is my own. Where information has been derived from other sources, I confirm that this has been indicated in the thesis.

Abstract

Prostate cancer is a major international health problem with a large and rising incidence in many parts of the world. Transrectal ultrasound (TRUS) imaging is used routinely to guide surgical procedures, such as needle biopsy and a number of minimally-invasive therapies, but its limited ability to visualise prostate cancer is widely recognised. Magnetic resonance (MR) imaging techniques, on the other hand, have recently been developed that can provide clinically useful diagnostic information. Registration (or alignment) of MR and TRUS images during TRUS-guided surgical interventions potentially provides a cost-effective approach to augment TRUS images with clinically useful, MR-derived information (for example, tumour location, shape and size).

This thesis describes a deformable image registration framework that enables automatic and/or semi-automatic alignment of MR and 3D TRUS images of the prostate gland. The method combines two technical developments in the field: First, a method for constructing patient-specific statistical shape models of prostate motion/deformation, based on learning from finite element simulations of gland motion using geometric data from a preoperative MR image, is proposed. Second, a novel "model-to-image" registration framework is developed to register this statistical shape model automatically to an intraoperative TRUS image. This registration approach is implemented using a novel model-to-image vector alignment (MIVA) algorithm, which maximises the likelihood of a particular instance of a statistical shape model given a voxel-intensity-based feature vector that represents an estimate of the surface normal vectors at the boundary of the organ in question.

Using real patient data, the MR-TRUS registration accuracy of the new algorithm is validated using intra-prostatic anatomical landmarks. A rigorous and extensive validation analysis is also provided for assessing the image registration experiments. The final target registration error after performing 100 MR–TRUS registrations for each patient have a median of 2.40 mm, meaning that over 93% registrations may successfully hit the target representing a clinically significant lesion. The implemented registration algorithms took less than 30 seconds and 2 minutes for manually defined point- and normal vector features, respectively. The thesis concludes with a summary of potential applications and future research directions.

Acknowledgements

Much joy in writing this thesis comes from counting the people who helped during the past five years. I feel sorry but equally thrilled to find out the name list is too long to complete here. I wish it is a compliment to those who have been left out due to the fact that their contributions were made in such a humble fashion.

Firstly, I am grateful to my supervisor Dr Dean Barratt, for his long lasting support in every possible aspect, from equation derivations to sci-fi film recommendations. His featherweight yet meticulous style of supervision, rigorous attitude in science, and the ability to switch between trained and unconventional thinking have been valuable assets during the course and are likely to play an important role in my future life. I am also grateful that my secondary supervisor Professor David Hawkes who has provided continuous, easily available advice and help throughout the period of my PhD.

I would like to thank a passionate clinical team in University College London Hospital, including Professor Mark Emberton, Mr Hashim Uddin Ahmed, Dr Clare Allen, Dr Caroline Moore, Dr Nim Arumainayagam, Dr Emilie Lecornet, Miss Louise Dickinson, Dr Lucy Simmons and Dr Alex Freeman. All of them have been nothing but encouraging, supportive and helpful. This thesis was motivated and has been continuously adapted following invaluable input from our clinical collaborators.

It is a great privilege to work among many bright and warm-hearted colleagues and fellow PhD students in the UCL Centre for Medical Image Computing and Department of Medical Physics and Bioengineering. In particular, Dr Zeike Taylor, Dr Xiahai Zhuang and Daniel Heanes contributed countless discussion hours. I only consider myself fortunate because I have had the opportunity to work with Dr Tim Carter, Dr Freddy Odille, Dr Erik-Jan Rijkhorst, Dr Baptiste Allain, Dr Christine Tanner, who are now making contributions to science somewhere else and to education in the case of Tim. I am also indebted to those who are still in UCL, Dr Gerard Ridgway, Dr Marc Modat, Dr Mingxing Hu, Dr Steve Thompson, Professor Sebastien Ourselin, Dr Jamie McClelland, Stian Johnsen, Pankaj Daga, Holger Roth, Valentin Hamy, Tom Hampshire and my career mentor Dr John Hipwell. Many other people in the department have kindly lent their helping hands without hesitation. A special thank you is to Daniel, Holger, Steve and Tom for proofreading my thesis chapters.

I have enjoyed an opportunity to lecture, which complements my scientific research experience, thanks to the help from Professor Jeremy Hebden and Professor Robert Speller, Dr Jamie Harle,

Dr Adam Gibson and, again, from Dean. I also enjoyed my years spent in Centre for Advanced Biomedical Imaging, a place full of good energy, although collaborations were mainly established on football pitches with the likes of Dr Jack Wells and Raj Ramasawmy.

I am also obliged to thank Dr Graeme Penney from King's College London, Dr David Atkinson from UCL, Dr Philip "Eddie" Edwards from Imperial College London and Professor Nassir Navab at Technical University of Munich for their constructive and inspiring discussions and suggestions during my transfer and final viva exams.

Like his other colleagues and friends, I have special memories of the late Dr Philip Batchelor and I deeply regret that there was never enough time to co-author a publication with him before he passed away after quite some pencil-and-paper work together.

I acknowledge the following funding sources which have supported, directly or indirectly, my PhD course: a UCL/UCLH Comprehensive Biomedical Research Centre - NIHR project, the Royal Academy of Engineering, the EPSRC, the UCL Study Assistance Scheme, the UCL Studentship and the Prostate Cancer UK (previously, Prostate Cancer Charity).

Last but certainly not least, I would like to dedicate this thesis to my friend Alvaro, my parents and my fiancée Angela for things one cannot put into words.

Biographical Note

Yipeng Hu obtained his BEng (2005) in Biomedical Engineering and MSc (2007) in Biomedical Engineering and Medical Imaging from Sichuan University and University College London (UCL), respectively. He has joined Centre for Medical Image Computing (CMIC), Department of Medical Physics and Bioengineering, UCL, to pursue a PhD degree since 2007. One year later, he was appointed as Research Assistant in CMIC and continued his PhD course as a part-time student in UCL. Part of the work described in this thesis has been presented in the following publications during the course of his PhD.

Selected journal publications

Y. Hu, H. U. Ahmed, Z. Taylor, C. Allen, M. Emberton, D. Hawkes, and D. Barratt, "MR to Ultrasound Registration for Image-guided Prostate Interventions," *Medical Image Analysis*, 16 (3): 687-703. 2012

Y. Hu, T. Carter, H. Ahmed, M. Emberton, C. Allen, D. Hawkes, and D. Barratt, "Modelling Prostate Motion for Data Fusion during Image-guided Interventions," *Medical Imaging, IEEE Transactions on*, 30 (11): 1887-1900. 2011

Y. Hu, R. van den Boom, T. Carter, Z. Taylor, D. Hawkes, H. U. Ahmed, M. Emberton, C. Allen, and D. Barratt, "A Comparison of the Accuracy of Statistical Models of Prostate Motion Trained using Data from Biomechanical Simulations," *Progress in Biophysics and Molecular Biology*, 103 (2-3): 262-272. 2010

Selected peer-reviewed conference papers

Y. Hu and D. Barratt, "Learning Patient-specific Motion based on Decomposing a Multilinear Shape Model," in *CMBE2011* (*2nd International Conference on Mathematical and Computational Biomedical Engineering),* 237-240. 2011

Y. Hu, E.-J. Rijkhorst, R. Manber, D. Hawkes, and D. Barratt, "Deformable Vessel-based Registration using Landmark-guided Cohenrent Point Drift," in *Medical Imaging and Augmented Reality 2010,* LNCS 6326, 20-29, 2010

Y. Hu, H. U. Ahmed, D. Pendsé, M. Sahu, C. Allen, M. Emberton, and D. &. B. D. Hawkes, "MR to Ultrasound Image Registration for Guiding Prostate Biopsy and Interventions," in *MICCAI 2009*, LNCS 5761, 787-794 , 2009

Y. Hu, D. Morgan, H. Ahmed, D. Pendsé, M. Sahu, C. Allen, M. Emberton, and D. &. B. D. Hawkes, "Modelling Prostate Gland Motion for Image-guided Interventions," in *Biomedical Simulation,* LNCS 5104, 79-88, 2008

Y. Hu, D. Morgan, H. U. Ahmed, D. Pendsé, M. Sahu, C. Allen, M. Emberton, and D. &. B. D. Hawkes, "A Statistical Motion Model based on Biomechanical Simulations for Data Fusion during Image-guided Prostate Interventions," in *MICCAI 2008,* LNCS 5241, 737-744, 2008

Patent applications

D. Barratt and **Y. Hu**. Apparatus and Method for Registering Two Medical Images. *UK Patent Application* GB2010 / 001480, 2011

Table of Contents

List of Figures

List of Tables

Chapter 1 Background - Prostate Cancer and Imaging

1.1 Anatomy of Prostate

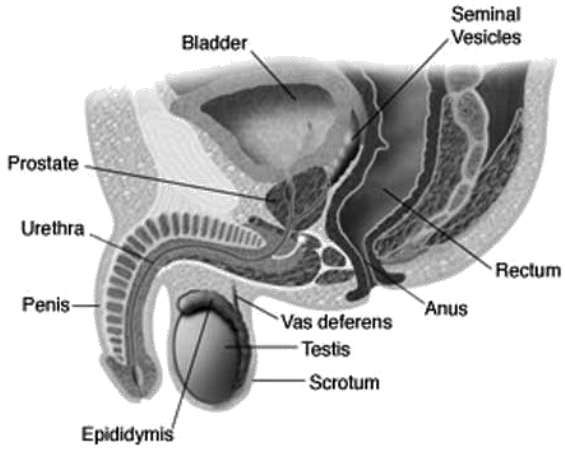

Figure 1.1 Gross anatomy of prostate gland

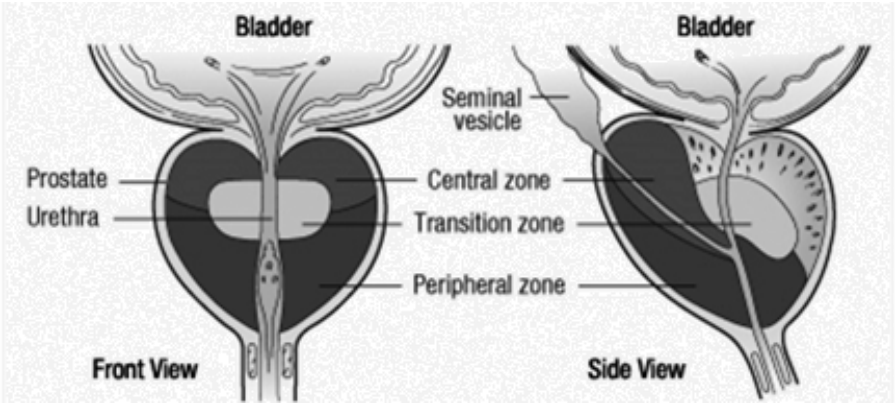

Figure 1.2 The zonal anatomy of prostate gland

The prostate gland is an organ located between urinary bladder and rectum and is only found in men. The main function of the prostate gland is to secrete a slightly acidic prostatic fluid, that constitutes 50-70% of the volume of the semen (Huggins et al. 1942). It surrounds the urethra and is located on the midline in humans (see Figure 1.1). The prostate gland comprises different zones (McNeal et al. 1988): the peripheral zone, the central zone, the transition zone and the anterior fibro-muscular zone (see Figure 1.2). The seminal vesicles and vasa deferens are paired structures on either side of the midline just above the prostate. These extend cranially to the prostate and posteriorly to the bladder, and provide important spatial indication relative to the prostate gland (Halpern et al. 2002). These structures together form a relatively well-defined

anatomical overview of prostate gland that is visible in medical images, particularly MR images. More details of the imaging-related anatomy are discussed in Section 1.3.

Although interpretations from imaging methods, such as MR, correspond to the anatomical description, the precise anatomy of prostate, in particular, local zones within the gland, may not be visualised with all conventional imaging techniques. For example, in ultrasound images, inner gland and outer gland are used to describe the two parts of the prostate within surgical capsule and outside of the surgical capsule. The inner gland contains periurethral tissue and transition zone, while the outer gland is comprised of central- and peripheral zones. Therefore, it could be confusing to the untrained eye in the way that the inner- and outer glands are wrongly considered sometimes as central- and peripheral zones, respectively.

1.2 Prostate Cancer

Prostate cancer is a major health problem internationally, but in particular, in countries in the Western World. The USA, Australia, New Zealand, and Western and Northern Europe (including the UK), have experienced large and rising incidences of prostate cancer. The latest available statistics indicated that prostate cancer is the second most common cause of death among men, after lung cancer in the UK. It accounts for around 13% of male deaths from cancer, 10,721 in 2010 (General Register Office for Scotland 2010;Northern Ireland Statistics and Research Agency 2010;Office for National Statistics Mortality Statistics 2011). In the USA, it is estimated that, in 2012, there were 241,740 new cases of prostate cancer and 28,170 deaths caused by prostate cancer (National Cancer Institute 2012). Furthermore, in several parts of Asia, a changing demography of prostate cancer has been observed, towards significantly rising incidence rate, which is exemplified by data from Singapore and Japan (Sim et al. 2005).

1.2.1 Prostate Cancer Diagnosis

Due to the limitations of the non-invasive diagnosis methods, histopathological analysis of tissue samples remains the gold standard for detection and staging of prostate cancer (Djavan et al. 2007). The clinical method for acquiring tissue samples is needle biopsy. In this procedure, a number of biopsy needles penetrate either the perineum or the rectal wall in order to reach the prostate gland. The *transrectal* biopsy usually is performed “freehand” with the patient in the lateral position and the needle attached to the probe using a needle guide (see Figure 1.3), whereas *transperineal* biopsy is usually performed with the patient in the lithotomy position. In

this case, needles are inserted using a template grid attached to a rigid support device, which also holds the ultrasound probe (see Figure 1.4). Template-guided, transperineal biopsy, in which more than twenty samples are usually collected, although more invasive, has been proposed to provide a better diagnostic ability due to its ability to map cancer with accuracy. (Ahmed et al. 2011;Barzell et al. 2007).

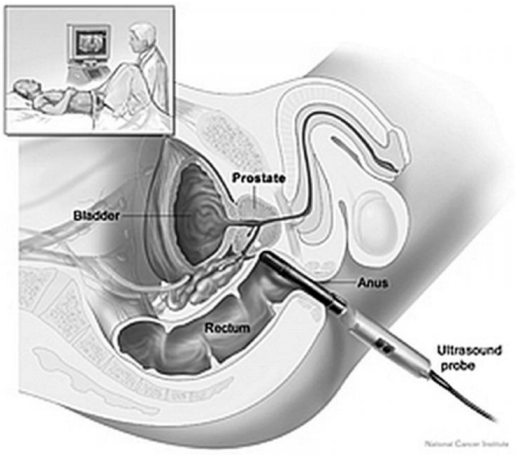

Figure 1.3 An illustration of a TRUS-guided freehand biopsy

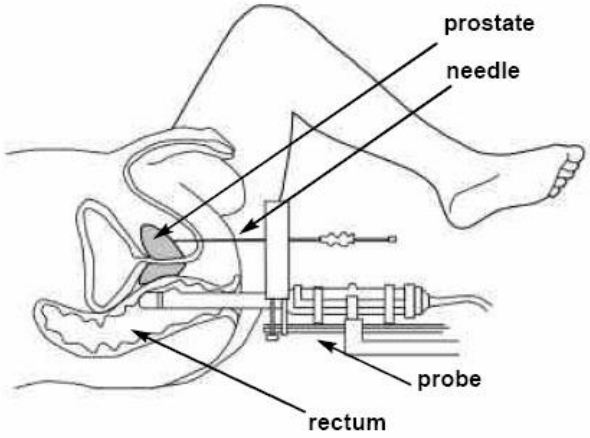

Figure 1.4 An illustration of a TRUS-guided template biopsy, where the biopsy needle goes through the template that is parallel to the patient's perinea. The template, illustrated as a block attached to the TRUS probe, provides relative location information.

All prostate biopsy procedures are performed under the guidance of transrectal ultrasound (TRUS). The proximity of the prostate to the rectal wall means that TRUS is an effective method for guiding prostate biopsy (as well as other minimally-invasive interventional procedures). TRUS provides real-time images of the prostate gland and the surrounding soft tissue, as well as the surgical instruments (see Figure 1.5).

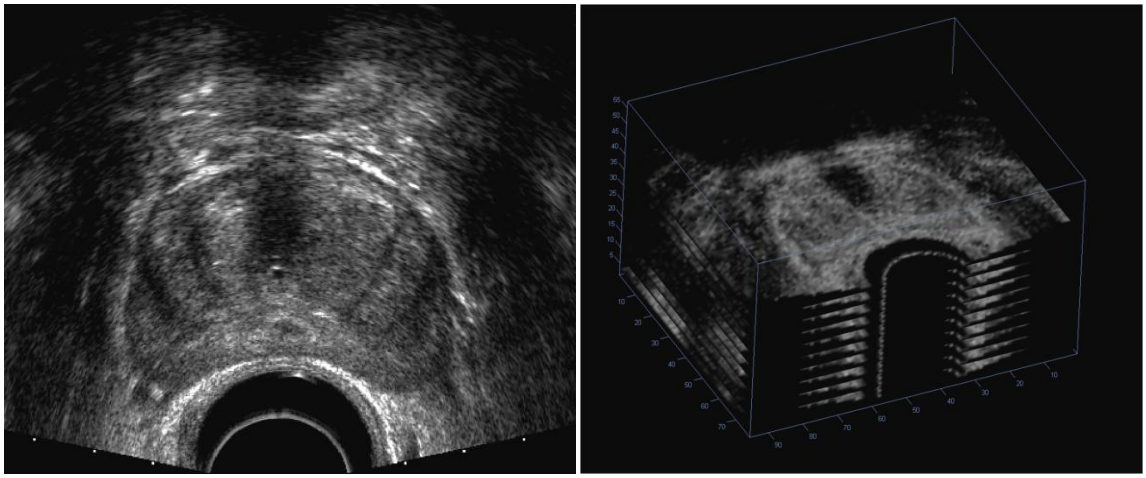

Figure 1.5 Example of a 2D B-mode TRUS image (left) and slices of a 3D TRUS volume (right)

Combined with other clinical factors, such as prostate-specific antigen (PSA) level, age and imaging findings, such as X-ray, magnetic resonance imaging (MRI), computed tomography (CT), positron emission tomography (PET), clinicians are able to detect, grade and stage the prostate cancer.

Recently, there has been increasing interest in imaging methods for diagnosing of prostate cancer, in particular, multi-parametric MRI (e.g. a combination of diffusion-weighted-, dynamic enhanced- and t2-weighted sequences), MR and ultrasound elastography, ultrasound imaging with micro-bubble contrast agents and radio frequency (RF) ultrasound image analysis. These developments are discussed in the Section 1.3.

1.2.2 Prostate Cancer Treatment

Prostate cancer has been found to respond to different treatment options. Which treatments should be recommended to a particular patient remains an open question (Heidenreich et al. 2008;Wilt et al. 2008). From a historical point of view, androgen (hormonal) therapy, radical prostatectomy surgery, radiation therapy (external beam or brachytherapy by implanting radioactive seeds), cytotoxic chemotherapy (Denmeade et al. 2002) and active surveillance (Klotz 2005) have all been adopted in clinical practice, especially for localised cancer. Importantly, thanks to the improvements of diagnostic techniques and the PSA screening, the prostate cancer may be detected at an early stage when it is still confined to the prostate and is potentially curable by surgery and/or whole gland radiation therapy (Denmeade et al. 2002). In addition to curative treatment, good palliative treatment is also important for patient welfare in the advanced stages (Tompson et al. 2007).

A major limitation of radical prostatectomy and other "whole gland" treatments is the risk of serious side-effects, such as incontinence, impotence and damage to the rectum. More recently, a number of alternative minimally-invasive therapies have emerged. For example, high-dose-rate brachytherapy, high intensity focused ultrasound (HIFU), cryotherapy, intensity-modulated radiotherapy and photodynamic therapy (Aus 2006;Marberger et al. 2008). Many of these techniques are well-suited to partial treatment of localised lesions, a surgical procedure widely known as focal therapy, which has been shown to reduce such complications, e.g. (Hambrock et al. 2010). It is important to note that, especially for the purpose of this thesis, focal therapies require guidance due to the need for precise targeting (van de Ven et al. 2011).

1.3 Prostate Cancer Imaging

Modern methods for the diagnosis, staging and treatment of prostate cancer rely heavily on medical imaging. Imaging techniques, such as high resolution multi-parametric MRI, potentially allow detection of the pathological changes for diagnosis and staging the cancer and visualisation of the gland zonal anatomy inside prostate and the surrounding anatomical structures. Most conventional imaging methods, such as ultrasound, CT and MR have been used for imaging the prostate gland. Other techniques, such as PET scan, have also been proposed (Schmid et al. 2005). In the following sections, developments of these imaging approaches are discussed.

1.3.1 Ultrasound Imaging

B-mode ultrasound imaging of the prostate can be performed via transabdominal, transrectal or transperineal approaches. The urethra provides the most important sonographic landmark within the prostate gland. From the bladder the urethra enters the prostate at the base of the gland, which is clearly visible in ultrasound images. The apex of the gland is also visible in ultrasound and defines the inferior margin of the gland (Halpern 2006). See Figure 1.5 as an example. The inner- and outer glands (as described in Section 1.1) correspond precisely to two counterpart structures in ultrasound (Halpern 2006;Halpern et al. 2002).

Unfortunately, a significant portion of prostate cancers are isoechoic with the surrounding prostate tissue, which means that little difference can be seen between lesions and healthy tissues in ultrasound images. Although some echogenic lesions may be observed, a great overlap

between benign and malignant lesions causes a very poor sensitivity to detect cancer via B-mode ultrasound imaging (Cochlin et al. 2010;Halpern et al. 2002).

However, by analysing the raw radio frequency data used to form conventional B-mode images, some studies suggest that an improved likelihood of the locations of potentially significant lesions may be computed using recently proposed computer algorithms (Aarnink et al. 1998). Such algorithms seek to quantify pathological changes in prostatic tissue so that high risk foci may be differentiated. Some commercially available techniques are already being included as part of clinical trials to assess the practical sensitivity in patients, e.g. (Aarnink et al. 1998;Braeckman et al. 2008). The ability to detect the prostate cancers using other ultrasound modes, such as colour and power Doppler, has not been demonstrated convincingly. Furthermore, the use of micro-bubble contrast agents has demonstrated increased sensitivity and tumour detection rate compared with conventional B-mode ultrasound (Halpern et al. 2005;Yang et al. 2008). Ultrasound-based tissue characterisation and elastography have also been the subjects of recent attention (Braeckman et al. 2008;Moradi et al. 2009;Zhang et al. 2008). To date, most of these methods still require further development and/or evaluation to determine the validity and translation into clinical practice.

In current clinical practice, the most important role for B-mode ultrasound remains the guidance of surgical procedures, including brachytherapy, cryotherapy, intensity-modulated radiotherapy, high-intensity focused ultrasound (HIFU) and photodynamic therapy (Loch et al. 2007). Compared to other image guidance methods, ultrasound has several advantages, including safety (it is a non-ionising imaging approach), and the fact that it is simple to perform, widely accessible, portable, and inexpensive.

Recent developments in 3D TRUS provide a method for accurate localisation of targeted regions. A 3D volume may be reconstructed from a series of B-mode slices and this approach is commonly applied in prostate needle biospy, brachytherapy system (Wei et al. 2005). There are different available methods for reconstructing 3D ultrasound images, including those that employ a stepper with the traditional 2D ultrasound probe to acquire a stack of 2D B-mode slices which are assumed to be parallel to each others; or orientated in a 'fan shape' if the probe is rotated about its long axis. A motor may also be integrated to automate the translational motion (e.g. Sonablate© probe, US HIFU, LLC, NC) or rotational motion, for a side-firing probe and an end-firing probe less in a second, respectively. Figure 1.5 shows an example TRUS slice

(left) and a reconstructed 3D volume (right). Other applications, including therapeutic procedures such as HIFU therapy and radiation therapy, currently being guided by 2D system potentially may benefit by 3D TRUS.

1.3.2 Magnetic Resonance Imaging

Prostate MR images provide rich anatomical information. On T1-weighted sequences, the signal intensity of the prostate is uniform and is difficult to distinguish from skeletal muscle. Neither the zonal anatomy nor the adjacent major anatomical structures, such as rectum and seminal vesicles, can be clearly visualised. However, T2-weighted sequences allow clear differentiation of the internal anatomy of the prostate gland. For instance, the peripheral zone has high signal intensity while some parts of the central zone are low. Figure 1.6 shows an example of T2-weighted MR prostate image in transverse and sagittal views.

Figure 1.6 Example slices of a T2 MR image of prostate. Left: the transverse view and, right: the sagittal view

The use of MR imaging is relatively new as a diagnostic tool in prostate cancer, but it has attracted a great of amount research interest due to its increasing availability and the ability to identify local, small, yet clinically significant tumour inside prostate. MR is now widely considered to be the most promising imaging modality for non-invasive identification of prostate cancer.

A systematic review of this technique reports a sensitivity of between 60% and 96% for localising prostate cancer using T2-weighted MR imaging when performed with an endorectal coil (Kirkham et al. 2006). A prospective multicenter study, conducted by the American College of Radiology Imaging Network and published since the review of Kirkham et al., reports an area

under the ROC curve of between 0.58 and 0.63 for the sextant localisation of peripheral zone cancer using T2-weighted MR imaging alone with a 1.5T pelvic phased-array coil (Weinreb et al. 2009). Although this study found no significant difference between standard MR imaging and MR spectroscopy in terms of cancer localisation accuracy, several other studies in the literature have convincingly demonstrated that imaging at higher field strengths (in particular, 3T) and/or the addition of one or more functional MR imaging techniques, such as dynamic contrast enhanced (DCE), diffusion-weighed (DW) imaging or MR spectroscopy - "multi-parametric MR" - can significantly improve detection accuracy (Ahmed et al. 2012;Futterer 2007;Futterer et al. 2007;Kirkham et al. 2006;Ravizzini et al. 2009;Villers et al. 2006;Villers et al. 2009).

Presently, the specificity of MR imaging for localising prostate cancer is not sufficiently high to replace needle biopsy as the gold standard test for prostate cancers and therefore histological verification is still required. Nevertheless, MR imaging has emerged as a powerful clinical tool for identifying "suspicious regions" within the prostate gland. Once localised, MR-visible lesions can be targeted during biopsy, given the availability of sufficiently accurate image guidance technology using an interventional MR or an MR-US fusion (Pinto et al. 2011). Furthermore, the detailed information on the 3D spatial distribution of disease, the presence or absence of extracapsular extension, involvement of the seminal vesicles, and patient-specific pelvic anatomy provided by MR imaging, combined with localised histological information provided by targeted biopsy, are powerful tools for clinical management and subsequent therapy planning (Ahmed et al. 2009).

1.3.3 Other Imaging Modalities

Because of the limited soft tissue contrast, CT has poor performance for diagnosing prostate cancer (Turkbey et al. 2009b). However, CT is the conventional modality for radiotherapy planning due to its ability to measure electron density and visualise bony anatomy. It is also useful to provide relative spatial information in a number of procedures (see Section 1.2.2). PET imaging has the ability to localise tumour by monitoring metabolic changes with appropriate agent, but is limited by low spatial resolution. The reliability and accuracy of this technique is still under investigation. Other imaging methods have also been applied to the prostate, including single photon emission computed tomography (SPECT), but these are still under development to provide better sensitivity and specificity (Turkbey et al. 2009a). However, these

image modalities are not considered further in this thesis, but the interested reader is referred to the survey by Turkbey et al. (2009a).

1.4 Image-guided Prostate Interventions

Recently, there has been growing clinical interest in targeted therapy strategies in which only part of the prostate gland containing the tumour is treated in order to minimise the damage to nearby vulnerable structures, such as nerves (Ahmed et al. 2007;Ahmed et al. 2008;Eggener et al. 2007;Scardino et al. 2008). The principal motivation for such approaches is the potential for a reduced risk of side-effects compared with traditional "whole-gland" interventions. Implementing focal or tissue-sparing therapies is, however, highly problematic since they rely critically on the availability of an accurate method for disease localisation as well as precise (image-guided) delivery technology. The current gold standard for cancer localisation is transperineal template-guided saturation biopsy mapping in which 20-100 tissue samples are collected systematically at 5mm intervals using a template grid under TRUS guidance (Onik et al. 2008;Pinkstaff et al. 2005). This technique is significantly more invasive compared to freehand transrectal biopsy, which is used routinely for diagnostic purposes, but it is usually performed under general anaesthesia to minimise patient discomfort and distress (Pinkstaff et al. 2005). Biopsy-verified, MR-based disease localisation using MR-targeted biopsy, on the other hand, potentially offers a less invasive alternative without compromising accuracy since fewer samples are required (Schouten et al. 2012). In patients with localised disease, the same MR-targeted approach can be applied to deliver minimally-invasive interventions using a treatment plan based on information derived from MR images and co-registered biopsy results (Pinto et al. 2011).

One approach to MR-targeting is to perform such procedures in an MR scanner (Makni et al. 2009;Pondman et al. 2008;Tempany et al. 2008). However, this solution is technically demanding and requires special-purpose, MR-compatible equipment and instruments. Moreover, despite the fact that MR imaging facilities are undoubtedly becoming more widely available in hospitals, it remains a high cost solution that is currently practical only in a relatively small number of specialist centres. Access to patient is much easier within open MR scanners, designed specifically for interventional procedures, but the image quality is generally too poor to reliably distinguish tumour. Therefore, diagnostic quality MR images must first be obtained using a (closed) diagnostic scanner and registered to the (low quality) images obtained during

the procedure. It is possible to perform interventions within a diagnostic MR scanner. This is technically difficult given the limited access to patient, and image acquisition is slow compared with TRUS imaging, meaning that true real-time guidance is currently not possible.

As illustrated in Figures 1.3 and 1.4, both freehand biopsy and template-guided biopsy employ TRUS for guidance. The patient is in a lateral position on a surgical table for the TRUS-guided procedures. The TRUS probe is inserted via the patient's anus, through the rectum and is placed under the gland. A saline-filled balloon cover the probe on top of the transducer will help provide a reasonable difference in acoustic impedance between soft tissues. Due to the isoechoic nature of prostate cancer, the possibility of allowing the physician to relate other (preoperative or intraoperative) information and to bring the preoperative plan in the intervention, in particular, using 3D TRUS (see Section 1.3.1) is the focus of this thesis.

A practical and relatively low-cost solution that motivates the work of this thesis is to use TRUS as the primary guidance modality, but to register MR images obtained prior to a procedure, possibly together with a co-registered surgical plan, to TRUS images obtained during a procedure (Kaplan et al. 2002). The surgical plan may define intended biopsy sample locations or the size, shape and position of a region of tissue encompassing a tumour, including a surgical margin. This approach has the advantage that the standard TRUS real-time guidance platform, which is familiar to practicing radiologists and urologists, is preserved. However, soft tissue motion on the order of several millimetres can occur between MR and TRUS imaging (Byrne 2005). Therefore, it is highly desirable that the registration method compensates for this effect to achieve the highest possible accuracy. Prostate motion can arise from a number of causes, including bladder filling, rectal wall motion, changes in patient position (e.g. supine versus lithotomy), placement of an endorectal coil during MR imaging, and from the placement of the TRUS probe. A second requirement is that the registration procedure should be as fast as possible and avoid significant user-interaction to minimise the disruption to the clinical procedure.

1.5 Thesis Aims

Data fusion between information obtained from different imaging modalities is enabled by multi-modality image registration, e.g. spatial alignment between MR and US images. Chapter 2 provides a detailed overview of this technique. However, current clinical procedures of such

image-guided minimally-invasive prostate interventions, including targeted biopsy and focal therapies, do not contain the component of computer-assisted image registration. The image registration described in this thesis may introduce two additional steps, preoperative planning and intraoperative registration: Before a procedure, planning is essential for any focal therapy or targeted biopsy, therefore the added (registration-required) planning, such as identifying the location of the lesion and possible manual segmentation of a preoperative image (see Section 3.2.1), is expected to be minimal; During the procedure, clinicians usually perform a "cognitive" registration between a preoperative surgical plan with the guidance images, whereas utilising the image registration usually requires certain manual interactions, mainly, identifying anatomical landmarks (see Section 4.2.1.1) and initialisation (see Section 4.2.3). A recent feasibility study (Dickinson et al. 2013) suggested that introducing such an extra registration step would not affect adversely the current workflow of preoperative- or intraoperative procedure.

The main aim of this thesis is to develop novel methods in image-guided prostate interventions for the purpose of data fusion to improve accuracy, efficiency and robustness of these clinical procedures. This includes 1) investigating and modelling the motion of prostate gland between the preoperative MR imaging to the intraoperative TRUS imaging; 2) developing a novel non-rigid registration algorithm to compensate such a motion; and 3) validating the MR-to-TRUS registration method using real patient data.

The main contributions of the thesis are the development and the evaluation of an advanced yet practical registration algorithm. This proposed algorithm adopts a novel motion modelling approach described in Chapter 3, and a novel model-to-image registration method, described in Chapter 4, for registering the prostate MR and ultrasound images. Chapter 5 provides rigorous validation methods to access each component of the algorithm whilst the Chapter 6 mainly presents the quantitative results from experiments using real patient data. The detailed contributions and further discussions are outlined in Chapter 7.

Chapter 2 Medical Image Registration: A Review

2.1 Overview

In general, image registration is the process of aligning images such that corresponding features are related mathematically (Hill et al. 2001). Images might be acquired at different times, from different patients, and/or by different imaging modalities. In the simplest case of pair-wise registration, the two input images are usually referred to as *source image* and *target image*. A *spatial transformation* is applied to the source image so that it is transformed into the space of the target image and the source and target images "match". The parameter to estimate how good the "match" is often termed *similarity measure*. If the spatial transformation is explicitly defined as a function of some parameters, the optimisation problem to find these parameters is usually referred to a *parametric registration*. This is the main type of image registration considered in this thesis. This type of image registration is usually posed as an optimisation problem where the aim is to find an optimum transformation, governed by a set of optimised parameters, which maximises the similarity measures. The similarity measure (to maximise) is equivalent to an objective function (to minimise), whose value is often considered as an error or distance in the field.

Symbolically, the parametric image registration problem may be represented as follows: Using the notation adopted by Hill et al. (Hill et al. 2001), image registration is defined more formally as the problem of finding the spatial transformation T, defined as:

$$\mathrm{T}(\mathbf{x}_B) = \mathbf{x}_A \tag{2.1}$$

where, $\mathbf{x}_A$, and $\mathbf{x}_B$, are *positions* (position vectors) from image *A* and *B*, respectively. The position vectors are represented by the spatial co-ordinates in 2D or 3D, and the goal of registering two images is to best align *corresponding locations*[1] using image intensities or features, $A(\mathbf{x}_A), \mathbf{x}_A \in \Omega_A$, where the image intensity/feature A (or B) is a function of spatial location $\mathbf{x}_A$, and Ω_A is the domain over which the intensities/features representing image A (or B) are sampled.

[1] The term *corresponding features* may have different meanings besides locations, *corresponding location* is used in this thesis to distinguish between the feature used in *feature registration*

However, corresponding locations are usually unknown or unclear directly from intensities. In medical images, this correspondence is related to physical entities of interest in the real world, e.g. patient information in medical images. It is a similar problem discussed in "Feature Correspondence" in Section 2.2.2.3. For the purpose of image registration, a *similarity measure* is defined as a function of $A(\mathbf{x}_A)$, $B(\mathbf{x}_B)$ and T to quantifying the goodness of the alignment:

$$S = f_S(\mathrm{T}, A(\mathbf{x}_A), B(\mathbf{x}_B)) \tag{2.2}$$

Assuming a parametric transformation $\mathrm{T}(\boldsymbol{\theta})$, numerical optimisation therefore can be used to find the transformation parameters, contained in vector $\boldsymbol{\theta}$, that maximises the similarity measure:

$$\boldsymbol{\theta} = \arg\ \max_{\boldsymbol{\theta}} f_S\big(\mathrm{T}(\boldsymbol{\theta}), A(\mathbf{x}_A), B(\mathbf{x}_B)\big) \tag{2.3}$$

Numerous clinical applications have been identified that benefit from the use of image registration, but this thesis focuses on statistical analysis of inter- and intra-patient pathology and surgical plan delivery in image-guided interventions. A review of the applied image registration is beyond the scope of this report. However, a particular field of interest, image-guided interventions, is discussed in the later sections.

It is because of different imaging procedures, subjects (e.g. different patients, organs and regions of interest), modalities, and even different operators, that medical images are different from case to case and, therefore, require trained clinicians to interpret. A universally applicable method or framework for registering medical images has not been proposed (assuming it exists) for all the tasks encountered in real clinical situations between pairs of image data of interest. Nonetheless, for instance, a framework (Rueckert et al. 1999) has been successfully applied to a class of scenarios where an image registration method is required for purposes of data fusion. Following the methodology proposed in this framework, to devise a registration procedure for a particular problem, one should follow these steps: 1) choose a transformation type; 2) define a similarity measure to represent the goal; and 3) solve the optimisation problem. This three stage approach to registration has been adopted by many researchers working in this field, especially in the context of medical images (Hajnal et al. 2001;Hill et al. 2001;Holden 2008).

Intensity- versus Feature based Registration

Various definitions have been adopted in the literature for intensity- or feature-based registration which can be used for distinguishing between them. Nevertheless, popular classification criteria are that intensity methods use the raw image data, whereas feature-based methods use a processed version of the raw image data (possibly incorporating information from other sources to perform the processing) to indentify and extract features of interest, such as intensity "edges", "ridges" or anatomical landmarks. Using these definitions, several review authors classified existing methods into different categories (Hill et al. 2001;Maintz et al. 1998;Zitova et al. 2003). In some literature (Goshtasby 2005), the features, such as corners, lines, curves, templates, regions, and patches, were defined explicitly and extracted exclusively for registration.

For the purpose of this thesis, using $\mathcal{T}$ to denote for both spatial and intensity transformations, intensity- and feature-based registrations may be unified using the following relation:

$$S = f_S(\mathcal{T}[A(\mathbf{x}_A)], B(\mathbf{x}_B)) \tag{2.4}$$

where an image voxel now is considered as a four dimensional feature - the scalar intensity value plus the three location co-ordinates. This similarity measure is a function of two images and the transformation $\mathcal{T}$. In intensity-based registration, interpolation is adopted to account for the transformation of the intensities. This is one of the core assumptions in intensity-based registration. In feature-based registration, the transformation of the feature values becomes non-trivial mainly due to the sparse and irregular distribution of feature locations. This is probably why the most popular feature remains simple point feature, which assumes that it is sufficient to replace the intensity with a binary value for a subset of all voxel locations. The sparseness of the point feature registration leads to, in general, a method that is less robust yet extremely fast due to the small amount data that needs to be processed. There are some alternative methods working in the middle-ground, e.g. (Cachier et al. 2002;Feldmar et al. 1997;Ourselin et al. 2000). These techniques are discussed further in Sections 2.2 and 2.4.

In practice, however, there seems to be a clear line between conventional intensity- and feature-based registrations based on differences in the objective functions and optimisation strategies. For example, completely different objective functions and optimisation strategies were employed between registering breast MR images (Rueckert et al. 1999) and registering

bone images (Barratt et al. 2008), respectively. In this thesis, it is argued that one logical classification of medical image registration methods is to consider intensity-based registration as a *special case* of feature-based registration, where the image intensities are features. In this sense, image features in medical image registration have slightly different meaning than those defined in conventional image processing literature, which are defined generally as a distinguishing primitive characteristics of an image (Gonzalez et al. 2008).

However, it is noteworthy that there is not one universal definition for each of these approaches, so that the classification of some methods as either intensity- or feature-based is not straightforward. Increasingly, there are a number of approaches that combine both techniques to produce superior registration performance than either one can achieve alone, e.g. (Cachier et al. 2001;Papademetris et al. 2004). Because the intensity-based method is generally an automatic method and may use all the available information contained in both images, it is often tested first. However, some multi-modality registration problems are challenging as the physics underlying the image acquisition of different imaging modalities can differ significantly and may not be correlated. In such cases, intensity-based methods can fail.

For the purpose of reviewing existing technologies, the following Sections 2.2 and 2.3 will focus on traditional methods considering the feature- and intensity-based methods, respectively.

2.2 Feature-based Registration

2.2.1 Feature Extraction

As determining a spatial transformation is the primary goal in image registration, features usually consist of spatial co-ordinates that represent geometric primitives. By distinguishing the additional dimension of feature data, this thesis proposes that the features are classified as point (binary), scalar and vector-valued multi-dimensional features. In such a classification, the vector-valued feature is a unified representation of image information, i.e. a point is a scalar with binary value and the scalar feature is a special case of a vector-valued feature.

2.2.1.1 Point Features

Manually identified point landmarks have been widely applied in medical image registration tasks. In particular, for a transformation with limited degrees of freedom (DOFs) (e.g. a rigid-body transformation), a reasonable amount of interactive effort has been acceptable to

establish a low dimensional transformation between fiducial landmarks for many applications (Hajnal et al. 2001).

In the medical image registration literature, point features have been developed extensively because they are straightforward to understand, extract and process. The iterative closest point (ICP) algorithm (Besl et al. 1992) and its variants have been proposed for rigid alignment between two un-ordered sets of points. The central idea is to update the point correspondence and the transformation alternately until convergence. To improve the robustness of the method, the assumption of deterministic correspondence (closest point) has been improved by introducing probabilistic generalisations, such as soft assignment (Gold et al. 1998) or a Gaussian mixture model (GMM). On the other hand, robust point matching (RPM) (Chui et al. 2000;Chui et al. 2002) has been proposed and employs thin-plate-splines (TPS) to account for the non-rigid transformations. Finally, coherent point drift (CPD) has been recently proposed as a generalised framework for non-rigid point sets registration (Myronenko et al. 2006;Myronenko et al. 2010). Closed-form solutions are available for updating the transformation parameters in all the above mentioned algorithms, such as Procrustes analysis in the rigid case (Hill et al. 2001). These methods are discussed in detailed in Section 2.4.1.

In the ICP, RPM and CPD methods, the features are sets of points with 2D or 3D co-ordinates representing spatial locations and automatic point feature extraction methods become attractive to reduce the level of user interaction required which introduces human error and is time-consuming. Most standard point detection methods are related to differential operators based edge detectors. For instance, the Canny edge detector (Canny 1986) is an approximation of the first order differential operator, gradient. Furthermore, second-order derivatives of the intensity capture the rate of change in the intensity gradient. Thus, in the ideal continuous case, detection of zero-crossings in the second derivative captures local maxima in gradient.

Furthermore, differential structures of an image provide rich information about local features. These local feature characteristics may be further analysed by eigen-decomposition of the Hessian matrix (via scale-space approaches) to enhance certain structures of interest, such as edges, ridges and locally tube-like structures (Frangi et al. 1998;Lorenz et al. 1997;Sato et al. 1997).

These computational operators should be able to provide useful point features by some further binary classifications, for example by a simple thresholding.

2.2.1.2 Scalar-valued Features

One special example of a scalar feature is the weighted geometrical (point) feature (Giannopoulos et al. 2002;Maurer, Jr. et al. 1996). The interpretation of the weight in this case can be related to the relative importance, and/or the uncertainty of each individual point: the larger the weight, the greater the influence of the associated point, as well as less flexibility provided by this particular feature in the matching process. Often, the weights can be normalised to sum up to a unit such that it can be interpreted as membership values, or in a probabilistic setting, by membership probabilities (discussed further in Section 2.4).

For the weighted point features, a summary measure, such as the sum, average or RMS of weighted distances, can form the objective function. It is however not a most general case. A more interesting scenario is when a general function of co-ordinates and a scalar value are considered collectively. Image intensities can therefore be regarded as an additional dimension such that every independent voxel in a 3D image becomes a 4D feature. The work of (Feldmar et al. 1997) proposes an extension to the ICP algorithm to use such a 4D feature for registering brain and heart images.

2.2.1.3 Directional and other Vector-valued Image Features

In the work (Feldmar et al. 1997) mentioned in the previous section, a higher dimensional feature – for example 7D feature which include intensities and directional gradients are used – is adopted to represent 3D images. From the “conventional” point of view, the use of directional gradients is incorporated into the similarity measures, independently proposed as normalised vector information (NVI) (Zhuang et al. 2005) and as a normalised gradient field (NGF) (Haber et al. 2006).

Arguably more relevant applications of vector-valued features have been found in the application of registration of diffusion tensor images: a diffusion tensor can be reconstructed to form three directional vectors (eigenvectors) which represent MR signals to indicate the principal directions of water diffusion (Alexander et al. 2001;Alexander et al. 2000).

2.2.2 Spatial Transformation Models

The transformation between two images is not necessarily interpreted as a spatial transformation defined in physical space. For example, consider the problem registering two images from different patients. There is clearly no defined motion: in this case, one might have to resort to homological features to define the registration problem (Crum et al. 2003), which should be dependent on biological definition, the application or the purpose of the analysis.

$\mathcal{T}$ (in Eq. 2.4) is defined as a "more complete" transformation applied to both locations and associated intensities (in Page R5, (Hill et al. 2001)). Interpolation sampling strategy can be applied to solve this problem of transforming intensities, so intensity value would be available for sampling at any given location in the *transformed* space. Therefore, in this case, $\mathcal{T}$ simply reduces to T (in Eqs. 2.2 and 2.3). However, this relies on the assumption that the intensity transformation is independent of the spatial transformation. For example, ultrasound images change intensities when the transducer is moved due to its directional dependent imaging (Wachinger et al. 2009). In this case, conventional interpolation and sampling methods, such as linear interpolation, are arguably inadequate. However, if necessary, some adjustment when estimating similarity measures may be useful. One example of such an adjustment is introduced in Section 4.2.1.1 to distinguish image features depending on whether they are aligned with ultrasound wave direction.

Nonetheless, in the case of registration for image guidance application, the images to be registered are usually from the same patient and differ primarily due to the gross patient motion, the tissue deformation and/or the change of modality. These different types of spatial transformations are primarily considered in the following subsections. In this thesis, depending on whether an explicit case-specific method to construct the transformation is being used, non-rigid transformations are considered as general-purpose- and case-specific ones.

2.2.2.1 General-purpose Transformation Models

Rigid Transformations

The rigid- or rigid-body transformation is the simplest transformation model, which describes a combination of a translation and a rotation. It is useful in general because these transformations very often occur between different images, for example, due to patient- or (pose-dependent) imaging sensor motion. The rigid transformation is a well constrained transformation model,

which leads to a limited search space for any optimisation algorithm and direct (i.e. closed-form) solutions, under certain conditions.

Rigid transformation may be expressed as follows:

$$\mathbf{x}_A = \mathrm{T}_{r6}(\mathbf{x}_B) = \mathbf{R}\mathbf{x}_B + \mathbf{t} \tag{2.5}$$

where $\mathbf{x}_A$ and $\mathbf{x}_B$ are two 3-dimensional position vectors, containing 3 elements to representing the spatial co-ordinates (of points or of pixels/voxels). $\mathbf{t}$ is a translation vector $\mathbf{t} = [t_x, t_y, t_z]^T$. $\mathbf{R}$ is the 3×3 rotation matrix, constructed by 3 rotation angles. For instance, $\mathbf{R}$ is defined in 3D as:

$$\mathbf{R} = \begin{bmatrix} 1 & 0 & 0 \\ 0 & \cos\theta_x & -\sin\theta_x \\ 0 & \sin\theta_x & \cos\theta_x \end{bmatrix} \cdot \begin{bmatrix} \cos\theta_y & 0 & \sin\theta_y \\ 0 & 1 & 0 \\ -\sin\theta_y & 0 & \cos\theta_y \end{bmatrix} \cdot \begin{bmatrix} \cos\theta_z & -\sin\theta_z & 0 \\ \sin\theta_z & \cos\theta_z & 0 \\ 0 & 0 & 1 \end{bmatrix} \tag{2.6}$$

where $\theta_x, \theta_y \; and \; \theta_z$ are Euler angles representing the rotation about x-, y- and z-axis, respectively. This is not a unique formulation as it depends on the order of these matrices multiplied and the direction of rotation. Therefore, the constrained $\mathbf{R}$ matrix is preferred to generally represent rotation, subject to $\mathbf{R}^T\mathbf{R} = \mathbf{I}, |\mathbf{R}| = 1$, where, $\mathbf{I}$ is the identity matrix and $|\mathbf{R}|$ is the determinant of the rotation matrix. An isotropic scaling factor s may be included to extend the rigid transformation as follows:

$$\mathbf{x}_A = \mathrm{T}_{r7}(\mathbf{x}_B) = s\mathbf{R}\mathbf{x}_B + \mathbf{t} \tag{2.7}$$

More generally, an affine transformation describes a group of transformations preserving straight lines, including scaling, shearing, reflection and rigid transformations. It can be defined as:

$$\mathbf{x}_A = \mathrm{T}_{affine}(\mathbf{x}_B) = \mathbf{A}\mathbf{x}_B + \mathbf{t} \tag{2.8}$$

where $\mathbf{A}$ is an "unconstrained" 3×3 matrix. Due to similar properties in representation, with higher DOFs (up to 12 with additional 3 DOF from translation $\mathbf{t}$), the affine transformation is sometimes referred as a generalised rigid transformation (Audette et al. 2000) In most cases, image re-positioning, scaling and/or distortion can be approximated by an affine transformation.

Because rigid- and affine transformations are of great importance both in medical image registration (Audette et al. 2000;Hill et al. 2001;Maintz et al. 1998), and also for pose estimation in computer vision, e.g. (Haralick et al. 1989), analytical solutions have been studied extensively.

One such a solution is to solve the least squares problem with or without different constraints (Hill et al. 2001;Myronenko et al. 2010), i.e. to maximise:

$$S = -\sum_{n=1}^{N} \left\| \mathbf{x}_{A_n} - \mathrm{T}(\mathbf{x}_{B_n}) \right\|_2^2 \tag{2.9}$$

where $\|\cdot\|_2$ is the Euclidean norm of the difference between two points, also known as L_2 norm, and N is the number of pairs of *corresponding* points. Different p-norms have also been proposed to improve registration robustness and/or speed (Jian et al. 2005).

In general, if a well-defined objective function (similarity measure) is specified, the optimum rigid- or affine transformation may be found using a standard, general-purpose optimiser (e.g. gradient descent, discussed in Section 2.3.3).

Non-rigid Transformations

Non-rigid (higher dimensional) transformations have been introduced to model the deformable change on non-rigid object (such as human soft tissue) or other having DOF larger than the rigid/affine transformation (Crum et al. 2003;Hawkes et al. 2005;Hill et al. 2001). General-purpose, non-rigid models have been proposed for modelling transformations with higher DOFs.

An example of the first attempts to extend non-rigid transformations is to assume a global polynomial function exists relating source and target locations (Audette et al. 2000). However, this mathematically simple formulation, which can be solved by least-squares minimisation, has some severe drawbacks including lack of local modelling ability, difficulty in determining the model complexity, and unexpected distortion (e.g. due to high sensitivity to noise).

A better behaved transformation results from the use of splines as an interpolation function (Audette et al. 2000;Hill et al. 2001;Holden 2008). The term "spline" usually refers to a piecewise polynomial (parametric) curve. Thin-plate-splines (TPS) (Bookstein 1989) and B-splines (Rueckert et al. 1999) have been widely used for medical image registration problems. By assuming that displacement is a function of co-ordinates, $\mathrm{T}_{rbf}(\mathbf{x}_B) = \mathbf{x}_B + \mathrm{u}(\mathbf{x}_B)$, the radial basis function may take the general form:

$$\mathrm{u}(\mathbf{x}) = \phi_s(\mathbf{x}) + \mathrm{R}_s(\mathbf{x}) \tag{2.10}$$

where $\phi_s(\mathbf{x}) = \sum_j^M \beta_j \phi_s(\mathbf{x})$ and $\mathrm{R}_s(\mathbf{x}) = \sum_i^N \alpha_i \phi_s(\|\mathbf{x} - \mathbf{x}_i\|)$ are sums of M polynomial functions and N kernel functions, respectively. The coefficients α_i and β_j can be computed by

linear least-squares, although usually only a set of co-ordinates of point locations are used in the fitting process. These landmarks may be used in feature registration or grid points in free-form deformation (FFD), which is one example of a non-rigid transformation model. Many other non-rigid models are reported in literature, for example those are based on physical assumptions, such as elastic body (Davis et al. 1997), motion coherency (Myronenko et al. 2006)), and those are motivated by mathematical convenience (e.g. polynomials). The purpose of all of these models is to approximate tissue deformations principally encountered in the real world.

There are also scenarios where two types of transformations are used together, either simultaneously (Wang et al. 2000) or sequentially (Schnabel et al. 2001). In fact, the latter has become increasingly important in the area of image-guided intervention, where a rigid transformation is used first followed by a non-rigid transformation (Schnabel et al. 2001). It also should be noted that in the work by Wang et al. (Wang et al. 2000), the statistical shape model (which itself can be viewed as a case-specific transformation model, described in Section 2.2.2.3) was used as a prior to constrain the physical deformation instead of a direct, general-purpose parametric model.

A general review and more in-depth discussions of non-rigid transformation models may be found in a review paper (Holden 2008). Although equally important, non-parametric transformations are not considered here as, from an algorithmic point of view, they involve significantly different strategy to solve the registration problem. Examples of non-parametric transformations include elastic- (Broit 1981), optical flow-, diffusion- (Thirion 1998), and fluid-based methods (Christensen et al. 1996;Thirion 1998). Unified approaches to treat this class of transformations are proposed by Cahill et al. (Cahill et al. 2009) and Melbourne et al. (Melbourne et al. 2010).

Summary of General-purpose Transformation Models

Both rigid and non-rigid transformations introduced in this section are general-purpose models, which may or may not be based on physical models. To cope with real-world applications, one usually has to choose a model and tune the parameters controlling the behaviour of the transformation model. This inevitably includes, for instance, a trade-off between rigidity versus flexibility and smoothness versus geometric accuracy. These are not always easy tasks: for example, it is desirable that a transformation model has a global constraining ability so that missing data from the local area would not affect the overall approximation. But this global

ability usually comes at the expense of local behaviour not being modelled adequately. This is exemplified by some of the spline-based methods, such as approximating thin-plate-splines (Bookstein 1989) and elastic-body-splines (Davis et al. 1997), in which the parameters control certain smoothness in a global fashion without taking into account the inhomogeneous behaviour of real human tissue.

Two main alternative approaches to general-purpose transformation models have emerged: First, physics-based models which aim to describe the real world as accurately as possible, for example, classical theories of mechanics can be applied to model complex nonlinear and inhomogeneous soft tissue behaviour (Carter et al. 2005); Second, learnt data can be used to describe transformation model by adopting statistical learning methods. The statistical shape model popularised by Cootes et al. (Cootes et al. 1995) is a good example of this (see Section 3.1.2).

The role of the non-rigid (deformable) modelling in medical image registration is of great importance, since it provides a physically plausible and well-constrained transformation model, resulting in a reduced parameter search space and potentially a faster and more robust numerical optimisation. In general, modelling enables better controlled registration by employing physical or empirical rules. The biomechanical modelling and the statistical shape modelling are the deformable modelling approaches investigated in this thesis. These are discussed in more details in the following sections.

2.2.2.2 Biomechanical Modelling

In medical image computing, biomechanical modelling usually refers to applying the principles of classical mechanics to model interactions between internal and externally applied forces and the motion of organs. Medical images provide a rich source of information for this kind of modelling. For instance, methods to model mechanical behaviour of brain tissue have been developed, e.g. (Joldes et al. 2012).

A key original contribution in the application of biomechanical modelling for image registration during prostate interventions is the work by Bharatha et al. (Bharatha et al. 2001), where 1.5T MR images were registered with 0.5T intraoperative images using a biomechanical model. The displacement field between two images was computed by solving the finite element (FE) equations, after building a FE mesh representation of the prostate gland from a segmentation of

the source image. The boundary condition of surface displacement, derived from a surface-based registration method, was applied. More recent analysis using this approach is described in Section 5.4.3.

Finite element analysis (FEA) provides a widely-used numerical framework for solving both traditional mechanical problems and emerging biomechanical problems that arise from the study of complex biological systems. Biomechanical modelling using FEA has been proposed by a number of authors as a means of predicting organ motion and soft-tissue deformation (Alterovitz et al. 2006;Bharatha et al. 2001;Crouch et al. 2007;Hensel et al. 2007). It is probably the most popular and best developed method. The basic steps involved in FEA-based biomechanical modelling are:

1) Set up a geometrical representation of target organ and surrounding tissues of interest;

2) Assign estimated material properties for the tissues of interest;

3) Set the boundary conditions for a particular scenario, such as the displacement of an organ surface; and

4) Solve a system of equations for unknowns of interest, such as displacements, numerically.

The results represent a complete displacement field across the model. Other mechanical properties, such as strain or stress field also can be computed, although in the field of medical image computing the usefulness of estimating these parameters is still under investigation. The displacement field, on the other hand, is directly related to the spatial transformation which is of most interest in image registration tasks and is a common output of this type of analysis (Carter et al. 2005). The biomechanical formulation of the problem provides a framework to compute physically plausible deformations that provide a useful constraint for image registration.

The rest of this section outlines some features and practical aspects of the FEA used in image registration.

Finite Element Analysis and Meshing

The FEA methods share one essential characteristic: the discretisation of a continuous, complex domain into a large, finite number of simple geometric elements, e.g. triangles/rectangles in 2D,

or tetrahedrons/hexahedrons for 3D domains. Discretisation in this way allows mechanical principles to be applied on each element, resulting in a large scale system of partial differential equations and integral equations, which, for real-world biomedical applications, are also defined for a (e.g. geometrically) complex domain.

Commercially available software packages include ABAQUS (ABAQUS Inc., Rhode Island, USA) and ANSYS (ANSYS Europe Ltd., Oxfordshire, UK). For research purposes, open source codes are also available in MATLAB (e.g. (Balmes et al. 2010)), C++ (e.g.(Hecht 2009)) and CUDA (Taylor et al. 2008).

The first step in FEA is meshing, which some practitioners might argue is the most crucial task in the analysis. In 3D, there are relatively robust methods to automatically generate a tetrahedral mesh, such as Delaunay triangulation employed in ANSYS. Hexahedral elements are more difficult to generate for irregular domains, which are common for biological structures. One reason for this is that a region of interest usually has complex topology so that a structured (or mapped) hexahedral mesh cannot be directly mapped to it. On the other hand, linear tetrahedral elements are vulnerable to so-called 'locking' when the material is assumed to be almost incompressible. Locking refers to an excessive stiffness of the mesh that results in smaller interpolated displacements than that would actually occur. Numerical methods have been proposed to overcome this problem (Bonet et al. 1998;Joldes et al. 2009). More complex element shapes include higher order elements in which additional nodes are located at positions other than vertices. These may be considered to trade computational expense for accuracy. A review of the finite element mesh generation can be found in the paper by Ho-Le (Ho-Le 2001).

In practice, volumetric meshes are generated typically from a geometric representation of a surface, such as a distance function (Per-Olof et al. 2006) or a surface mesh. The latter provides a simple, discrete representation, which can be converted to most other representations. Therefore, the conversion of triangulated meshes is a popular approach and is supported by most solid meshing algorithms. For instance, to represent a closed surface, spherical harmonic surface representation can be sampled into a triangular surface mesh (Zacharopoulos 2005). Alternative methods exist, which have been designed specifically for surface meshing, e.g. (CGAL 2009).

Boundary Conditions and Material Properties

Boundary conditions (BCs) - which are also termed "loadings" in some fields of engineering - can be specified in forms of body displacements, velocities, accelerations, and forces and pressures (externally applied and/or due to gravity). However, tissue displacement is the type mostly applied for medical applications, largely because it is usually directly measurable from image data. Gravity is also considered in cases where it applies a significant load on organs that causes deformation (Carter et al. 2008). In the context of medical image registration, BCs are commonly estimated in two ways: first, by measuring a displacement between two corresponding points identified in images obtained at different time-points; and second, using the derivative of a similarity measure as a surrogate for applied force (Modat et al. 2010).

The mechanical behaviour of biological tissue under load is complicated, so certain simplifications and assumptions are made when assigning tissue material properties, which govern the relationship between stress and strain. An interesting argument is that for applications in image-guided interventions, computational speed is more important than the accuracy of the simulations (Hajnal et al. 2001). The general rule is that the more complex the analysis approach and the more detailed model, the greater the computational expense, but the more accurately model the real-world biomechanical behaviours. A relevant debate in the field is whether accurate material properties (in general, accurate constitute models) are required for modelling of human tissue deformation. In the prostate gland, some investigation work (Chi et al. 2006) and (Hu et al. 2008a) report errors of 4.5mm and 1.82mm (approximately 47% of total simulated displacement), respectively. These suggested that material properties should be estimated accurately. Whilst recent developments in computational hardware and parallel computing techniques have significantly reduced the computational burden of FEA, an accurate and complex (therefore realistic) material model, is believed generally desirable. The level of the complexity and accuracy, which depends on the application, is one topic of investigation in this thesis (see Section 3.2.5).

Displacement BCs can be computed for each node by either an explicit or an implicit solver, depending on the type of analysis (Zienkiewicz et al. 2000), and interpolated through the meshed region. The resulting deformation field computed from FEA over the regions of interest then serves as a transformation model for image registration. There are two different schemes to adopt the biomechanical analysis for image registration task, as outlined below:

The first approach involves direct estimation of both boundary conditions and material properties. In this case, the results of FEA are the solution to the registration problem, while the transformation parameters are obtained implicitly to when solving the FE equations. For instance, the surface normal direction to the target surface was used to set the boundary conditions and empirical material properties assigned for breast tissues in a study by Carter et al. which aimed to register prone and supine MR images of the breast (Carter et al. 2008).

The second scheme adopts a more image-specific (but potentially less realistic) similarity measure, such as mutual information. The FE equations are then updated iteratively using a synthetic force derived from the derivatives of this similarity measure so that the similarity measure is maximised at the end of iterations (Modat et al. 2010). A more direct approach performs one or more complete FE simulations in each iteration within a registration optimisation scheme, which includes boundary conditions and material properties as free parameters (Alterovitz et al. 2006).

The first scheme is largely subject to the prescribed BCs, and estimating these may be a challenging feature registration problem in itself (see the comparison study of (Crouch et al. 2007) for another example of this approach). Furthermore, the sensitivity to material properties remains an important consideration. The second method, on the other hand, is a natural extension of the intensity-based registration framework (outlined in Section 2.3) in which the registration is posed as an optimisation problem. It is however much more computational demanding in practice and may be potentially impractical for large scale 3D problems.

2.2.2.3 Statistical Shape Modelling

Another major class of transformation models employs statistical approaches. The basic idea is to analyse representative training data statistically in order to "learn" the transformation, which could then be used in the image registration. This type of transformation usually is specifically built for the object(s) of interest and the learnt transformation usually is not generalisable to other applications or other objects (organs) in the same patient.

One highly popular example of this approach is the statistical shape model (SSM) (Heimann et al. 2009), which was first proposed as a means of image segmentation (Cootes et al. 1995). A SSM describes the shape changes across a number of training samples, which are captured and parameterised by principal component analysis (PCA) which enables dimensionality reduction.

Therefore, a low-dimensional shape model may be combined with a basic rigid transformation to form a non-rigid transformation model with relatively small number of parameters. Other established alternative statistical approaches, such as factor analysis and linear regression (P.D.Sozou et al. 1994), have also been investigated and applied in a very similar fashion. Although a number of variations to original SSM have been proposed, the construction of all SSMs shares a three-stage scheme: shape representation, feature correspondence, and dimensionality reduction. These stages are discussed bellow.

Shape Representation

Arguably the simplest representation of a 3D shape is a point cloud, which is the basis of the point distribution model (PDM) (Cootes et al. 1995;Heimann et al. 2009). Sets of points are usually sampled from the surface of the object of interest. A complete representation of shape requires adequate point density (sampling frequency).

A different strategy is to represent a volumetric region of interest (ROI), where points can be easily sampled not only on the surface but also from locations inside of the ROI. An example of such a representation is the medial representation, such as M-reps proposed by Pizer et al. (Pizer et al. 2003), which have been applied to model organs including the prostate gland (Dam et al. 2008). Splines, such as non-uniform rational B-splines (NURBS) are also widely used to represent shape. NURBS have been used to re-sample the prostate gland surface (Wu et al. 2000;Wu et al. 2003). Spherical harmonics (SH) are another example of parametric model which represents closed surfaces. The use of spherical harmonics to represent the prostate gland was reported by Tutar et al. (Tutar et al. 2006).

It is noteworthy that, in principle, conventional linear statistical analysis, such as PCA-based SSM, can be applied to any parametric models (such as NURBS and SH) when the mapped parameter space has statistical significance; In other words, linear SSM can be applied on any parameters of the shape representation, such as the parameters of NURBS and SH, regardless the form of the representation. However, the resulting model is no longer linear due to the non-linearity introduced by the parametric form; and the resulting model may not be able to capture the most variance of the training data with fewer parameters (which is a goal of PCA-based SSM). This is probably the reason why most parametric shape representations (instead of being used directly in the statistical analysis) are mainly useful for point cloud sampling, visualisation and establishing the point correspondence.

Feature Correspondence

To enable a classical multivariate statistical analysis, multi-dimensional features representing training data need to share an identical multivariate space, meaning that not only the entire multivariate space but also all subspaces, in which the features are sampled, should be the same. However, sampling methods generally do not guarantee that the features from different shape data have common subspaces. For example, for each shape represented by the PDM, the co-ordinates of all the points are assembled in n^{th} data vector $\mathbf{x}_n = [\boldsymbol{\delta}_1^T, \boldsymbol{\delta}_2^T, \dots, \boldsymbol{\delta}_M^T]_n^T$, where M is the number of points and $\boldsymbol{\delta}_j^T = [\delta_x, \delta_y, \delta_z]$ is the 3D co-ordinate vector for j^{th} $(1 \leq j \leq M)$ point. The j^{th} point co-ordinates may be sampled from an arbitrary location, which has little relevance to the one sampled from another shape data, while the number of points M, may also be different. This presents a feature correspondence problem, which samples or re-samples the shape features so the resulting data vectors become corresponding features, i.e. share the common subspaces.

The correspondence between two images, or the same object represented by two images, might be defined according to homology (Crum et al. 2003), which indicates anatomically the same locations in most image registration applications. However, without expert knowledge, homological correspondence is rarely available for medical images. In particular, a ubiquitous point-to-point correspondence is very difficult to establish in certain circumstances. For instance, between the prostate gland shown in respective MR and ultrasound images, only the surface of the gland and very limited number of landmarks, such as points at the apex and base, can be defined reliably as corresponding landmarks, while the point-to-point correspondence on the rest of the surface remains unclear. From an algorithmic point of view, finding surface correspondence is equivalent to surface registration (Heimann et al. 2009). It turns out that most medical image registration tasks are equivalent to finding correspondence to enable all kinds of analysis, including data fusion and classical multivariate statistics analysis. Moreover, intensity-based image registrations, which establish voxel correspondence, have become one practical method for finding correspondence used in statistical analysis (Rueckert et al. 2010).

A valid question is that, if the correspondence can be found, why build an SSM-based transformation for registration? The answer is twofold: Firstly, it is usually possible to establish the correspondence between images of the same type from the same modality, but establishing correspondence between multimodal data is generally much more challenging. Secondly, for

certain applications, such as registration during image-guided interventions, processing time is very restricted, and an SSM-driven registration is usually more efficient (thanks to dimensionality reduction and the linearity of most adopted models) compared with correspondence-finding methods. It also separates the entire procedure in two stages, preoperative and intraoperative stages, therefore allows more time, potentially including for user interaction, to access and to process preoperative data, from which the transformation is learnt prior to the procedure.

Different criteria have been developed for surface-based registration, depending on the surface representation adopted. A review on methods to find correspondence using different surface representations is given in Heimann et al. (Heimann et al. 2009).

Dimensionality Reduction

PCA remains the most popular method to construct a statistical shape models in the field of medical image computing (Heimann et al. 2009). PCA was originally proposed by Pearson (Pearson 1901) as a general purpose method of representing physical, statistical, and biological data in linear, orthogonal and low-dimensional spaces.

Assuming an $3M$-dimensional data vector $\mathbf{x}_n$ (defined in the previous subsection), a $3M \times N$ matrix containing all N vectors can be defined as $\mathbf{X} = [\mathbf{x}_1, \mathbf{x}_2, \dots, \mathbf{x}_N]$. Given the assumption of *linearity* in the transformation, $\mathbf{X}$ can be expressed as a linear combination of basis (or component) vectors, onto which the data can be projected, and a bias vector $\mathbf{c}$, representing a constant offset. Collecting together the basis vectors into a matrix $\mathbf{P}$ gives $\mathbf{X} = \mathbf{PB} + \mathbf{c}\mathbf{1}^T$, where, $\mathbf{P} = [\mathbf{p}_1, \mathbf{p}_2, \dots, \mathbf{p}_L]$ is a $3M \times L$ matrix $L \leq 3M$ containing L $3M$-dimensional basis vectors; $\mathbf{B} = [\mathbf{b}_1, \mathbf{b}_2, \dots, \mathbf{b}_N]$ is an $L \times N$ matrix containing vector signals (or scores) corresponding to each of the data; and, $\mathbf{c}$ is an $3M$-dimensional constant vector.

Another two assumptions, *ranked variance* and *orthogonality*, are made in order to solve the change-of-basis problem in an efficient way: Firstly, the variances are assumed to associate with the importance of the basis (component); and, secondly, the new basis vectors or principal components are assumed to be orthogonal. In this case, eigen-decomposition can be used to diagonalise the covariance matrix, giving the variances in each of the orthogonal component:

$$\left(\frac{1}{N}\mathbf{X}\mathbf{X}^T\right)\mathbf{U} = \mathbf{U}\boldsymbol{\Lambda} \tag{2.11}$$

where $\mathbf{\Lambda}$ is a diagonal matrix containing eigenvalues indicating associated variances, each of which corresponds to the eigenvectors in $\mathbf{U} = [\mathbf{u}_1, \mathbf{u}_2, \dots, \mathbf{u}_{3M}]$. Rearranging Eq. (2.11), gives:

$$\mathbf{X} = \mathbf{UA} + \bar{\mathbf{x}}\mathbf{1}^T \tag{2.12}$$

where $\mathbf{A} = \mathbf{U}^T\mathbf{X}$ is the full coefficient matrix, and $\bar{\mathbf{x}}$ is the mean vector obtained from an average of the data in $\mathbf{X}$. The eigenvalues then are sorted in descending order and only the first L preserved. Usually, $L \ll M$. The corresponding eigenvectors now form $\mathbf{P} = [\mathbf{u}_1, \mathbf{u}_2, \dots, \mathbf{u}_L]$ to obtain the approximated reconstruction:

$$\mathbf{X} \approx \mathbf{PB} + \bar{\mathbf{x}}\mathbf{1}^T \tag{2.13}$$

where $\mathbf{B} = \mathbf{P}^T\mathbf{X}$ are the coefficients associated with the first L principal components.

Once correspondence is established, the shape training data can be assembled into the matrix $\mathbf{X}$. The resulting shape model is then:

$$\mathbf{x} = \mathbf{Pb} + \bar{\mathbf{x}} \tag{2.14}$$

If $\mathbf{X}$ contains the previously rigidly-aligned 3D co-ordinates of the shape nodes, the model is commonly referred as a PDM.

In the eigen-decomposition above, the operation of diagonalisation of the covariance matrix involves the underlying assumption of independence between components when these components are orthogonal. Strictly speaking, this assumption holds only when the first- and second-order moment statistics - i.e. the mean and variance, respectively - are sufficient to characterise the data distribution (for instance, if the data follows a Gaussian distribution). But in general, removing second-order dependencies is insufficient at revealing all structure within the data (Shlens 2009). This leads to one of the limitations of the PCA-based SSM.

To include higher-order statistics of the data and achieve better modelling ability, the first assumption to break is that of orthogonality. Principal factor analysis (PFA) provides a decomposition into easily interpretable modes, while still being a linear technique that performs dimensionality reduction (Ballester et al. 2005). However, closed-form solutions are no longer available for this case, so an iterative approach is required. Another approach is to break the original assumption of linearity. For example, kernel methods can be used to transform the

original data to another nonlinear basis when performing PCA, resulting in so-called kernel PCA (Ballester et al. 2005;Rathi et al. 2006;Scholkopf et al. 1998). Alternative linear or nonlinear projection was also proposed, by which the projected data have mutual statistically independent components. Independent component analysis (ICA) (Hyvarinen et al. 2009) can be employed to eliminate the requirement of Gaussian distribution of the data.

It is noteworthy that it is not necessary for data to follow a multivariate Gaussian distribution (Jolliffe 2002). The Gaussian assumption is only prerequisite if: 1) some inference is made that assumes that the PCA outputs, new components and variance, are Gaussian; and 2) the data is de-correlated significantly as a result of the matrix diagonalisation (Shlens 2009).

The Application of Shape Models

A shape model provides a mathematically convenient representation of shape space from which plausible shapes can be sampled. There are broadly two approaches for applying an SSM in image segmentation, registration and other related tasks: from a statistical point of view, the inferences of an SSM can be made such that: 1) unknown parameters can be estimated where the SSM captures a distribution of shapes. In this case, the coefficients contained in $\mathbf{b}$ are of interest and the problem reduces to a classical parameter estimation problem; and 2) another function, usually defined as a probability density function (PDF), is constrained within a Bayesian framework whereas the SSM serves as a prior. For example, a log-prior is usually used to regularise some other transformation model.

In the first approach, the parameters of the SSM are of interest and the model behaves like other transformation models, such as rigid or spline-based ones. In this case, an objective function and/or its derivative are evaluated for a set of parameter values. The second approach requires a probabilistic formulation or a combined energy function in which a general-purpose transformation is usually added to the regularisation term to penalise shapes with lower (prior) probability. For both of the above cases, the objective function should be defined with respect to the shape representation.

There are numerous medical image related applications of SSMs (Cootes et al. 1993;Cosio 2008;Dam et al. 2008;Ding et al. 2007;Mohamed et al. 2002;Thompson et al. 2008). The reader is referred to the review paper (Heimann et al. 2009) for a comprehensive list.

2.2.2.4 Combined Biomechanical-Statistical Modelling

Biomechanical modelling has been shown to be a promising development in medical image analysis (see discussion in the previous section). Theories and practices have been inherited from classical mechanics to model/simulate the motion of biological organ systems and, more generally, physical manifestations of physiological changes such as the electromechanics of the heart, the development of vascular diseases, and injury and response due to ablative therapy. Typically, a patient-specific geometric model is built from medical images; boundary conditions and constraints (for example, displacement of some known regions) are then estimated and specified; finally, numerical methods, such as FEA, are applied to compute a change in state of the model that will, for instance, correspond to a change in shape. However, varying patient anatomy, unknown and difficult to measure boundary conditions, and the complexity of the biomechanical behaviour of soft tissue make the analysis challenging in practice. For example, although models of complex soft tissue behaviour have been successfully developed and implemented, they are rarely used in practice, largely because such models are computationally expensive, which makes applying them to solve problems of the size and complexity encountered in medical applications problematic. Considerations of computational cost are particularly relevant for time-critical applications, such as image-guided interventions. Furthermore, uncertainties in the parameters which characterise the model, such as mechanical stiffness, can overwhelm the requirement for exactness of any particular parameter. In other words, some models are too sensitive to errors in the input parameters and, in most cases, it is impractical to reduce parameter uncertainty, for example by implementing an elaborate method for measuring patient-specific parameters *in vivo*.

Given these challenges, statistical approaches to handle model parameter uncertainty have emerged. One example, applied in the field of image-guided interventions (described in detail in the remainder of this thesis) is to perform *simulations* of organ shape changes that are likely to occur during the intervention before the intervention takes place. The pre-computed simulations employ all the information available at that time, such as anatomical information from preoperative imaging, and estimated parameter values, which are assumed to lie within range that reflects the known intra- and/or inter-subject uncertainty in parameter values. Even if that uncertainty is poorly defined or poorly understood, it is still possible to assign parameter values that reflect this uncertainty (but at the cost of more simulations). Therefore, rather than being used to compute an exact solution given a set of boundary conditions as in classical

biomechanical modelling, a biomechanical model can instead be used to produce a set of physically plausible solutions when the boundary conditions are poorly understood, difficult to estimate and/or subject to significant uncertainty. This *space of solutions* can then be summarised using statistics, for example, by re-parameterisation and dimensionality reduction using an SSM. In this way, a model can be built that captures prior biomechanical information and such a model may be optimised during an intervention as more information becomes available. This approach is sometimes referred as a combined statistical-biomechanical model (SBM) (Davatzikos et al. 2001).

SBMs confer several advantages: Firstly, they can be built using only the information of interest, such as the motion of a particular organ. Certain information, such as interactions with surrounding structures, may be required to perform biomechanical simulations, but is not interesting from a specific application point of view. The dimensionality of the resulting model, which may be a marginalised one (i.e. a model representing marginal probability of the original) with only variance of interest being efficiently covered, can be reduced to a much greater extent compared to conventional dimensionality reduction methods, which achieve a lower dimensional representation by excluding only variance due to random noise. Secondly, the model may be re-parameterised into a new space using significantly fewer parameters and possibly also with less correlation between parameters. This property is particularly helpful when these parameters are to be optimised numerically. Thirdly, the deformation/motion being defined not only on the surface but also throughout the solid 3D space of the whole region of interest, SBMs also provide a statistical framework for managing information at different stages, such as comparing different sources of information to measure the usefulness for surgical guidance. For instance, a patient's age and the size of an organ may or may not affect the deformation during a surgical procedure. By including this quantitative information in the SBM building, statistical analysis may identify the correlation between these variables and model parameters in order to explore any underlying connections and to better control the future application.

A major contribution of this thesis is the development of methodology to build and apply an SBM for image-guided prostate interventions. Details of the SBM developed for this purpose will be discussed in the later chapters.

2.2.3 Optimisation

Given a transformation model and an objective function (i.e. similarity measure), the registration problem becomes a numerical optimisation problem. In principle, a general-purpose optimiser can be used to solve the problem and estimate the optimal parameter values that maximise or minimise the objective function. In practice, numerical optimisation schemes vary in terms of convergence properties, speed and robustness, which are dependent on the application and the algorithm employed. General-purpose optimisers will be considered in Section 2.3.3.

Special cases also exist, for example, where pixel/voxel correspondence between images is known and both the transformation and the similarity measures can be linearised. For this case, least squares methods may be used to solve the registration problem directly without explicit iteration (Golub et al. 1996). A great amount of work has been done for this case, which was discussed in Section 2.2.2 in the context of formulating spatial transformations. More importantly, these methods serve as building blocks for solving the more complicated problems where one or more of the conditions specified above is not satisfied.

Another approach to optimise the objective function is based on (or inspired by) the expectation maximisation (EM) algorithms (Bishop 2006;Dempster et al. 1977), where the objective function is formulated as a likelihood function. EM algorithms have superior convergence properties compared to alternative optimisation approaches. This technique will be discussed in depth in Sections 2.4.1 and 4.2.2.

2.3 Intensity-based Registration

For the purposes of this thesis, also discussed in Section 2.1, intensity-based image registration is characterised as a registration method that uses directly the image intensity information to align images without any distinguishable intermediate steps to extract image features.

From a conventional perspective, intensity-based registration is posed as an optimisation problem where the objective function, determined by an image similarity measure, is a function of the transformed source image intensities, the target image intensities, and the free parameters of the transformation model to optimise (Hill et al. 2001). Therefore, the three components of intensity-based registration are the transformation model, the chosen similarity measure, and the numerical optimisation algorithm. This is analogous to the key components of

feature-based registration summarised in Section 2.2, but with the similarity measure being a function of intensity rather than general representations of extracted features.

The registration framework adopted in this thesis is generally described as feature-based registration, for which the intensity-based approach is a special case (see discussion in Section 2.1). The aims of this section are as follows: 1) to provide an overview of the area of intensity-based image registration; 2) to outline the key features of intensity-based registration so that the challenges of applying the intensity-based methods in the domain of image-guided interventions, especially for multi-modality data fusion, can be identified; and 3) to review some of the methods that share the same technical approaches to solve different registration problems.

2.3.1 Spatial Transformation

The general-purpose transformation models, introduced in Section 2.2.2.1, are also applicable for intensity-based image registration. Rigid- and affine transformations can be parameterised by a homogeneous matrix with up to twelve degrees of freedom. The obvious limitation of rigid transformation models is their inability to represent soft tissue. Furthermore, the simplifying assumption of rigidity may impact upon the performance of the similarity measure. For instance (Rueckert et al. 1999) reported less accurate registration when rigidly registering breast images for which a larger deformation had been introduced between the images. This is probably because particular similarity measure has different local and global performances. Most general-purpose, non-rigid transformation models introduced in Section 2.2.2.1 can also be applied in intensity-based registration schemes with the additional step of defining control points. Control points can be specified for each pixel/voxel in the image, a subset of pixel/voxels, or any arbitrary positions within an image domain. In the last two cases, interpolation is used to determine the pixels/voxel intensity value at any spatial location in the domain. As medical images are conventionally represented as a grid of discrete intensity samples, a natural representation of a non-rigid deformation field is as a displacement vector field defined over a Cartesian co-ordinate system. Building on early work in computer graphics, free-form deformation (FFD), in which a deformation is represented by repositioning a set of control points, has become popular in the medical imaging community. Most commonly, a spline-based transformation model is weighted by a set of control points that are distributed uniformly throughout the image domain. The control points effectively represent the deformation field in

the image, and the displacement at any point in the image space is found by interpolation and regularised by a spline. The B-spline is one popular choice (Rueckert et al. 1999). The Reader is again referred to the survey (Holden 2008) for a more detailed review of the literature.

Other types of transformation model, including finite element models (see Section 2.2.2.2) and statistical shape models (see Section 2.2.2.3), can also be applied for an intensity-based registration. Examples include an iterative method to optimise boundary conditions and/or material properties of a biomechanical model (Alterovitz et al. 2006) and a statistical deformation model for segmentation (which essentially is equivalent to a registration problem) (Shen et al. 2003).

2.3.2 Similarity Measures

Historically, measuring the similarity between two images has developed from simple arithmetic and statistical comparison to information theory. The sum of squared differences (SSD) is a simple and widely-used metric that quantifies the overall difference in image intensities (Hajnal et al. 2001;Hajnal et al. 1995). Correlation-based techniques, such as normalised cross correlation (Lemieux et al. 1994) and the correlation ratio (Roche et al. 1998), have been derived using statistical modelling of image formation with random noise. Mutual information (MI) (Maes et al. 1997;Viola et al. 1997;Wells III et al. 1996) and normalised MI (Studholme et al. 1999) were invented for image registration shortly after the entropy of the joint histogram between images was investigated (Hill et al. 1994). The generalised overlap measure for multiple- or fractional voxel labels was introduced for the purposes of analysis and validation of the registrations (Crum et al. 2005). Finally, the minimum description length (MDL) generalises most of the above metrics and has been applied successfully to a group of images (Marsland et al. 2008). A comprehensive review of established registration techniques may be found in Pluim et al. (Pluim et al. 2003).

A major difference with feature-based registration methods is that the intensity-based methods employ a similarity measure that is applied directly to intensity. In other words, the similarity measure is a simpler function of ubiquitous image intensity without considering explicitly the spatial information. Therefore, all available intensities are used to compute the objective function, which in general leads to a more robust method.

Furthermore, similarity measures between two images usually rely on the assumption that a block of intensity samples are available for both, which requires that the two images overlap. In practice, samples are usually directly from the positions at the voxel centres of one "reference" (target) image while the samples from another "floating" (source) image are interpolated from the same set of positions. This is a convenient framework to work with, which avoids the correspondence problem because the similarity measure can be computed for each pair of voxels at the same sampling location in source and target images. Interpolation is used to sample the intensity at required locations of a spatially transformed image. This implicitly solves for $\mathcal{T}$ (in Eq. 2.4) by assuming the interpolated intensities are not only the spatially transformed intensities but also the $\mathcal{T}$-transformed ones. To explain the most popular choices of similarity measures in the literature, independent intensity samples within an image and dependence between samples from two images are usually assumed, so the dependent relationship can be quantified to measure how similar these two images are, given certain transformation.

A major limitation, however, is that in practice such assumptions do not hold and, as a consequence, similarity measures may not always be applied successfully. This is particularly the case for multi-modal registrations, where different imaging modalities represent different physical properties of the human body which do not necessarily have any correlation or functional relationship.

2.3.3 Optimisation

Optimisation is a mathematical procedure to minimise or maximise an objective function of a set of unknown parameters in order to obtain the optimal values for the parameters of interest. As discussed, image registration is posed as an optimisation problem.

In practice, the optimisation problem is complicated because the objective function (similarity measure) is nonlinear, has multiple local minima and, sometimes, is expensive to compute, largely due to the direct application of a similarity measure on intensities that represent complex physical organs. General-purpose optimisers are often employed. These optimisers for example use combinatory schemes to find local minimum iteratively.

There are two general types of optimisation approach commonly used in image registration: derivative-free and derivative-based approaches, depending on whether the optimiser computes explicitly the derivatives of the objective function.

Derivative-free methods typically operate using a stochastic search scheme to iteratively find a lower or higher value of the objective function. Derivative-free methods can be applied to solve a variety of optimisation problems that are not well-suited for conventional derivative-based optimisation algorithms, including problems in which the objective function is discontinuous, non-differentiable, or highly nonlinear. Examples include the Golden Search method, quadratic approximation, genetic algorithms, pattern search, Powell's method, and the Nelder-Mead simplex method (Venkataraman 2002;Yang et al. 2005).

In addition to the non-linear nature of the image registration, with less computationally expensive interpolation and/or sampling methods, the objective function can become discontinuous and/or non-differentiable. Therefore, derivative-free optimisation approaches are the method of choice for these scenarios, and have been used in numerous studies in the literature, e.g. (Shao et al. 2006;Thompson et al. 2008;Wu et al. 2003). The results of these studies indicate that, with careful adjustment, these methods are effective for finding the optimum for a wide variety of clinical applications.

On the other hand, derivative-based methods, such as steepest descent, Newton's method, and Conjugate Gradient, typically use a Taylor expansion which approximates the objective function locally. In some applications, the vector-valued derivatives need to be re-computed iteratively. This takes up a large portion of the total computation time. Another drawback of most derivative-based method is that convergence to a global minimum is only guaranteed when initial parameter values are used that are sufficiently close to the optimum point, otherwise, behaviour can become erratic in highly nonlinear regions. This may mean that a good starting estimate for the registration is required in practice. To overcome such drawbacks, a number of adaptations have been described based on numerical approximations, such as the modified Newton or practical Newton methods (Nocedal et al. 1999;Venkataraman 2002).

A common problem encountered by those working in the field is that derivative-based optimisation approaches are difficult to apply successfully without a clear understanding of the underlying optimisation algorithm. In particular, setting the algorithm options and parameters appropriately becomes critically important for many applications. An example is that the subject of this thesis is model-to-ultrasound registration, where the low signal-to-noise-ratio and artefacts present in ultrasound images is challenging. To the best of the author's knowledge, a valid guideline for appropriate algorithm recommendations for image registration is currently

unavailable, particularly for multi-modality registration problems. Furthermore, robust optimisation is difficult to achieve without adopting a relatively large-scale optimisation scheme, which compromises computational efficiency. This is relevant because for most registration applications in image-guided surgical procedures, a fast implementation is highly desirable due the time-critical nature of such procedures. This motivates the modification of the sampling method and the similarity measure, described in Sections 2.3.1 and 2.3.2, so that the objective function has fewer discontinuities, fewer local minima, and a larger capture range (defined as the range of the parameters around the optimal values where no discontinuities or other local minima exist). These improvements potentially make the use of derivative-based optimisation method practical.

In some cases, the derivatives of the objective function may be computed analytically, but numerical estimation, for example, using a finite differencing scheme, is more common in practice.

Another type of derivative-based method is the classical solution to the linear least squares problem. This can be computed by setting to zero the derivatives of an over-determined system, described by a set of homogenous equations (Hill et al. 2001;Holden 2008), and solving efficiently using matrix inversion or decomposition.

The trade-off between different optimisation processes is that, in practice, successful optimisation for medical image registration benefits from adopting a combination of the above techniques. For example, some gradient-based optimisation algorithms employ line search to reduce the number of the objective function evaluations along the negative gradient direction. As another example of combined approaches, an EM-like optimiser is introduced in the following section where either direct least squares or an alternative optimiser is used to compute the transformation parameters in the maximisation steps (see Section 2.4).

2.3.4 Expectation Maximisation Methods

The maximum likelihood (ML) problem is a well-known problem in mathematical statistics where the parameters of a certain distribution are estimated by maximising a likelihood function given a finite set of samples of the associated random variables (Hogg et al. 2005). Practical problems can be modelled using this framework so that the unknowns can be estimated by assuming a certain distribution of a random process, such as unknown intensities.

The assumption of identically and independently distributed (IID) variables is normally applied so that the likelihood function can be expressed as the product of the PDFs of known random variables.

EM is an elegant algorithm to solve the ML problem (Dempster et al. 1977). Conceptually, the EM algorithm solves the ML problem by iterating two steps: an expectation step (E step) and a maximisation step (M step). In the E steps, the posterior probabilities of the latent variables are computed, whereas in the M steps the complete log-likelihood function, which is usually easier to deal with than the original likelihood function, is maximised to estimate the parameters.

The EM algorithm is useful as an alternative method for general-purpose optimisation. And for cases where no explicit likelihood function is defined, EM-like methods have also been shown to be effective. For instance, it has been proposed (but without rigorous derivation) that block matching (Ourselin et al. 2000) can be implemented using this strategy for optimisation. Furthermore, the applicability can be improved when approximations are made; for example, hard assignment (Arindam et al. 2003) allows approximation using only nearby data in the E steps, rather than all the data as in soft assignment. Generalised EM (GEM) can be proven to converge when parameters in the M step are optimised sequentially rather than simultaneously (Neal et al. 1998).

Two-step EM-like algorithms have also been proposed for registration applications (Cachier et al. 2002;Feldmar et al. 1997). This approach will be discussed in detail in Section 2.4, but as an example when a finite mixture model (FMM) is employed, the E- and M steps iteratively estimate the correspondences and optimise the transformation, respectively. It is noteworthy that the correspondence and transformation can be modelled explicitly in an EM-like method.

2.4 Probabilistic Formulation: Parameter Estimation

By introducing the existence of a “scene”, the objective of image registration may be represented by certain joint PDF of source and target images. Therefore, the image registration problem becomes an ML problem where the distribution parameters to estimate are the parameters of the unknown spatial transformation model. Intensity-based registration is, therefore, unified using a ML approach (Roche et al. 2000) and importantly, several widely-used image similarity measures can be generalised as formulations of a likelihood function of one image given another.

However, conventional feature-based registration methods require further assumptions to be incorporated into this general framework. The interpolation method and the optimisation method, although described only briefly in the original paper by Roche et al. (Roche et al. 2000), are believed to be of great importance. A number of other studies have attempted to provide some type of unification (Cachier et al. 2002;Feldmar et al. 1997). It proves difficult probably because, as discussed in Section 2.1, the correspondence problem is handled implicitly in intensity-based registrations, thanks to regularly sampled image data. For the feature-based approach, on the other hand, it is much easier to define a likelihood function and to represent explicit feature-to-feature (e.g. point-to-point) correspondence, thus leading to a solution using an EM algorithm.

The unified view incorporating conventional feature- and intensity-based registration methods potentially enables an alternative EM-like algorithm to be used to solve general registration problems. Such a unified framework may be advantageous because it may allow the benefits of intensity- and feature-based methods to be usefully combined.

Point-based registration provides a good example to introduce parameter estimation, ML estimation, and EM algorithms in the context of medical image registration, and is discussed in the next section. A review of attempts to adapt such an approach to intensity-based registration is omitted from this discussion as it has less relevance to the work presented in this thesis. The interested readers are referred to (Cachier et al. 2002) or (Feldmar et al. 1997) for a detailed discussion of this approach.

2.4.1 Point Feature Registration

For the purposes of this discussion, a point registration problem is one in which a spatial transformation transforms one point set onto a second point set such that the two point sets are spatially aligned. Following the transformation, it is assumed that the point correspondence is unknown and is not necessarily one-to-one (for example, to reflect the case where one point set contains more points than the other). In real-world problems, noise will also be present and data may be missing. The transformation can be rigid or non-rigid, and the similarity measure between two point sets often (interestingly) converges to the Euclidean distances between corresponding points.

2.4.1.1 Correspondence and Distance between Point Features

In Chui et al. (Chui et al. 2000;Chui et al. 2002), the relationship between point correspondence and registration transformation is described as a "chicken and egg" problem: either the correspondence or the transformation may be easy to estimate if the other is known. This discussion is based on the practical assumption that the Euclidean distance is a sufficient measure to obtain an acceptable transformation between two sets of points. While the features of interest are point sets, the distances between points become naturally a similarity measure, i.e. a measure of how well points are aligned. If the correspondence between points is known, a summary metric such as the average distance between corresponding points provides a suitable objective function. Analytical solutions have been proposed to estimate the rigid- (Umeyama 1991) and non-rigid transformations (Bookstein 1989) with respect to a given set of point displacements.

On the other hand, if the distances between point sets can be defined in a more general manner, the correspondence does not need to be considered separately. For instance, in the iterative closest point (ICP) algorithm, which will be discussed in more detail in the following subsections, the average distance between closest points can be regarded as an overall measure between point sets, whilst the closest points are the correspondent points from another point set (Besl et al. 1992). However, the transformation is usually more difficult to estimate directly due to the complexity of such a distance function, which is dependent on the determination of the closest points. The problem then becomes a numerical optimisation problem.

The difference between traditional feature- and intensity-based registrations may also be understood in this viewpoint (described in the previous two paragraphs): the correspondence is assumed to be known (the same location) in intensity-based registration while the correspondence must be determined in feature-based registration. Several methods that adopt a unified view of correspondence and transformation within a single framework are reviewed below.

2.4.1.2 Mixture Models and the EM Algorithm

The finite mixture model has received increasing attention for feature-based registration and can be defined as:

$$f_{\mathrm{X}}(\mathbf{x}) = \sum_{m=1}^{M} \alpha_m f_{\mathbf{z}_m}(\mathbf{x}; \boldsymbol{\theta}_m) \tag{2.15}$$

where the PDF f_{X} is expressed as a weighted sum of the component distribution $f_{\mathbf{z}_m}$ with parameters $\boldsymbol{\theta}_m$. $\alpha_m \in [0,1]$ are the so-called mixing parameters, satisfying $\sum_{m=1}^{M} \alpha_m = 1$.

According to ML theory, the unknown parameters can be estimated by maximising the log-likelihood function, i.e:

$$\widehat{\boldsymbol{\theta}} = arg\max_{\boldsymbol{\theta}} logL(\boldsymbol{\theta}|\mathrm{X}) \tag{2.16}$$

Assuming *N* observation data is available and IID then:

$$L(\boldsymbol{\theta}|\mathrm{X}) = \prod_{n=1}^{N} f_{\mathrm{X}}(\mathbf{x}_n) \tag{2.17}$$

The ML solution has been investigated when the component PDF is a Gaussian function. Eq. 2.17 then becomes a Gaussian mixture model (GMM). As no analytical solution exists for this ML problem, the EM approach has gained popularity. This algorithm can be used to solve this ML problem with guaranteed convergence and an efficient implementation. The basic idea of EM is as follows:

1) Estimate the probability distribution of the unobserved data (latent variables $\mathbf{z}_m$) given parameters estimated in the previous step;

2) Estimate the distribution parameters by maximising the posterior complete log-likelihood function (with known latent variables, estimated in previous step); and

3) Repeat steps 1 and 2 with in an iterative scheme.

A full derivation can be found in most text books on mathematical statistics (Bishop 2006;Hogg et al. 2005). The solutions for the i^{th} iteration are given by (Bilmes 1997):

In the E step,

$$p\left(\mathbf{z}_m \middle| \mathbf{x}_n, \boldsymbol{\theta}^{i-1}\right) = \frac{\alpha_{\mathbf{z}_m}^{i-1} f_{\mathbf{z}_m}\left(\mathbf{x}_n \middle| \boldsymbol{\theta}_m^{i-1}\right)}{\sum_{k=1}^{M} \alpha_{\mathbf{z}_k}^{i-1} f_{\mathbf{z}_k}\left(\mathbf{x}_n \middle| \boldsymbol{\theta}_k^{i-1}\right)} \tag{2.18}$$

the computation of the posterior probabilities in the E step is sometimes called *soft assignment*. The probabilities of the latent variables represent estimated clustering, from which the data are "generated" (or being "*correspondent to"* in context of image registration).

In the M step, the complete log-likelihood function becomes:

$$Q\left(\boldsymbol{\theta}^{i}\middle|\boldsymbol{\theta}^{i-1}\right) = \sum_{m=1}^{M}\sum_{n=1}^{N}\log(\alpha_m)\, p\left(\mathbf{z}_m\middle|\mathbf{x}_n,\theta^{i-1}\right) + \sum_{m=1}^{M}\sum_{n=1}^{N}\log\left(f_{\mathbf{z}_m}(\mathbf{x}_n|\boldsymbol{\theta}_m^{i-1})\right)p(\mathbf{z}_m|\mathbf{x}_n,\theta^{i-1}) \quad (2.19)$$

This expression is important as it becomes the new objective function during the M steps. In general, $f_{\mathbf{z}_m}$ can take any form of PDF (which contains the transformation function). The prime goal of image registration is to estimate the current unknown parameters of interest in $f_{\mathbf{z}_m}$ by solving this maximisation problem. The details of the solution will be explored shortly after $f_{\mathbf{z}_m}$ takes a specific form introduced in the next section.

Equating the derivatives of Eq. 2.19 with respect to the mixing parameters α_m to zero, we arrive at:

$$\alpha_m = \frac{1}{N}\sum_{n=1}^{N} p\left(\mathbf{z}_m\middle|\mathbf{x}_n,\boldsymbol{\theta}^{i-1}\right) \quad (2.20)$$

If each of the clusters takes the form of a Gaussian PDF, analytical estimators for the mean and standard deviation in M steps exist (Bilmes 1997). These can be obtained by equating the corresponding derivatives of Eq. 2.19 to zeros.

GMMs are a well-known clustering approach in statistical learning. The EM-GMM algorithm employs soft assignment has been compared to the hard assignment used in well known k-means clustering method (Bishop 2006). An analogous relationship can be found between the GMM-based registration methods (discussed in the following section) and the ICP algorithm in the context of feature registration.

2.4.1.3 ICP, RPM, CPD and RASM

In this section, four popular methods in feature registration are summarised from an algorithmic point of view. The similarities between these methods are highlighted.

The original ICP algorithm (Besl et al. 1992;Zhang 1994) can be summarised as follows:

ICP Algorithm

for (i=0; i<N; i++)
{
1. Find correspondence by computing *nearest point*,
   w.r.t. the previous estimated transformation.
2. Estimate the (*rigid*) transformation using *adapted Procrustes analysis*,
   using the correspondence established in step 1;
3. Repeat until a convergence criterion or the maximum number of allowed iterations is reached.

}

Robust point matching (RPM) was first proposed by Chui et al. (Chui et al. 2002) as a non-rigid extension to the original point matching algorithm that featured soft assignment (Gold et al. 1998) and outlier rejection (Gold et al. 1998;Rangarajan et al. 1996). The soft assignment has also been re-formulated as a result of GMM (Chui et al. 2000). The non-rigid transformation is a group of radial basis functions, with TPS being a popular choice in many implementations. However, the EM solution for the mixture model in RPM is only an approximation and some practical enhancements, such as slack variables to handle outliers, have been made to overcome the well-known problem that GMMs are prone to outliers. It has been argued that RPM provides only approximations of the objective function and is not a real probability approach as the GMM needs to be adapted to allow an effective solution (Myronenko et al. 2006;Myronenko et al. 2010). The transformation can be estimated directly if other distance metric, such as the L_2 norm, between distributions of GMMs (Jian et al. 2005) is adopted. However, this again leads to an approximation without a clearly defined likelihood function.

RPM Algorithm

for (i=0; i<N; i++)
{
1. Find correspondence by computing *soft assignment* or *from mixture model*,
   w.r.t. the previous estimated transformation.
2. Estimate (*TPS-based non-rigid*) transformation by *least-squares on the kernel*,
   using known correspondence;
3. Repeat until a convergence criterion, such as the change of the objective function, or the maximum number of allowed iterations is reached.

}

The more recent coherent point drift (CPD) algorithm has been proposed (Myronenko et al. 2010) to set up a framework for using mixture models in point-based registration tasks. Most of the work introduced above can be unified using this framework. This is a pure probabilistic framework where the posterior probabilities in the E step and the complete log-likelihood function in M steps are both derived analytically. The objective function is a mixture of Gaussian and uniform distribution to account for outliers explicitly. Closed-form solutions for rigid and affine cases are provided while a variational solution to estimate the non-rigid, regularised transformation has also been derived (Myronenko et al. 2006;Myronenko et al. 2010).

CPD Algorithm

for (i=0; i<N; i++)
{
1. Find correspondence by computing *posterior probabilities of mixture model*, wrt. the previous estimated transformation.
2. Estimate (*Gaussian kernel-based*) transformation by *maximising the complete likelihood*, using known correspondence;
3. Repeat until a convergence criterion, such as the change of the likelihood function, or the maximum number of allowed iterations is reached.

}

Following the RPM formulation, Abi-Nahed et al. (Abi-Nahed et al. 2006) proposes robust active shape models (RASM) algorithm where the TPS is replaced with an active shape model (ASM), equivalent to the PDM described in Section 2.2.2.3. The intermediate solutions for the RPM were adapted to form a new energy function as the objective function in the M steps, but neither constraints nor the solutions were provided in the paper. A more rigorously explained and intensively validated method is described by Luo et al. (Luo et al. 2001;Luo et al. 2003), but the resulting method is quite similar to original RPM.

RASM Algorithm

for (i=0; i<N; i++)
{
1. Find correspondence by computing *soft assignment* / *mixture model*, wrt. the previous estimated transformation.
2. Estimate (*linear shape-based*) transformation by *least-squares on shape space*, using known correspondence;
3. Repeat until a convergence criterion, such as the change of the objective function, or the maximum number of allowed iterations is reached.

}

It is worth noting that the EM algorithm was not adapted rigorously by some authors, including RPM and those methods incorporating the ASM described above. Since the EM algorithm has been applied successfully for both feature- and intensity-based registration, it is possible to formulate the objective function probabilistically in order to understand the problem in a more principled manner. The underlying reasoning is that (feature) correspondence is usually unknown but does need not to be determined explicitly. This situation can be posed as a latent variable problem, which usually can be solved by the EM algorithm (Bishop 2006).

Some of the non-parametric methods based on regularising the displacement field may also be integrated within the generalised framework described above. In particular, the regulariser can be treated as a prior so that the problem becomes maximum a posterior (MAP) problem, which still can be solved by the EM algorithm with minor changes (Bishop 2006).

2.4.2 Model-to-Image Registration

At this point, it is worth distinguishing the model-to-image registration approach introduced in this thesis from alternative methods. Fundamentally, there is no particular difference between model-to-image registration and feature registration in terms of the underlying mathematical or physical principles. However, in practice, the method has been implemented so that the model typically contains prior information relevant to solving the registration and associated clinical problems – for example, the model may contain information on organ deformation and/or pathological/surgical information – whereas processing the target image is relatively simple, fast, automatic and unsupervised. This approach also enables computationally intensive processing to be focused on the source model. As another example, outliers usually need to be considered in the target image, but this may not be necessary for the source model. These features

constitute a significant difference when compared with general registration methods described in the literature.

This thesis describes such a model-to-image registration algorithm, where a patient-specific prostate motion model, built from training organ shapes derived from preoperative MR (or TRUS) images, is registered automatically to intraoperative 3D TRUS images. This enables preoperative information of cancer location and extent to be transferred to TRUS images that are used routinely for guiding minimally-invasive surgical procedures for diagnosing and treating prostate cancer.

Chapter 3 Statistical Motion Modelling - a Transformation Model

In order to register preoperative prostate magnetic resonance (MR) and intraoperative ultrasound images of the same patient, this thesis describes a model-to-image registration approach. The main motivation is that a physically plausible transformation model, which potentially provides useful constraints for the registration, is desirable for the registration because establishing an effective similarity measure is difficult between multi-modality images. In an ideal scenario, a similarity measure should provide an adequate measure of how good a transformation is so that fitted parameters with a higher value of similarity measure have a greater chance of representing a physically correct transformation. In this case, the objective function is considered well behaved and therefore should be easy to optimise. A well-constrained transformation model would help limit the search space of the spatial transformation so a "not-so-good" similarity measure could still be effective to lead to a good registration. This will be discussed further in Chapter 4.

This chapter describes details of building statistical motion models (SMMs) from prostate ultrasound and MR images. The proposed SMMs are learned from biomechanical simulations to provide such well-constrained transformation models. By constraining a registration algorithm (discussed in Chapter 4), these models are useful to be registered to intraoperative images. In the application of interest here, the aim is to provide fused TRUS and MR information during prostate interventions. The transformation model represents prior knowledge that approximates the real gland motion so that non-physical deformations can be avoided and the efficiency and robustness of the registration therefore are improved. Further discussion of the motivation of the proposed SMMs is provided in Section 2.2.2.4.

3.1 Related Work

3.1.1 Biomechanical Modelling

Biomechanical modelling using FEA, described in Section 2.2.2.2, has been previously applied for predicting prostate gland motion (Bharatha et al. 2001;Crouch et al. 2007;Hensel et al. 2007). However, the conventional application of this method requires knowledge of boundary conditions and tissue material properties, which are very difficult to estimate accurately *in vivo*. The mechanical properties of tissue are known to vary significantly between patients and different tissue types. Such variations can introduce significant errors when average

experimental values are used to predict organ motion as part of a registration scheme. Chi et al., for example, report a registration error of up to 4.5mm due solely to a 30% uncertainty in material properties for a solid FE model of the prostate gland (Chi et al. 2006). Similar results have been observed in the experiments presented in Section 5.1.

In most existing work, a mesh representing the gland is required, and the displacement of the surface of the prostate gland is estimated using a surface registration method. FEA then estimates the internal nodal displacements with respect to the surface displacement being loaded as the boundary conditions. Therefore, the gland motion predicted is subject to 1) the surface registration "driving" the FE model; and 2) the approximated constitutive model (i.e. material properties (Bharatha et al. 2001)). To date, there are a number of deformable registration methods described in the literature that have adopted this methodology. Some of these have been applied to the problem of registering MR images of the prostate acquired at different times, with and without using an endorectal coil (Alterovitz et al. 2006;Baowei et al. 2003;Bharatha et al. 2001;du Bois et al. 2004).

In a number of proposed methods (Alterovitz et al. 2006;Bharatha et al. 2001;Hensel et al. 2007), a biomechanical model is used to constrain the allowable deformations to be physically plausible. Crouch et al. (Crouch et al. 2007) describe a method for automatically generating a volumetric FE mesh of the prostate gland, together with appropriate boundary conditions, and validate the method for registration using CT images obtained with and without an endorectal MR imaging coil in place. They also address the effect of gland swelling following brachytherapy seed implantation.

Another interesting attempt is to pose the unknown boundary conditions and material properties as unknown parameters in the image registration problem (also discussed in Section 2.2.2.2). Numerical optimisation then is employed for optimal values to maximize the similarity measures between two sets of image data (Alterovitz et al. 2006). However, this study only reported results on 2D data. Further sensitivity studies of the optimised material properties and a larger patient study have not been reported. Difficulties might include: 1) that this is a typical ill-posed problem, where an adequate regulariser is usually difficult to find; and 2) that this approach demands substantial computational resources, which become impractical in 3D.

Recent developments in fast computational techniques for FE analysis utilise graphical processing units (GPUs), e.g. (Taylor et al. 2008), and make FEA methods more practical for simulating soft-tissue motion during surgical procedures but, in general, simulations are still challenging for time-critical image registration applications in which at least one FEA simulation is performed during each iteration of a numerical registration optimisation algorithm.

3.1.2 Statistical Shape Modelling

SSMs, described in Section 2.2.2.3, provide a low-dimensional description of variations in organ shape across a population and have been widely used for image segmentation tasks (Heimann et al. 2009). This modelling approach has been applied to segmentation of the prostate gland from CT (Dam et al. 2008), MR (Makni et al. 2009;Tsai et al. 2003;Tsai et al. 2004) and TRUS (Cosio 2008;Shen et al. 2003;Wu et al. 2000) images. The conventional approach to generating SSMs is to use shape information derived from a series of sample images which serve as training data. The same approach can be applied for constructing a statistical model of organ motion – an SMM – but replicating and imaging organ motion *in vivo* in order to generate a sufficiently large training dataset is often impractical or impossible. For instance, where a TRUS probe is the primary source of prostate motion from its "resting state" during a diagnostic MR scan, simulating this motion during MR imaging would be highly challenging, partly because replicating the lateral or lithotomy patient position adopted during TRUS-guided procedures inside an standard diagnostic MR scanner is usually not possible, and partly because performing multiple scans across the range of probe positions, orientations, and balloon diameters that may be encountered during TRUS-guided procedure would be time-consuming unless the patient position and probe insertion can be standardised in some way, which in practice is difficult to achieve.

3.1.3 Combined Biomechanical-Statistical Modelling

One computational solution to the above problem is to synthesise training data by using biomechanical modelling techniques to simulate organ motion (Davatzikos et al. 2001). This approach has the advantages that a large amount of training data can be generated easily and automatically, and that a wide range of deformations and boundary conditions that might be encountered in practice can be considered, without the need for standardising the conditions under which gland motion occurs. In addition, the approach is highly flexible since in principle it can be applied to any deformation that can be reasonably modelled.

Furthermore, combining statistical analysis techniques and biomechanical modelling overcomes these problems by enabling variability and uncertainty in tissue mechanical properties to be captured within an SMM by including variability in the training data. The application of multivariate statistical methods, such as PCA, further allows a low-dimensional (and therefore computationally efficient) model of organ motion to be produced, which is well-suited to registration applications.

This approach, originally proposed by Davatzikos et al. (Davatzikos et al. 2001), was adopted by Mohamed et al. (Mohamed et al. 2002) to construct a statistical model of prostate motion due to differences in TRUS probe poses. In this proof-of-concept study, the deformations of patient-specific FE models of prostate glands were simulated using varying boundary conditions determined by the position and orientation of the TRUS probe. In the earlier work of Alterovitz et al. (Alterovitz et al. 2006), material properties and external forces were estimated using optimisation of the FE model derived from 2D MR images to predict prostate motion.

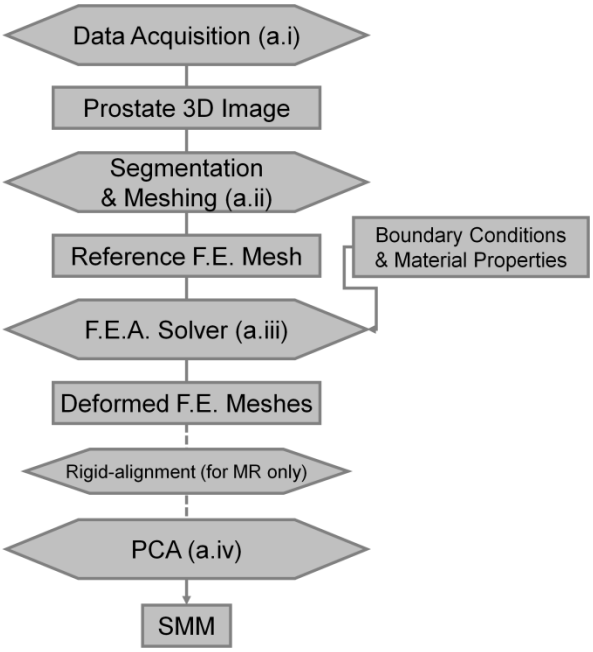

Figure 3.1 A flowchart for an overview of the modelling method

Figure 3.1 provides a schematic overview of the model building process, the first one of the two stages of the algorithm developed in this thesis. This stage includes the following steps:

a.i) For a *TRUS-derived SMM* that represents ultrasound-probe-induced prostate motion, a three-dimensional ultrasound image is acquired at the beginning of a procedure, usually before

the balloon is expanded. The balloon covered on the ultrasound probe contains saline to provide acoustic coupling. In practice, expanding the balloon and/or moving the probe upwards can further improve acoustic coupling and improve the image quality. However, the expansion of the balloon and the probe pressure are considered main sources of prostate gland motion. Alternatively, a T2-weighted MR image can be used to provide anatomical information for building an *MR-derived SMM*;

a.ii) Build a patient-specific FE mesh of the prostate gland and surrounding anatomy (if visible) from the source image;

a.iii) Perform a series of FEA simulations of gland motion using randomly sampled material properties and boundary conditions which correspond to different possible positions and orientations of the TRUS probe during the procedure;

a.iv) Construct a TRUS-derived SMM by directly applying PCA to the predicted FE mesh node displacements. Alternatively, an MR-derived SMM is constructed followed by a rigid alignment (with respect to a reference mean) of the corresponding mesh node positions.

The purpose of building a TRUS-derived SMM is threefold: 1) it is a better controlled situation, where only movement of the probe and very limited patient motion exist. These two are major causes of the deformation between a source image and the target intraoperative ultrasound image; 2) it is much more practical to validate the model by identifying visually traceable anatomical landmarks between ultrasound images than between MR and ultrasound images; 3) a TRUS-derived SMM is useful by itsself in a number of applications, where the intraoperative motion is the subject of interest.

The differences between the TRUS-derived- and the MR-derived SMMs are: 1) some surrounding structures, such as pelvic bones and bladder, are partially invisible in TRUS image due to the limited field of view. Therefore, the full FE model for the SMM resorts to approximation of the patient-specific anatomy; and 2) the dimension reduction method (i.e. PCA here) is applied on displacements and node positions, respectively. However, a simplified geometric representation of the FE model is introduced and validated that makes the geometric differences trivial in real applications (see Section 3.2.5).

In this chapter, details of building a combined statistical-biomechanical model to estimate the patient-specific motion are described. They are referred as TRUS-derived SMM and MR-derived SMM for ultrasound and MR images, corresponding to whether the model is derived from TRUS or MR images, respectively.

3.2. Finite Element Analysis

3.2.1 Segmentation

3.2.1.1 Segmentation of Prostate Gland in TRUS

Each TRUS image slice was segmented using manual contouring with a graphical user interface (GUI) developed by the author using MATLAB (The Mathworks Inc., MA, USA). As illustrated in Figure 3.2, contours were defined for the prostate capsule surface and for the boundary that differentiates the periurethral tissue, central- and peripheral zones, based on visual differences in texture and intensity between the regions. This boundary separates the prostate into two regions, an inner gland and an outer gland (IG and OG, respectively), as shown in Figure 3.2. This is important for the FE modelling as it permits the two regions to be assigned different elastic properties, which reflects surgical and pathological experience that the peripheral zone is more compliant than the inner part of the prostate (Bharatha et al. 2001;Cochlin et al. 2010). Points defining the apex and base of the gland were also identified manually with the segmentation software.

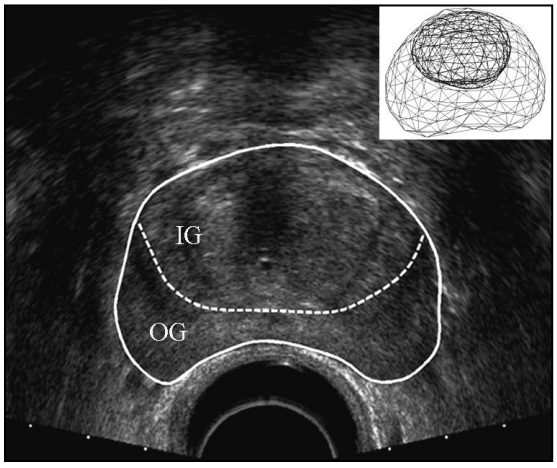

Figure 3.2 An example of a transverse TRUS image of the prostate with a manually segmented capsule contour (solid line) and the boundary between the inner gland and outer gland regions (dashed line), labelled IG and OG, respectively. The final surface meshes derived from the segmented contours are shown in the top right.

The surface of the transrectal balloon is well defined in TRUS images. In this thesis, the balloon was segmented automatically (using the algorithm described below) and modelled as a cylinder, and was included in the FE model. The diameter and position of the cylinder in the reference TRUS images were used to set the reference diameter and position of the balloon in the FE model (see details in Section 3.2.4).

The balloon segmentation process used was as follows: The point corresponding to the TRUS probe axis was determined as the intersection point of the extreme radial scan-lines at the edges of the sector image. To detect the balloon edge, TRUS image slices were first filtered using a median filter to suppress noise. A Canny filter with a high normalised threshold (0.4) was then used to find the edges of the balloon surface (see Figure 3.3a). To detect edges far away from the likely surface position of the balloon, only edge pixels within a predefined distance range relative to the probe axis were considered. For example, for the B-K ProFocus probe used in this work the range was set to 10-20mm perpendicular to the probe axis. A circle centred on the probe axis was then fitted in a least-squares sense to the extracted edge points within the range using a fitting algorithm (see Figure 3.3b). To ensure robustness, a simple outlier rejection scheme was included into the fitting algorithm in which 10% of the points with the largest distance from the fitted circle were removed automatically during each iteration until the root-mean-square (RMS) point-to-surface distance errors fell below a threshold of 3 pixels. Using this method, the circle fitting converged within 5 iterations. Finally, a cylinder was fitted by averaging the centres and the radius of the detected circles. An example of reconstructed prostate (see Section 3.2.2) and balloon surface meshes is shown in Figure 3.4.

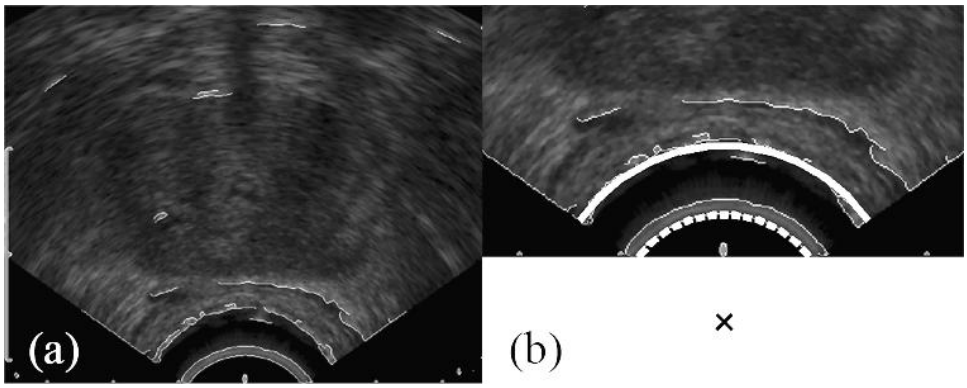

Figure 3.3 (a) A TRUS image overlaid with a Canny edge map; (b) The fitted balloon surface (white solid curve), modelled as a circular arc centred at the intersection of the image plane, and the central axis of the TRUS probe (denoted by the black cross). The probe surface is indicated by the white dashed curve.

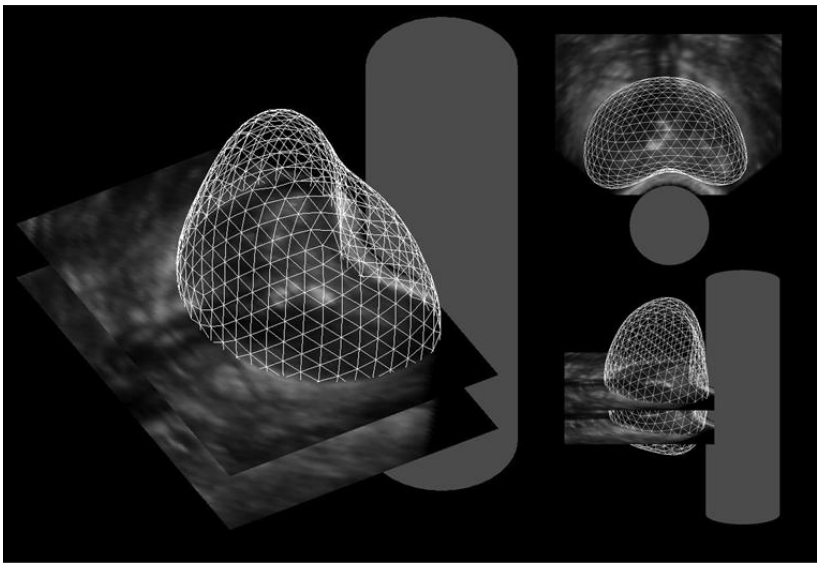

Figure 3.4 Three views of a triangulated prostate gland surface mesh and TRUS probe balloon segmented from parallel TRUS images. The balloon is modelled as a straight cylinder.

In general, the pelvic bone and bladder are only partially visible in the limited TRUS field of view. Therefore, a generic pelvic model is used (see Figure 3.5) and the effect from the bladder is assumed to be negligible. This will be discussed further in Sections 3.2.3 and 3.2.4.

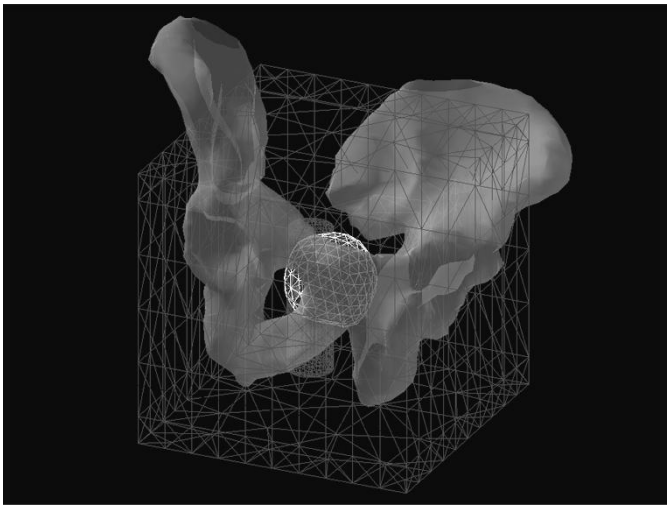

Figure 3.5 A FE mesh of the prostate gland constructed from 3D TRUS data shown in relation to a generic surface model of the pelvic bone, in order to provide rigid constraints for FE simulations. The surrounding soft tissue is modelled as a homogeneous block.

3.2.1.2 Segmentation of Multiple Organs in MR

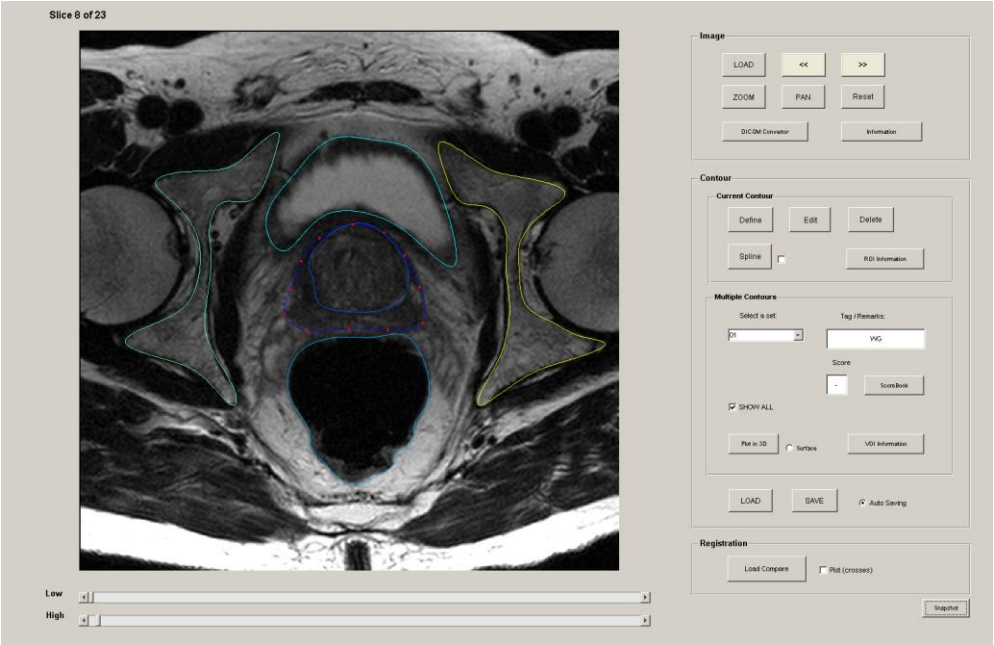

Figure 3.6 An illustration the GUI used to segment multiple contours in an MR slice, a transverse slice through a T2-weighted MR image of the prostate showing manually delineated contours used to segment the prostate gland, the rectum, the pelvis and the bladder.

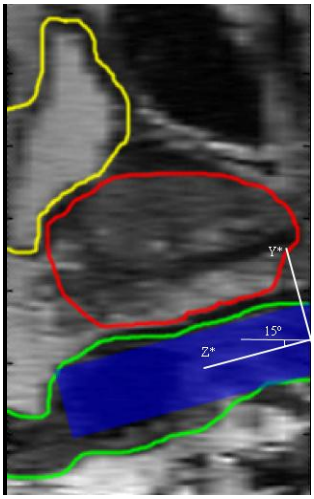

Figure 3.7 An illustration of the local TRUS probe co-ordinate system shown on a sagittal prostate MR image. The prostate gland, rectal wall, probe and bladder are shown in red, green, blue and yellow, respectively. The local reference co-ordinate system was defined with the z-axis orientated at 15 degree relative to the cranial-caudal axis.

For the purposes of this thesis, diagnostic MR images were segmented by manually defining contours on transverse slices using the MATLAB GUI (see Figure 3.6). The segmentation process was time-consuming (typically taking 45 minutes per patient), but was the most accurate method available for segmenting pelvic anatomy. The outer surface of the prostate gland

capsule was segmented, and the gland itself divided into the central- and peripheral zones, which are usually clearly visible in T2-weighted MR images. The pelvic bone, the rectum, and the bladder at the base of the prostate were also segmented (see Figures 3.6, 3.7 and 3.8).

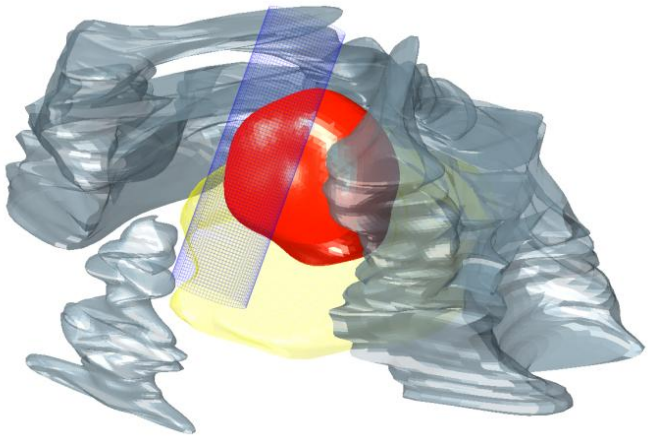

Figure 3.8 An illustration of surface meshes obtained by segmenting an MR image. The TRUS probe (with sheath), approximated by a cylinder is shown in blue. The prostate gland, the pelvis, and the bladder are shown in red, grey and yellow, respectively.

3.2.2 Finite Element Meshing

3.2.2.1 Surface Meshing

Comparing to other potential methods (discussed in Shape Representation, Section 2.2.2.3), spherical harmonic (SH) provides a compact parametric form that is well-suited to represent a smooth, start-shaped organ (Zacharopoulos 2005), such as prostate gland (Tutar et al. 2008). As shown in Figure 3.9, the prostate gland surface was represented by a SH surface fitted to the transverse contours. The contours are first converted into a binary volume. Surface points then are sampled from the binary image and fit an SH surface using the method that described by Tutar et al. (Tutar et al. 2008). To obtain a smooth and uniformly sampled surface, suitable for generating a high quality mesh for FEA, the following adaptive sampling scheme, similar to the one described in Zhou et al. (Zhou et al. 2004), was implemented. The SH surface was first filtered in the frequency domain using a trapeziform low-pass function (Zhou et al. 2004) before being meshed into triangles by projecting a uniformly triangulated sphere template. Refinement of the triangulated mesh was performed by maximising the sum of a triangle quality measure over the surface using a quasi-Newton numerical optimisation algorithm, implemented in MATLAB (Zacharopoulos 2005). The smoothness of the final surface mesh is controlled by the degree of the SH, the coefficients of the filter, and the density of the mesh. Values for these

parameters were set experimentally such that the surface appeared smooth visually with the constraint that the maximum absolute distance (MAD) between the reconstructed surface and the original contour points was less than 1.0mm (Note that, as reported in Tutar et al. (Tutar et al. 2006), the maximum inter-observer error was found to be significantly greater than this value). Definition of the apex and base points was found to be important for producing a geometrically accurate surface. These were defined immediately adjacent to the available contours to maintain a topologically correct gland surface. An example of a smoothed SH representation of a prostate gland, reconstructed from TRUS contours, is illustrated in Figure 3.9d.

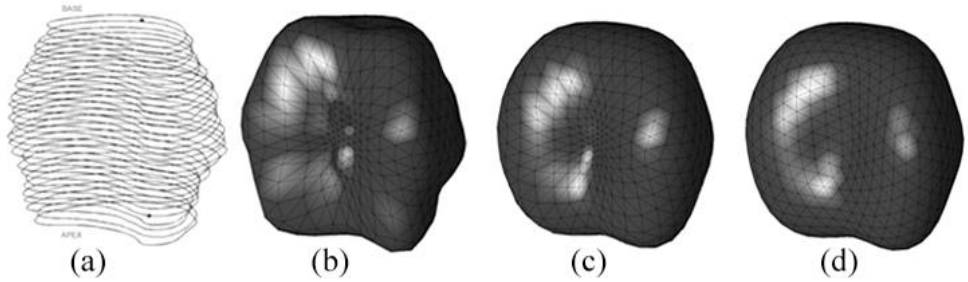

Figure 3.9 Reconstruction of a smooth, triangulated SH surface from manually drawn prostate contours: (a) original contours with apex and base points; (b) initial fitted SH surface; (c) filtered SH surface; and (d) surface in (c) following mesh refinement.

As described in Section 1.1, a zonal structure of prostate gland that is visible in TRUS images is different from that in MR images. In this thesis, inner/outer gland and central/peripheral zone are considered for TRUS-derived- and MR-derived SMMs, respectively. For TRUS-derived SMM, the user-defined boundaries separating the inner- and outer glands regions (see Figure 3.2) were not smoothed and used simply to label tetrahedra of the FE mesh according to whether they lied within the inner or outer parts of the gland. This allows the assignment of different material properties for different regions (see Section 3.2.3). The segmentation obtained from MR image (see Figure 3.6) was used to separate central- and peripheral zones for MR-derived SMM.

In a 3D FE analysis, surface meshing is not necessary but useful for the subsequent solid meshing as a surface mesh provides a simple, discrete and unambiguous representation of regions of interest, especially comparing to other representations, such as splines, point clouds and binary volumes.

3.2.2.2 Solid Meshing

For TRUS-derived SMM, the tissue surrounding the prostate was modelled as a homogeneous block with dimensions 20×20×20 cm^3 (see Figure 3.5) due to a limited field of view of TRUS images. These dimensions are large enough to contain a normal human lower pelvis region. For the MR-derived SMM, the surrounding tissue uses the MR image sections (see Figure 3.8) which adequately cover the same region. The surface meshes and the block structure were imported into a commercial FEA software package (ANSYS). A linear four-node tetrahedral FE mesh was then constructed automatically using trimmed parametric surfaces and Delaunay tessellation techniques provided by the software. Only the solid meshing tool of ANSYS was used in this work; although ANSYS is a general purpose FEA package, an alternative fast FE solver was employed to compute mesh node displacements, as described in Section 6.2.1. For each patient case, the mesh comprised approximately 35,000 – 100,000 elements. Volumetric regions corresponding to the inner prostate gland, the outer prostate gland, the rectal wall, and surrounding tissue were individually labelled and attributed with different material properties, as described in the next section.

Using the refinement tool available in ANSYS, the region around the rectum was re-meshed to obtain high element density in this region. This enabled the TRUS probe – or more precisely, the fluid-filled sheath placed over the TRUS probe, approximated by a cylinder – to be modelled directly in each simulation without the need for re-meshing.

There are other meshing tools available to generate the solid tetrahedron mesh in the field. For instance, Tetgen (Si 2006) is an open source tool to generate quality 3D meshes from surface meshes. On the other hand, a general purpose meshing method for structural meshes, such as four node hexahedrons, is still under active development (El-Hamalawi 2001). This practical consideration is the main motivation for adopting tetrahedron elements in this work.

3.2.3 Material Properties

In the literature on modelling biomechanical tissue motion, the tissue mechanical properties are typically assigned fixed values based on the results of *ex vivo* experiments. A few studies have attempted to determine the mechanical properties for prostate tissue (e.g. (Krouskop et al. 1998)). In related work by Bharatha et al. (Bharatha et al. 2001), linear material properties for the human brain were assumed for modelling prostate deformation. However, *ex vivo* properties are often poorly representative of the corresponding properties *in vivo*, and

accurately measuring *in vivo* mechanical properties is extremely difficult in practice. To the best of the author's knowledge, such *in vivo* experiments for human prostate gland have not been reported. Furthermore, there is likely to be considerable variation in tissue properties between individuals, particularly for diseased tissue. To account for this, in this thesis, tissue material properties were included as variable parameters in the generation of training data for the prostate SMM. Given the variability and uncertainty associated with published material properties, sample values are sampled from a relatively wide range, consistent with the range normally applied for soft-tissue modelling (Carter et al. 2005). It is important to note, however, that the prediction of displacements in the FEA is only dependent on the ratio of elasticity moduli assigned to different compartments and not on their absolute values. The uniform ranges used in this thesis are given in Table 3.1.

Description	Parameter(s)	Range	Reference Value(s)	DOF
Balloon radius	R	$[0.9R_0, 1.5R_0]$*	R_0*	1
Balloon translation	Tb_x, Tb_y, Tb_z	[-5, 5] mm	$Tb_x = Tb_y = Tb_z = 0$ mm	3
Balloon rotation	ϑb_x, ϑb_y, ϑb_z	[-10, 10] °	$\vartheta b_x = \vartheta b_y = \vartheta b_z = 0°$	3
Pelvis Scaling****	S	[0.8, 1.2]	$S = 1$	1
Pelvis translation****	Tp_x, Tp_y, Tp_z	[-10, 10] mm	$Tp_x = Tp_y = Tp_z = 0$ mm	3
Pelvis rotation****	ϑp_x, ϑp_y, ϑp_z	[-15, 15] °	$\vartheta p_x = \vartheta p_y = \vartheta p_z = 0°$	3
Shear modulus	G_1, G_2, G_4**	[3.36, 76.9] kPa	–	4
	G_3***	[3.36, 67.1] kPa		
Bulk modulus	K_1, K_2, K_4	[8.33, 3.33x10^3] kPa	–	4
	K_3***	[0.17, 3.33] GPa		

* R_0 denotes the radius of the balloon measured from the source image.
** The subscripts *1-4* correspond to the prostate central zone/inner gland (1), the peripheral zone/outer gland (2), the rectal wall (3), and the surrounding tissue (4), respectively.
*** The rectal wall in contact with the balloon is assumed to be nearly incompressible.
**** For the generic pelvic model used in TRUS-derived SMMs only.

Table 3.1 Material properties and boundary conditions used for FE simulations. The ranges of the material properties and the boundary conditions have been assigned based on plausible values as well as on the observations. See detailed discussions in Sections 3.2.3 and 3.2.4.

The element groups, which are modelled using different material properties and/or are assigned different types of nodal displacements, are referred as compartments. For MR-derived SMM, these compartments include the central- and peripheral zones of prostate gland, the rectum, the surrounding tissue, the pelvic bones and the TRUS probe. In the case of TRUS-derived SMM, the central zone and peripheral prostate zone are replaced by the inner gland and outer gland,

which are visible in the TRUS image, respectively. These different compartments are segmented as described in Section 3.2.1. In practice, elements within the same compartment of the FE model were labelled according to the corresponding tissue type. Different material property can then easily be assigned to the corresponding compartment. All the organs are assumed to be geometrically connected to the surrounding tissue. The pelvis provides a geometrically realistic, rigid constraint, which balances the driving force exerted by the movement of the TRUS probe.

All the materials were assumed to be linear in initial work (Hu et al. 2008a;Hu et al. 2008b), and later were changed to be nonlinear (Hu et al. 2011a). In both cases, a nonlinear solver, such as the fully nonlinear total Lagrangian explicit finite element formulation (Taylor et al. 2008) used in this thesis, is essential, as a larger deformation breaks the linear assumption of geometry despite the linear material model. Because there is a lack of studies in the literature pointing to any particular model suitable for modelling prostate gland motion, a simple linear elastic model and a hyperelastic neo-Hookean model with two parameters were used. The neo-Hookean provides a relatively simple formulation to predict the nonlinear strain-stress behaviour of hyperelastic material undergoing large deformation (Zienkiewicz et al. 2000). Although exact behaviour of soft tissue is expected to be complex and nonlinear, it may be argued that the exact formulation of the material model is not important in this application where only the variance of the motion is of interest.

3.2.4 Displacement Loadings

Because forces, or equivalently pressures, are difficult to estimate from medical images (see discussions in Section 2.2.2.2), boundary conditions were specified by mesh node displacements on a subset of all the finite element nodes. Two sources of prostate deformation were considered: the expansion of the TRUS balloon and a change in the pose of the TRUS probe/balloon. Further boundary constraints were imposed on the pelvic bone surface so that the magnitude of these nodes had a displacement of zero. Slippages between organ surfaces and between the TRUS probe and rectal wall were not modelled.

For the FE simulations, the expansion of the balloon was modelled by applying a radial displacement to the cylinder surface nodes. Since the position and orientation of the TRUS probe in the rectum is unknown before a procedure, the cylinder representing the balloon surface was also repositioned in each simulation by applying a rigid-body transformation, resulting in 6 additional DOFs.

For building TRUS-derived SMMs, in general, only a small part of the pelvic bone is visible in TRUS images and therefore it was not possible to determine the shape or location relative to the prostate of the pelvic bone for each patient. To approximate the boundary conditions at the pelvis surface, a surface model of an average male pelvis, derived from CT images and developed by Thompson et al. (Thompson et al. 2008), was used to fix the FE mesh node positions at the bone surface. The reference position and orientation of this model with respect to the prostate was calculated using the method described by John et al. (John et al. 2005) and Sung et al. (Sung et al. 2007).

The uniform ranges of the boundary conditions used in this thesis are based on empirical values which can produce plausible scenarios and are summarised in Table 3.1.

3.2.5 Simplified Finite Element Models

As introduced in Section 3.1.3, the aim of the multiple FE simulations is to provide training data for later statistical analysis. In particular, building MR-derived SMMs requires patient-specific segmentation of multiple organs. Although a number of semi- and fully-automatic segmentation algorithm have been proposed, this section describes an alternative to the segmentation for reducing the burden of manual delineation and therefore making patient-specific SMM more clinically practical. Specifically, a geometrically simplified FE mesh, in which, some anatomical structures are replaced by equivalent structures with a simplified geometry, or omitted completely, is proposed. This strategy is inspired by the observation that since a PCA-based SMM trained using a set of deformed FE meshes captures the statistical variation in mesh node displacements, adopting a geometrically simplified mesh may not affect the characteristic parameters (i.e. the mean and variance of a Gaussian distribution) of this distribution significantly. Therefore, the accuracy of the final MR-derived SMM may not be compromised significantly by adopting a simplified mesh when generating the training data. Only the MR-derived SMM is considered for this simplification in this thesis as an example.

The change of material properties and/or boundary conditions is expected to affect significantly the individual simulation (also, see the results presented in Section 5.1). However, the impact of the simplified FE models is investigated by comparing the accuracy of MR-derived prostate SMMs built using different simplified FE mesh geometries with a reference model built from training data simulated using an FE mesh in which the geometry of the prostate, rectum, bladder and pelvic bone are all accurately defined. The details of these comparisons are

presented in the following sections. The results to assess the effect of the SMMs based on simplified geometries are presented in Section 6.2.

For each patient, a *fully-specified* FE mesh was used to build a reference (control) SMM (see Figure 3.10 and 3.11). This fully-specified FE model was based on FE simulations that consider the prostate gland, pelvic bone, rectum, and bladder segmented fully from a MR scan as distinct, homogeneous structures, as shown in Figure 3.6. The corresponding SMM was generated by randomly assigning boundary conditions and elastic properties for each tissue type, and computing the subsequent deformations.

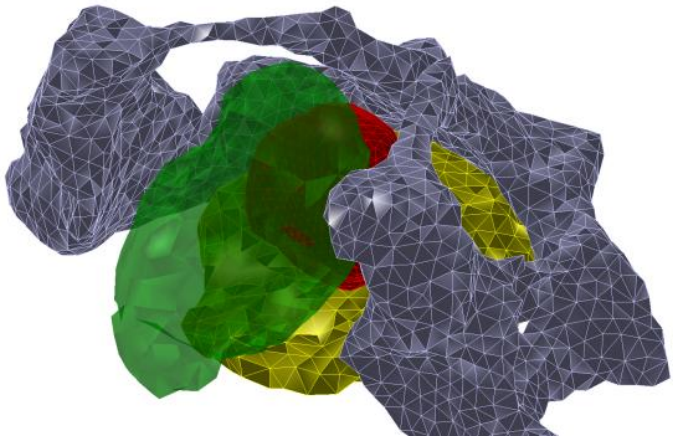

Figure 3.10 An illustration of surface meshes of gland (red), bladder (yellow), rectum (green) and pelvis (grey).

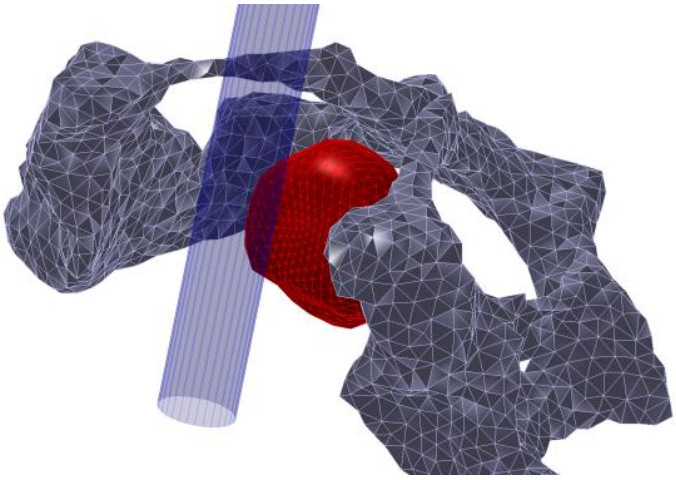

Figure 3.11 An illustration of TRUS probe (blue cylindrical structure) position relative to the prostate gland and the pelvis.

SMMs based on FE simulation data were also built by reducing the number of soft-tissue compartments in the model (equivalent to assigning identical material properties to adjacent compartments in the fully-specified model) and/or simplifying the geometry of the pelvic bone.

Either of these simplifications directly reduces the amount of prerequisite segmentation required to build an SMM from FE simulations.

Material Properties

In the FE simulations, all soft tissues were assumed to behave as isotropic, elastic materials described by a neo-Hookean model (Zienkiewicz et al. 2000). Since the values of the elastic properties of each tissue type were assumed to be unknown, the material properties for each of the four soft-tissue compartments were assigned randomly sampled values within the physiological ranges given in Table 3.1. The usual condition of incompressibility ("equivalent" Poisson's ratio = *0.5*) was not assumed because it can be argued that this is not appropriate for organs such as the prostate, rectum and bladder, which are compressible due to gain and loss of blood and other fluids, as well as the presence of cavities.

Material properties were assigned in two ways, depending on number of organs that need to be segmented as follows:

MP1: In the first case, material properties are assigned independently to each of the segmented soft-tissue five regions – i.e., the rectal wall, the bladder, the central- and peripheral zones of the prostate gland, and the surrounding tissue (assumed to be homogeneous).

MP2: In the second, simpler case, i) the prostate gland and ii) surrounding organs and tissue are treated as two single homogeneous materials.

Boundary Conditions

Two types of boundary conditions were considered in this thesis: the rigid constraint imposed by the pelvic bone and the position and orientation of the TRUS probe. In one configuration of the simplified FE model investigated in this thesis, the pelvic bone was approximated by three boundary planes, as shown in Figures 3.12 and 3.13. This choice of representation was motivated by the need for a clinically practical method for approximating the bony constraints within the pelvis.

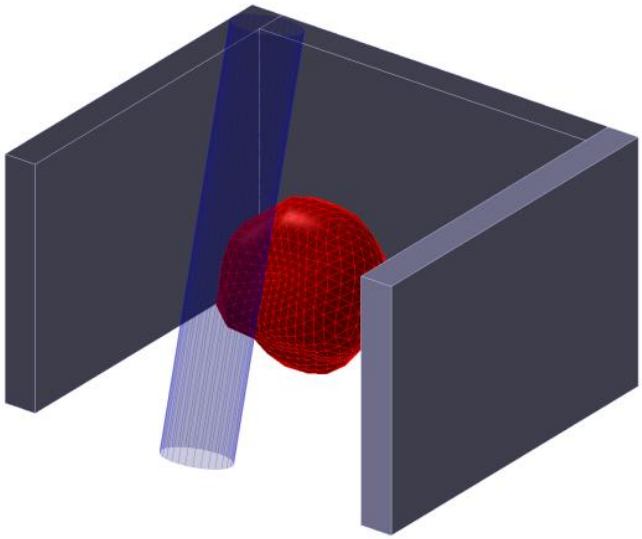

Figure 3.12 An illustration of the three-plates-structure (grey plates) relative to the positions of prostate gland (red mesh) and TRUS probe (blue cylinder).

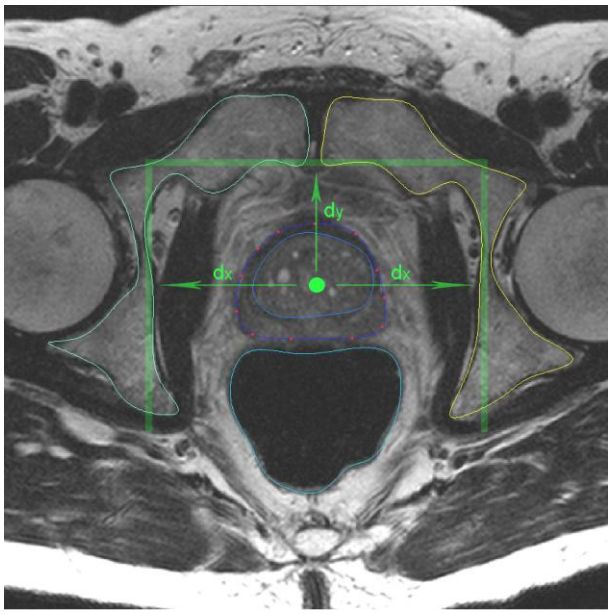

Figure 3.13 illustration of the three-plates-structure (green lines) in the transverse MR slice and the distance measures d_x and d_y are also demonstrated.

The positions of these planes for an individual patient were determined by measuring two distances, d_x *and* d_y, in the approximately mid-gland transverse plane of the MR image, as shown in Figure 3.13. Assuming that the prostate capsule has been segmented, d_x is the average of the two distances measured along the left-right axis from centre of mass of the prostate gland to the nearest intersections with the axis on the left and right sides of the pelvis. Distance d_y is the distance from the prostate centre of mass to the nearest point on the posterior side of the pubis

along the anterior-posterior axis. In this thesis, these distances were computed automatically using the segmentation of the pelvic bone, but, importantly, both can be easily measured without needing to segment the pelvis. The displacement at each mesh node of the pelvic bone, or alternatively the surrogate planes, was fixed to zero for all simulations.

In the experiments described below, three different pelvic boundary conditions – referred to as BC1, BC2, and BC3 – were used. These are defined as follows:

BC1: An anatomically realistic, patient-specific pelvic bone. This requires complete segmentation of the bone on MR.

BC2: Three planes placed according the patient-specific measurements, as described above. This requires only simple measurements from an MR image.

BC3: Three planes placed at fixed positions determined by the average measurement calculated for the remaining 6 patients in the test dataset. Setting this boundary condition only requires segmentation of the prostate capsule (in order to compute the centre of mass of the gland).

As the driving force for the prostate motion, the size and 3D motion of the TRUS probe were specified in terms of the diameter of the water-filled sheath surrounding the probe, and the motion with respect to a local 3D co-ordinate system, defined with respect to an initial reference position (see details in Section 3.2.4).

Simulation of Soft-tissue Motion

Biomechanical simulations of TRUS-probe-induced prostate motion were performed to provide synthetic training data for the SMMs (see an example of such a simulation in Figure 3.14). The ranges of the assigned boundary conditions (BC1) and material properties (MP1) for the fully-specified FE model are summarised in Table 3.1.

To investigate the effect of using simplified FE models to generate the training data, different configurations of boundary conditions (BC1, BC2 and BC3) and material properties (MP1 and MP2) were compared, resulting in a total of 6 different SMMs for each patient. The tissue types, pelvic constraints, corresponding required segmentations and measurements are summarised in Table 3.2. The detailed experiments and results will be described in Section 6.2.

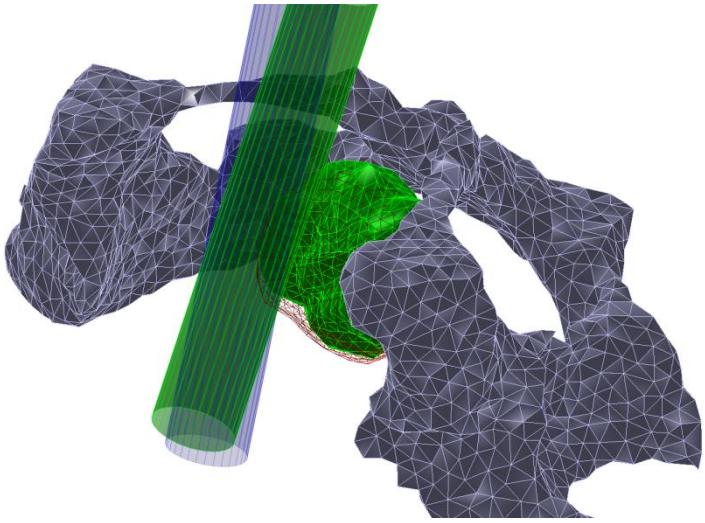

Figure 3.14 An illustration of displaced TRUS probe (green cylindrical structure) position relative to the deformed prostate gland using FE simulation (shown in green mesh) and the pelvis.

Model	Material Properties	Pelvic Constraints	Required Segmentation and Measurements
SMM 1	*All soft tissues*	*Real Pelvis*	*CZ, PZ*, bladder, rectum and pelvis*
SMM 2	*All soft tissues*	*Patient-specific plates*	*CZ, PZ*, bladder, rectum and measurements***
SMM 3	*All soft tissues*	*Generic plates*	*CZ, PZ*, bladder and rectum*
SMM 4	*Gland and ST****	*Real Pelvis*	*Gland and pelvis*
SMM 5	*Gland and ST****	*Patient-specific plates*	*Gland and measurements***
SMM 6	*Gland and ST****	*Generic plates*	*Gland only*

* CZ and PZ – central zone and peripheral zone, respectively;
** Measurements refer to the distance measurements to place the boundary planes described above;
*** ST – surrounding tissue.
Table 3.2 Summary of different configurations used in simulations

3.2.6 Summary of Assumptions in Finite Element Analysis

Prostate gland motion between MR and TRUS imaging sessions involves two transformations: firstly, there is a change in patient position due to the fact that MR imaging is performed in the supine position, whilst intraoperative TRUS is generally performed in the lithotomy position; secondly, there is a transformation due to the placement of the TRUS probe in the rectum. For simplicity, it was assumed that the first transformation is approximated by a rigid-body

transformation of the pelvis. Therefore, the position and orientation of the prostate apex-base axis relative to the anus and distal section of the rectum, adjacent to the prostate, remain unchanged. This enables the use of the geometry of the prostate (and other organs) segmented from an MR image as the initial (or resting) state for the finite element simulations. However, in reality, there is likely to be some tissue motion solely due to the change in patient position, which may change the orientation of the anus and rectum relative to the prostate.

It is assumed that the shape change of the prostate gland due to the change from the supine to lithotomy position is sufficiently small to be captured by a model of prostate motion that only describes explicitly the deformation due to the manipulation of the TRUS probe. It is also assumed that the range of possible orientations of the TRUS probe, modelled in the FE simulations, is wide enough to capture changes in the relative orientation of the prostate and rectum/anus that may occur when there is a change in patient position.

3.3 Statistical Motion Models

3.3.1 Principal Component Analysis-based Statistical Motion Models

The PCA-based dimension reduction method, described in Section 2.2.2.3, is applied on the displacements and node positions, for TRUS- and MR-derived models, respectively.

3.3.1.1 TRUS-derived Statistical Motion Model

Given N simulated gland deformations (here, $N = 500$), the 3D displacement of every node in the prostate gland mesh was calculated. The components of these displacements were combined with the balloon radius to form a vector $\mathbf{d}_n$, defined (for the n^{th} simulation) as $\mathbf{d}_n = [\boldsymbol{\delta}_1^T, \boldsymbol{\delta}_2^T, \dots, \boldsymbol{\delta}_M^T, R]_n^T, 1 \le n \le N$, where M is the number of gland mesh nodes and $\boldsymbol{\delta}_j^T = [\delta_x, \delta_y, \delta_z]$ is the 3D displacement vector for j^{th} $(1 \le j \le M)$ node. R is the additional variable indicating the radius of the balloon/probe used in this simulation. The principal modes of variation in random vector $\mathbf{d}$ are calculated by finding the eigenvectors of the covariance[2] matrix $\mathbf{C}$, given by:

$$\mathbf{C} = \frac{1}{N-1}\sum_{n=1}^{N}\left(\mathbf{S}\mathbf{d}_n - \bar{\mathbf{d}}\right)\left(\mathbf{S}\mathbf{d}_n - \bar{\mathbf{d}}\right)^T \quad (3.1)$$

where

[2] Here, $\mathbf{C}$ is an unbiased estimator of the covariance matrix and is different than, but converges to (given large sample size), its definition in Eq. 2.11.

$$\bar{\mathbf{d}} = \sum_{n=1}^{N} \mathbf{S}\mathbf{d}_n. \tag{3.2}$$

In Eqs. 3.1 and 3.2, $\mathbf{S}$ is a diagonal scaling matrix in which the diagonal elements, S_k, are set to $1/\sigma_k$, where σ_k is the standard deviation over N values of the k^{th} element of $\mathbf{d}_n$, $1 \leq k \leq 3M+1$. Now, if p_i is the eigenvector corresponding to the i^{th} largest eigenvalue of $\mathbf{C}$, and b_i is the corresponding scalar weight, then the node co-ordinates of a deformed prostate mesh, contained in vector $\mathbf{x}$, are given by:

$$\mathbf{x} = \mathbf{x}_0 + \bar{\mathbf{d}} + \mathbf{S}^{-1}\left(\sum_{i=1}^{L} b_i \mathbf{p}_i\right), 1 \leq L \ll 3M+1 \tag{3.3}$$

where $\mathbf{x}_0$ contains the node co-ordinates of the reference mesh (derived from the source image) and the reference balloon radius R_0. Figure 3.15 shows the shape of the deformed prostate mesh after varying b_i independently for $1 \leq i \leq 6$.

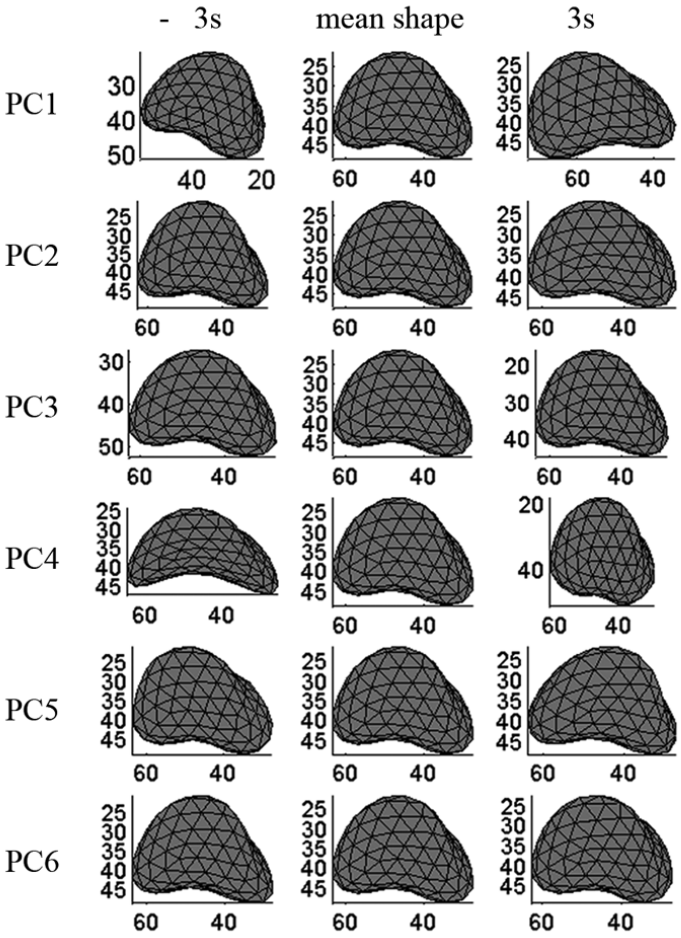

Figure 3.15 Instantiated surface meshes after independently changing the weights corresponding to the first six principal components, PC1 - PC6. The left and right columns show the shapes after changing each weight to +/- 3*s*,

respectively, where *s* is the standard deviation of the weight over the training data. The middle column shows the mean shape for comparison.

When $L < 3M + 1$, a RMS reconstruction error for one training simulation can be defined as:

$$\varepsilon = \sqrt{\frac{1}{(\beta-\alpha+1)}\left(\sum_{i=L+1}^{M} b_i \mathbf{S}^{-1}[\mathbf{p}_i]_{(\alpha,\beta)}\right)^T \left(\sum_{i=L+1}^{M} b_i \mathbf{S}^{-1}[\mathbf{p}_i]_{(\alpha,\beta)}\right)} \quad (3.4)$$

where the notation $[\mathbf{p}_i]_{(\alpha,\beta)}$ denotes the vector formed from the elements α through to β of vector. If $\alpha = 1$ and $\beta = 3M$, evaluating ε gives the RMS error in the gland node displacements, denoted by $\varepsilon_{\text{gland}}$. Similarly, we can define a reconstruction error, ε_R, for the balloon radius, R, by setting $\alpha = \beta = 3M + 1$. For each SMM, L was chosen such that the SMM covered at least 99.5% of variance in the training data and that $\varepsilon_{\text{gland}} <$ 0.2mm and $\varepsilon_{\text{R}} <$ 0.2mm, computed over all training examples.

3.3.1.2 MR-derived Statistical Motion Model

In the case of building an SMM from MR images, i.e. an MR-derived SMM, the reference status would be less useful, as no such correspondent reference is available in target ultrasound images. Therefore, before extracting the principal components (Eq. 2.11), a rigid alignment was applied using Procrustes analysis (Umeyama 1991) to eliminate the variance due to change of pose in the model. In addition, the normal to the surface, at each of the control nodes, may be approximated from the triangulations. This additional information can be updated immediately after a change in shape and provides a useful representation of the shape for the registration algorithm presented in Chapter 4. Figure 3.16 shows the shapes of the deformed prostate mesh, with surface normal vectors computed using the triangulations, after varying b_i independently for $1 \leq i \leq 3$.

Therefore, the resulting MR-derived SMM is mathematically identical to the one described in Section 2.2.2.3. This linear formulation will be revisited in Chapter 4 when it is put in use for a registration algorithm.

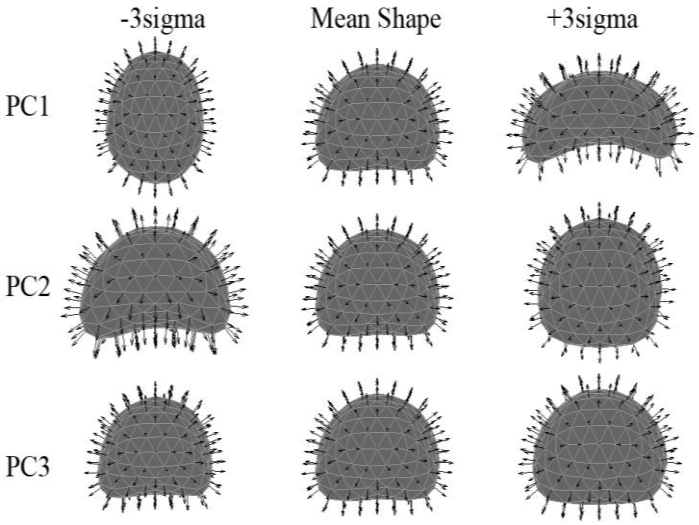

Figure 3.16 Changes in the shape of the first three modes of variation (PC1, PC2 and PC3) of a prostate SMM as a result of independently varying the corresponding weights. The normal vectors at the nodes of the triangulated surfaces, are used in the registration scheme and are indicated by arrows. ('sigma' is the standard deviation for each mode).

3.3.2 The Use of the Statistical Motion Models

The use of conventional SSMs has been summarised in Section 2.2.2.3. There is no fundamental difference between the original formulation and the MR-derived SMM. The difference in building, the synthetic training data and its simplified geometric FE model, would not affect the application of the resulting models. The variance is computed with respect to the mean shape which is computed by averaging the rigid-transformation-excluded node positions. Therefore, in the instantiation of the model, and possibly in later optimisation as well, an extra rigid component should be added to compensate for this.

The TRUS-derived SMM, on the other hand, is built with respect to a reference, the ultrasound probe in this case. The variance learnt and summarised is of the displacements relative to the reference. The shape parameters, therefore, can be directly optimised to represent a plausible instance of the model.

Both of the models are incorporated in registration algorithms which are introduced in Chapter 4, where detailed applications for prostate image fusion are described.

Chapter 4 Model-to-Image Registration Algorithms

4.1 Introduction

Following the discussion in the beginning of Chapter 3, this chapter describes the detailed steps required to implement the image registration algorithms developed in this research.

4.1.1 Summary of Prostate Image Registration Methods

Following the discussion in Section 2.1, one of the underlying assumptions in intensity-based registration method is the existence of a valid intensity relationship between a pair of images. This is not always true, especially between multi-modality data. For instance, ultrasound imaging measures the tissue properties such as differences in acoustic impedance while a T2-weighted MR imaging measures the differences in spin-spin relaxation time of different tissues. Therefore, it is difficult to find a valid similarity measure to correctly describe how well the ultrasound and MR images match. For example, the boundary between the central zone and the peripheral zone of the gland is visible in T2 MR but not in ultrasound. In contrast, a different surgical boundary, between inner gland and outer gland, is visible in ultrasound but not in MR images. In ultrasound and MR transverse slices, these two different boundaries appear similar: as lines separating the gland into upper and lower parts that have similar shapes. Unfortunately, based on the experience, no existing similarity measures could distinguish these boundaries. It is probably that significant yet uncorrelated differences in intensity pattern also exist in other regions. As a result, most similarity measures try to match these two different boundaries together given a general-purpose non-rigid transformation.

It is argued in this thesis that the most reliable and possibly exclusive corresponding features between MR and ultrasound images are the surfaces of the prostate gland. It is clearly visible and extractable in both modalities. Other potential anatomical landmarks, such as the apex and base of the gland, are also valid, although they provide limited localisation information. Furthermore, corresponding point features can also be defined on the surface. The entire internal structure of the gland, however, may not be driven by the intensity information, but could be predicted by well constrained transformations that convey a plausible gland deformation.

Therefore an explicit feature extraction step can inevitably be found in most proposed methods to register prostate MR and TRUS images. The surfaces have been found to be the only valid

features of interest for registration purposes. For instance, an automatic registration technique reported by Wu et al. (Wu et al. 2003) adopts a "marker-to-pixel" approach in which the prostate capsule surface (the "marker"), segmented from one 3D TRUS image, is rigidly registered to another TRUS image of the same patient using a novel similarity measure and a genetic algorithm optimisation scheme that aims to maximise the alignment between TRUS image gradient vectors and the surface normal vectors. Further work by Shao et al. (Shao et al. 2006) investigated methods for registering the pubic arch in MR and TRUS images by comparing the similarity measure proposed by Wu et al. (2003) with alternative measures based on the average intensity across the surface, and on a modified surface intensity measure that takes advantage of the high intensity at the bone surface and anterior shadow artefact that is characteristic in TRUS images of the pubic arch. The latter measure was found to provide the most robust and accurate registrations of the pubic arch. Unfortunately, the registration error for the prostate gland itself is not reported.

More recently, Xu et al. (Xu et al. 2008) describe a method for rigid MR-to-TRUS registration during freehand transrectal biopsy using an end-firing TRUS probe. Using CT imaging to identify needle tip locations, the accuracy of the system in localising the centres for target tumours within a prostate phantom was found to be 2.4 ± 1.2mm. A further evaluation of the registration accuracy based on the overlap between capsule contours drawn on 2D MR and TRUS images selected from 20 patient datasets yielded a 90 ± 7% overlap following registration. However, no data were provided on the accuracy of registering structures within the gland. It is also noteworthy that the system described in this study only compensates for motion *during* a procedure using TRUS-TRUS image registration initialised by electromagnetic tracking. An initial manual registration of the MR and TRUS images at the start of procedure is therefore required. Details of this initial registration step are unfortunately not provided.

A further phantom-based MR-TRUS registration study was carried out by Narayanan et al. (2009). Using a multi-modality prostate phantom with embedded glass beads, which served as fiducial markers, they report a mean fiducial registration error of 3.06 ± 1.14 following non-rigid registration of MR and 3D TRUS images of the phantom. The registration was achieved by a deformable registration of the prostate surface, segmented from both the MR and TRUS images, followed by linear elastic warping of the gland volume using the surface point displacements as boundary conditions.

Singh et al. (Singh et al. 2008) describe a manual method for non-rigidly registering MR and TRUS images, but this requires significant user interaction during a procedure to place control points to align both the surface and structures inside the prostate. The problem of *automatically* registering MR images to TRUS images is challenging because of the intrinsic differences in grey-level intensity characteristics between the two modalities, combined with the presence of artefacts (particularly in the TRUS images). In particular, standard intensity-based approaches, such as those based on maximising mutual information, often perform poorly since a probabilistic relationship between MR and ultrasound voxel intensities usually does not exist. Furthermore, when the transformation model is non-rigid, such approaches are computationally intensive and therefore typically require high-speed, special-purpose computer hardware and an optimised algorithmic implementation to make them practical for interventional applications.

4.1.2 Model-to-image Registration Framework

Early on in this research, it was recognised that the "marker-to-pixel" method, proposed by Wu et al. (Wu et al. 2003), has the most potential to extend to a fully automatic non-rigid registration method, given a well constrained transformation model. The reasons are 1) it uses the reliable surfaces to be aligned where the first one can be extracted in the preoperative image where there is more time available and fewer restrictions on user interactions; 2) the transformation model can be built to represent the transformation between corresponding features, the surfaces and/or its surface normal vectors. This approach is formalised as the 'model-to-image' method presented in this thesis (also discussed in Section 2.4.2).

However, though the surfaces are identified as corresponding features, more detailed point-to-point correspondences remain unknown. The model-to-image registration problem therefore is converted into a feature registration problem, where the features are the surface points and/or surface normal vectors sampled from the gland. There are methods to formulate the feature registration problem as a probabilistic ML problem. An overview of this class of problems is reviewed in Section 2.4.1, where only the point features are considered. This chapter extends this method 1) to incorporate the SMM as a constrained transformation model; 2) to use the additional orientation vectors representing the surface normal.

The detailed correspondence can be optimised with respect to the maximisation of a specifically designed similarity measure. For instance, the RMS of weighted distances between individual model feature and all the image features may be adopted, whereas the weighting of each image

feature can be calculated according to the distance between single image feature and single model feature. The most simplified solution is to use only the closest image feature, i.e. the weightings of others are set zeros.

A general-purpose optimiser may be used to optimise this RMS distance, which is referred as to the *direct optimisation approach* in this thesis. On the other hand, if the similarity measure is defined as the likelihood function of a normalised PDF, the optimisation problem becomes an ML problem. The latter is referred to as the *probabilistic approach* in this thesis and may be solved via classic statistical methods, such as the EM algorithm introduced in Section 2.4.1.2.

The distance between features, either the spatial locations or the surface normal orientations, is first extracted from the model (the surface of the TRUS-derived- or MR-derived SMM), which could be trivial as the model is usually of certain mathematically convenient representation, and extracted from the image, which requires fast and minimal human interaction in order to enable a rapid and efficient intraoperative procedure.

DIRECT OPTIMISATION APPROACH

PROBABILISTIC APPROACH

Feature Extraction	**Spatial Location Only**			**Spatial Location and Orientation**	
Model Feature	Sampled surface point locations			Surface points & surface normal vectors	
Image Feature	Manually defined points	Voxels having high gradient magnitude	Voxels having high sheetness response	Voxels with gradient vectors	Voxels with normal vectors of sheetness

Table 4.1 Summary of the model-to-image registration framework and its implementations

Table 4.1 summarises the framework of registration between a model and an image developed as part of this thesis. In theory, all the combinations, between different model-, image features and different optimisation procedures can be applied using SMMs or any other transformation model. This thesis describes two instances as the items shaded in black and gray in Table 4.1. The first implementation (black background) employs a TRUS-derived SMM using manually picked surface points from another TRUS image and a direct (general purpose) optimisation algorithm to assess the statistical model; the second (gray background) automatically extracts the image vector features from intraoperative TRUS image to align with the MR-derived model in order to solve the MR-to-TRUS image registration problem.

In the proposed probabilistic registration method, the prostate gland surface within the deformable model is fitted automatically and rapidly to a 3D TRUS volume, acquired during a surgical procedure, by minimising a novel vector-based similarity measure so that the best alignment between the surface normals of the model and estimated surface normals, determined from the TRUS volume, is achieved. The surface normals are estimated automatically from the TRUS image using a second-order Gaussian filter configured to enhance locally sheet-like structures (in particular, the prostate capsule surface). The use of the biomechanically-constrained TRUS-derived- or MR-derived SMM enables registration to be achieved rapidly, which is particularly important for time-critical applications such as image-guided prostate cancer interventions. Furthermore, although only the capsule surface is aligned during the registration, the displacement of every voxel within the gland can be calculated as the model captures motion based on the displacement of every node in the FE mesh. This is particularly advantageous because the location of clinically important features, such as tumours, which are usually only visible in MR images, can be predicted within the TRUS volume. It also overcomes the problem of lack of corresponding intra-prostatic features visible in both MR and TRUS images, as discussed above.

A schematic overview of the 'model-to-image' registration approach is shown in Figure 4.1. The model building process (shaded) is described in Chapter 3. The TRUS-derived- and MR-derived SMMs are specific examples of a preoperative model. During the intervention, the following steps are proposed in the registration algorithm (labelled b in Figure 4.1). This occurs during the intraoperative stage, where all computations are required to meet the time, interaction and computation restrictions.

b.i) Acquire a 3D TRUS volume;

b.ii) Compute the TRUS image features;

b.iii) Iteratively optimise the rigid-body and/or SMM shape parameters until the likelihood of a particular set of registration parameters given the feature vectors derived from the TRUS image, or other similarity measure, is maximised.

b.iv) Compute the final displacement for each MR voxel inside the FE model and warp the MR image using these displacements.

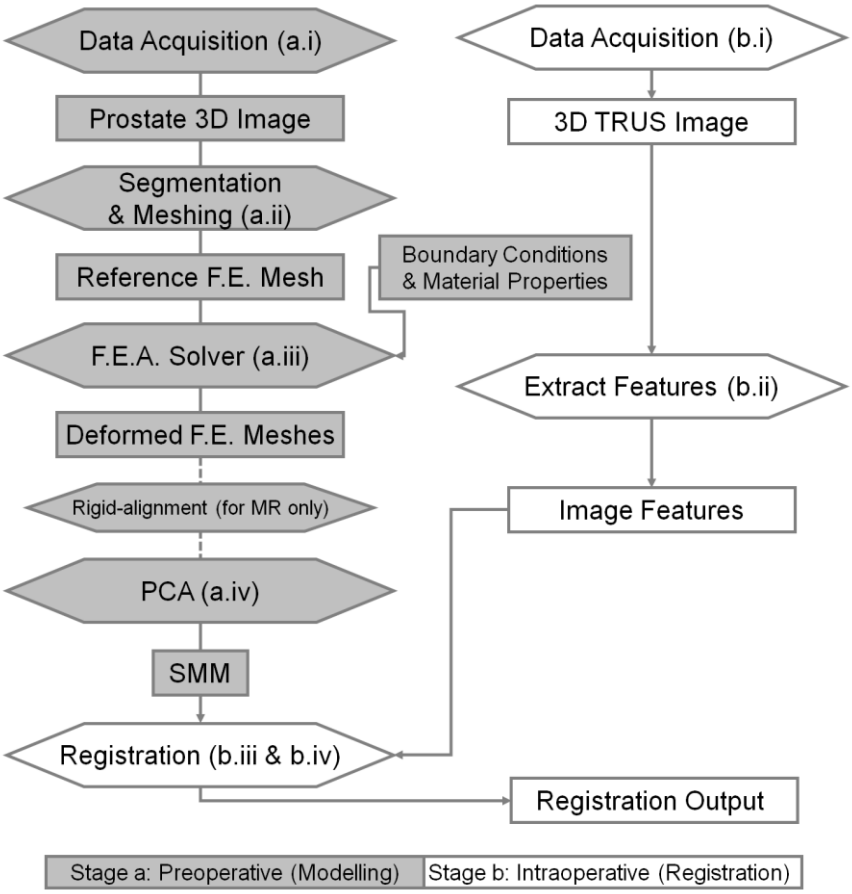

Figure 4.1 A flowchart of the modelling method (shaded) and the registration method (clear)

4.2 Model-to-image Registration Algorithms

4.2.1 Direct Optimisation Approach

The following approach solves the registration problem using a classic optimisation framework, where the transformation, parameterised by registration parameters, is optimised to maximise the similarity measure (i.e. the objective function; see Chapter 2).

In the application of registering prostate images, the different image features extracted from TRUS images are discussed first. Similarity measures, in particular, a class of cosine functions between surface normal vectors are introduced. The use of an SMM as a transformation model (see Chapter 2) is then revisited in order to formalise the optimisation problem.

4.2.1.1 TRUS Image Features

As listed in Table 4.1, three image features are considered in this work: points, image gradient and Hessian-based sheetness. The last two can be represented as either point or directional features depending on whether the orientation information is used.

Manual Point Features

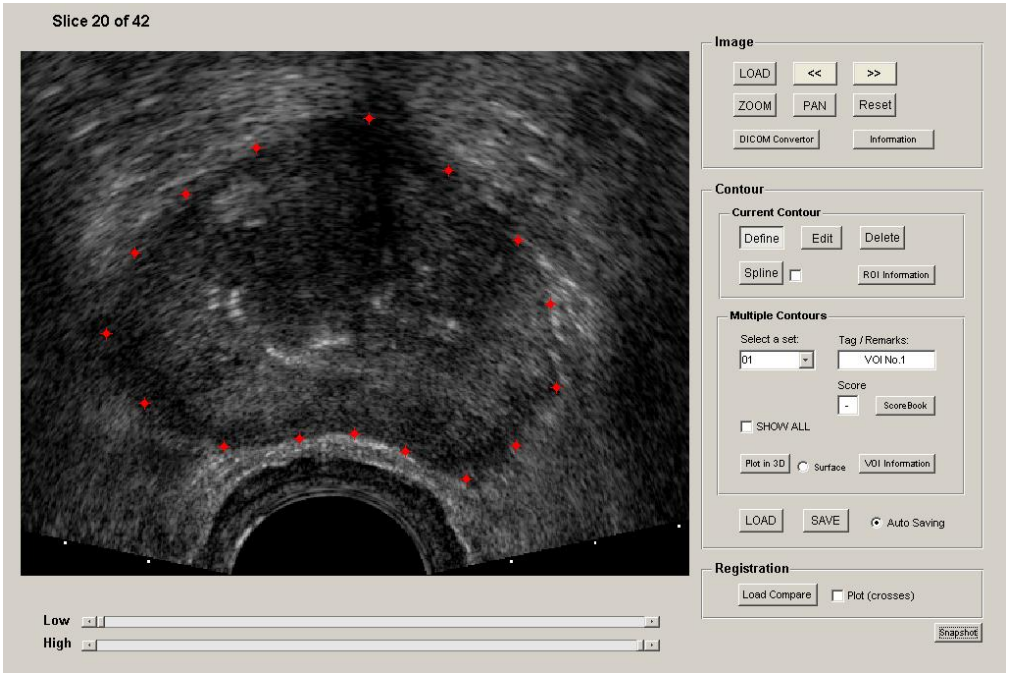

Figure 4.2 A snapshot of the software for defining points on a 2D image slice

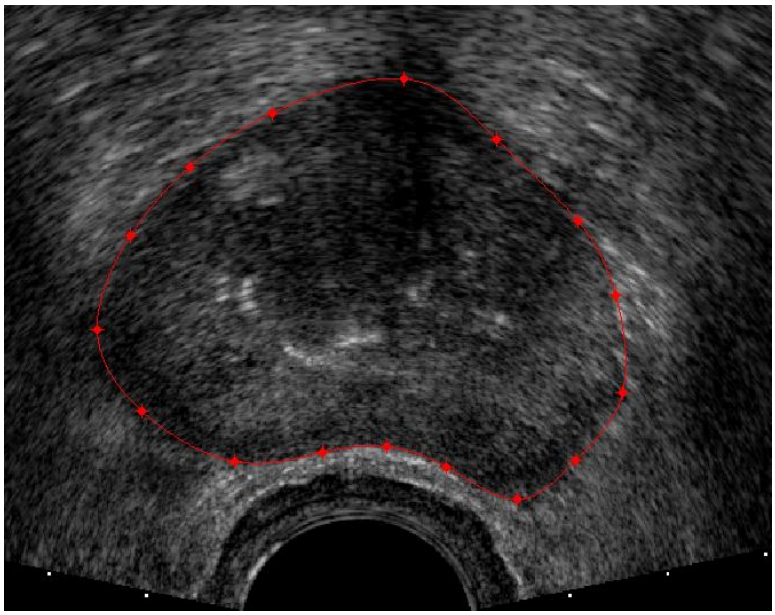

Figure 4.3 An illustration of a spline fitted contour

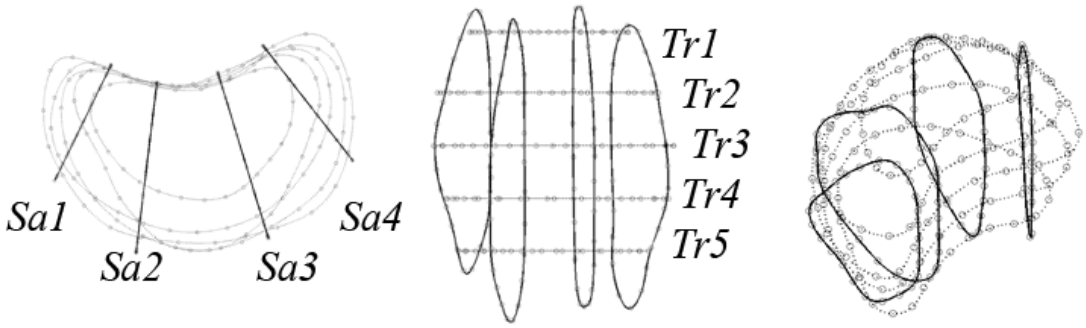

Figure 4.4 Three views of defined contours in four sagittal views (solid contours), five transverse views (dotted contours) and sampled 25 target points (circle-knots) on each contour.

In many circumstances, manually-defined points remain the most accurate and reliable features to identify the prostate capsule in TRUS data. In this case, typically 5-20 points on each 2D slice are identified at the position where the operator believes the surface of the prostate is located. Figure 4.2 illustrates the MATLAB GUI for defining such points. A cubic spline can be fitted to these points to form a closed contour in each slice. Evenly spaced points can then be sampled from the spline as illustrated in Figures 4.3 and 4.4. The re-sampled contour points form a point set that describes the surface.

Image Gradients

One of the most widely adopted image features is image gradients. Computing image gradients quantifies significant intensity change which characterises edge/boundary structures. For instance, the Canny edge detection is a discrete version of such extraction (Canny 1986). An intensity change in an ultrasound image is assumed to be the boundary between two different tissue types. Thresholding then can be applied to the magnitude of the gradients to identify the locations of such boundaries. Instead of the magnitude, it was found that the full derivatives, i.e. a three-dimensional vector, provide a better feature for registration. Gaussian derivatives with respect to a certain scale are used here to derive the image gradient. The Normalised gradient field (NGF) (Haber et al. 2006) was also found to effectively reduce the sensitivity to noise and provide a smooth cost function based on a cosine measure. The NGF is modified as follows to employ the derivative of the Gaussian $G(\mathbf{y}, \sigma^2)$:

$$\mathbf{v}(\mathbf{y}, I, \sigma, \varepsilon) = \nabla I(\mathbf{y}, \sigma) / \sqrt{\nabla I(\mathbf{y}, \sigma)^T \nabla I(\mathbf{y}, \sigma) + \varepsilon^2} \tag{4.1}$$

where $\varepsilon(\eta) = \frac{\eta}{V} \int_{\Omega} |\nabla I(\mathbf{y}, \sigma)| \cdot d\mathbf{y}$, $\nabla I(\mathbf{y}, \sigma) = I(\mathbf{y}) * \nabla G(\mathbf{y}, \sigma^2)$, $I(\mathbf{y})$ is a given image with a 3D co-ordinates vector $\mathbf{y}$, ∇ denotes the gradient of a scalar function, σ^2 is the variance of the

Gaussian, and ε is a small constant governed by an additional parameter η and number of voxels/pixels V in the image domain Ω.

Therefore, a vector representation $\mathbf{v}$ of the possible gland surface in TRUS data can be formed. This is superior to the non-normalised gradient as it conveys pure geometric information which is sometimes more relevant for representing local regions (Haber et al. 2006).

Hessian-based Sheetness Filtering

A surface normal vector field, $\mathbf{v}(\mathbf{y})$, can be defined for the image in a similar form, where $\mathbf{y}$ is a 3D position vector that defines a point in image space. In order to estimate $\mathbf{v}$ in this case, a multi-scale filtering technique based on second-order Gaussian derivatives was employed. In this method, the Hessian matrix is first computed at each voxel for a particular scale of the Gaussian operator. The relative magnitudes of the eigenvalues of the Hessian are then used to classify the local structures, and to enhance blob-, tubular- or sheet-like features in an image (Frangi et al. 1998). In this work, an extension of the sheet-like enhancement filter (Descoteaux et al. 2006) was developed to compensate for the non-uniform ultrasound image intensity characteristics found at the capsule boundaries due to artefacts arising from the variable angle between the true surface normal at the boundary and the ultrasound beam path. In particular, this effect is responsible for visible differences in the low boundary intensity on the lateral sides of the prostate gland compared to those on the inferior and superior sides of the gland.

In the original formulation (Descoteaux et al. 2006), the filter response, f_{sheet}, is given by:

$$f_{sheet}(\mathbf{y}) = \exp\left(-\frac{R_1^2}{2\alpha^2}\right)\left(1-\exp\left(\frac{R_2^2}{2\beta^2}\right)\right)\left(1-\exp\left(\frac{R_3^2}{2\gamma^2}\right)\right) \tag{4.2}$$

where $R_1 = |\lambda_2/\lambda_3|$, $R_2 = \left|2|\lambda_3| - |\lambda_2| - |\lambda_1|\right|$ and $R_3 = \sqrt{\lambda_1^2+\lambda_2^2+\lambda_3^2}$. The eigenvalues of the Hessian, λ_1, λ_2 and λ_3, are computed at point $\mathbf{y}$, ordered according to the magnitude, i.e. $|\lambda_1| \leq |\lambda_2| \leq |\lambda_3|$. For the TRUS volumes acquired for this thesis, the filter response was found to be insensitive to the scalar parameters, α, β and γ, and therefore these were set to the constant values α = β = 0.5 and $\gamma = \max_{\mathbf{y}} R_3$, as suggested by Descoteaux et al. (Descoteaux et al. 2006). For simplicity, f_{sheet} was computed for a single scale. It was found that a value of 1mm for the width σ (in all directions) of the Gaussian operator (used to compute the Hessian) enhances the capsule well in the ultrasound images processed in this work.

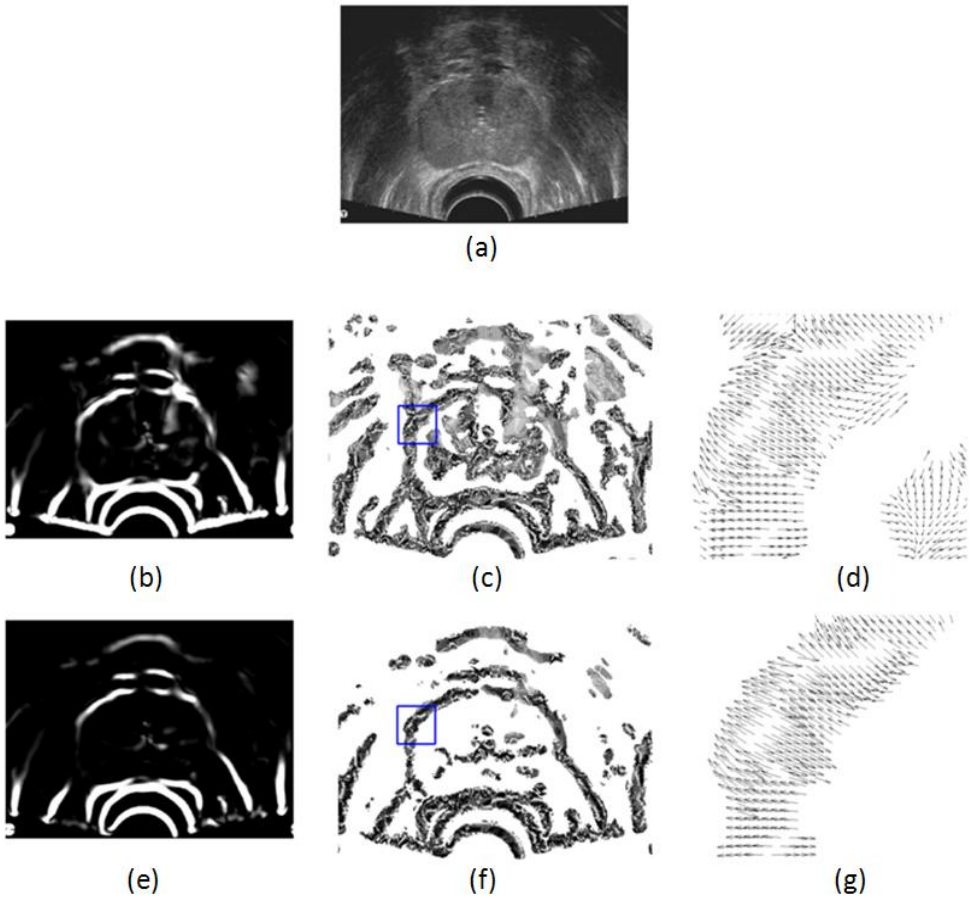

Figure 4.5 Example of the surface normal vector field estimated from a 3D TRUS image. (a) is a transverse slice through the TRUS volume. (b) and (e) show the same slice after applying the filter, f_{sheet} and f^*_{sheet}, defined in Eqs. 4.2 and 4.3, respectively. (c) and (f) shown the vector field, v, extracted using these filters, and (d) and (g) show zoomed-in views of the regions indicated in (c) and (f). From inspection of (f), it can be seen that the TRUS beam compensation integrated in f^*_{sheet} results in a significant reduction of noise compared with (c).

In order to take the direction of the ultrasound beam into account the modified filter is proposed as follows:

$$f^*_{sheet} = (\mathbf{n}_3^T \mathbf{b}_{US})^2 f_{sheet} \tag{4.3}$$

where $\mathbf{b}_{US}$ is the 3D vector that defines the radial direction of TRUS beam and $\mathbf{n}_{3,}$ is the eigenvector corresponding to the largest eigenvalue λ_3 of the Hessian, which is approximately aligned with the surface normal at the capsule boundary. Therefore, when the direction of the ultrasound beam is approximately perpendicular to the surface normal, the sensitivity of the feature vector field to noise is significantly reduced, as illustrated in Figure 4.5.

Considering only filter responses within a predefined window, the final surface normal vector field is given by:

$$\mathbf{v}(\mathbf{y}) = \begin{cases} \mathbf{n}_3(\mathbf{y}) & (a \le f^*_{sheet}(\mathbf{y}) \le b)\&(\lambda_3 > 0) \\ \mathbf{0}, & otherwise \end{cases} \tag{4.4}$$

where the upper and lower limits of the window, within which the filter response is considered to be significant, are specified by scalars a and b, respectively. An example of the vector field $\mathbf{v}$ computed for a TRUS volume is shown in Figure 4.5.

4.2.1.2 Similarity Measures between Spatial and Directional Features

Point Distance

The spatial distance from the model surface to the target point is simplified by the closest point between densely sampled points (from the surface) to the closest target point. The target points can be the manually defined points, voxels having a large magnitude (e.g. of the gradient defined in Eq. 4.1) or voxels having a high sheetness response f^*_{sheet}, defined in Eq. 4.3, depending on the method used to extract the target features. Therefore, the overall similarity measure between two source (model) and target (image data) point sets, $\mathbf{x}_j (j = 1 \dots J)$ and $\mathbf{y}_i (i = 1 \dots I)$, respectively, is given by the RMS of the Euclidean distances:

$$D_{spa} = \begin{cases} \sqrt{\frac{1}{J}\sum_{j=1}^{J}\left\|\mathbf{y}_j^* - \mathbf{x}_j\right\|^2}, if\ J \ll I \\ \sqrt{\frac{1}{I}\sum_{i=1}^{I}\left\|\mathbf{x}_i^* - \mathbf{y}_i\right\|^2}, if\ J \gg I \\ \sqrt{\frac{1}{I+J}\left(\sum_{j=1}^{J}\left\|\mathbf{y}_j^* - \mathbf{x}_j\right\|^2 + \sum_{i=1}^{I}\left\|\mathbf{x}_i^* - \mathbf{y}_i\right\|^2\right)}, if\ J \approx I \end{cases} \tag{4.5}$$

where $\mathbf{y}_j^*$ is the closest point to point $\mathbf{x}_j$ from point set $\mathbf{y}_i$, and $\mathbf{x}_i^*$ is the closest point to $\mathbf{y}_i$ from $\mathbf{x}_j$. This RMS distance reflects the overall similarity measure between two point sets. If the one-to-one correspondence is not known, several methods (as discussed in Section 2.4.1) could be used to minimise the distance, where the closest points are acting as temporarily corresponding points in order to iteratively compute an optimal transformation.

Distance between Orientation Vectors

The "distance" between directional vectors, which quantifies how well aligned they are, may be described using a cosine function. If the 180 degree opposite directions cannot be distinguished, i.e. in the case of bipolar directional data, the square cosine may be used. An extra power parameter *e* is introduced for weighting the alignment. The directional distance, or equivalently, the inverse similarity measure, is therefore defined as:

$$D_{dir} = \frac{1}{J}\sum_{j=1}^{J} d_j \tag{4.6}$$

$$d_j = \begin{cases} \left(\cos^2 \psi_j\right)^e, & e \geq 1 \\ 1 - \left(1 - \cos^2 \psi_j\right)^e, & 0 < e < 1 \end{cases} \tag{4.7}$$

where ψ_j is the angle between the correspondent model and image directional data, $\mathbf{u}_j$ and $\mathbf{v}_j^*$, defined at position j, respectively. The cosine value can be computed using the scalar product between the pair of normalised vectors:

$$\cos \psi_j = \mathbf{u}_j \cdot \mathbf{v}_j^* \tag{4.8}$$

Figure 4.6 compares the proposed metric d_j (defined in Eq. 4.7) with conventional cosine metrics. The modified cosine metric is controlled by the power e. The smaller e, the less sensitive the similarity measure is to strong matches and *vice versa*. This is particularly useful when a certain amount of strong but false positive matches exist in real image data, and their contributions to the overall similarity measure need to be reduced.

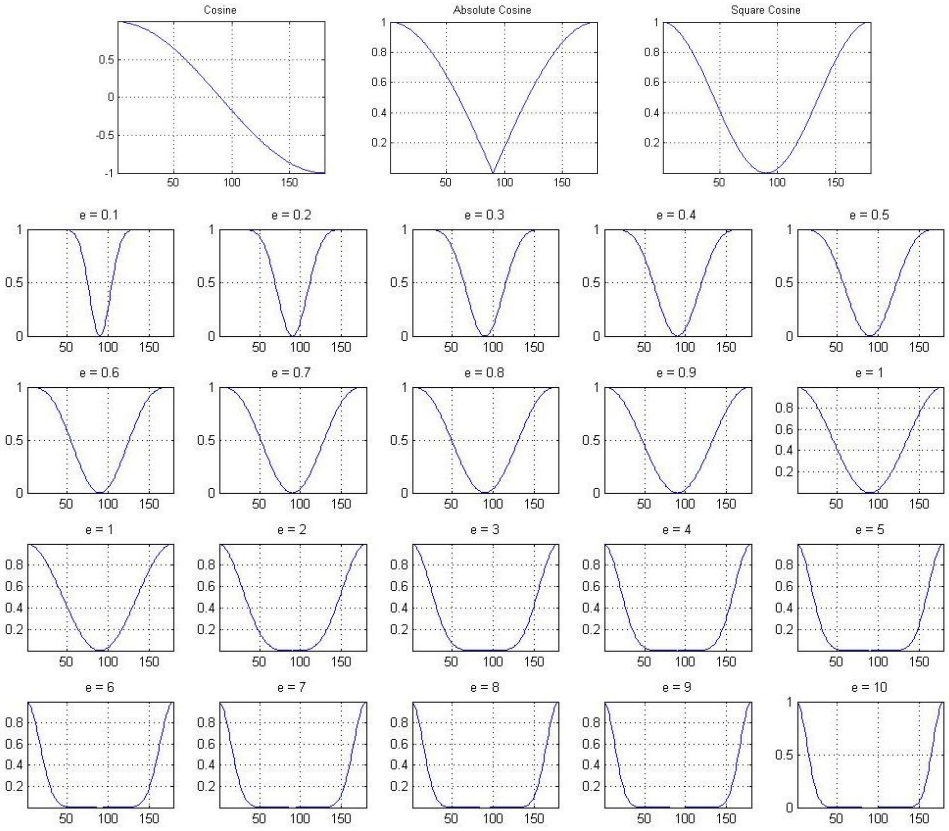

Figure 4.6 In the top row, three plots show the behaviour of cosine function and its variance. The remaining plots show the behaviour of modified cosine function as *e* changes.

However, the correspondence problem remains for the directional similarity measure. The spatially closest point for which the directional data is available may substitute for the true corresponding directional data. Alternatively, an interpolation sampling scheme may be adopted to compute the directional data at position j. This interpolation usually requires spatial information from nearby data, so the spatial data would be effectively considered in the overall directional distance calculation. Therefore, the goal of combining the spatial and directional information can be achieved at the price of a separate, possibly nonlinear interpolation method being necessary. The direct consequence of that would be that the computing of the transformation parameters becomes more complicated. Nevertheless, an iterative numerical optimisation scheme is able to optimise the transformation parameters.

4.2.1.3 Shape Model-based Transformations

Rigid Transformation

First, the rigid or affine transformation, defined in Section 2.2.2.1, may be applied solely to compensate motion when the remaining non-rigid motion is negligible. The rigid transformation used in this thesis of spatial locations is given again by:

$$\tilde{\mathbf{x}}_j = \mathrm{T}_{rigid}\left(\mathbf{x}_j, \boldsymbol{\theta}_{rigid}\right) = s\mathbf{R}\mathbf{x}_j + \mathbf{t} \tag{4.9}$$

where $\mathbf{x}_j$ is the spatial co-ordinate vector of a feature or voxel, $\tilde{\mathbf{x}}_j$ is the transformed co-ordinates. $\boldsymbol{\theta}_{rigid}$ is the transformation parameter vector, i.e. s, $\mathbf{R}$ and $\mathbf{t}$, scaling, rotation matrix and translation vector, respectively. Additionally, the rigid transformation can be directly applied to the rotational vectors as follows:

$$\tilde{\mathbf{u}}_j = \mathrm{T}_{rigid}\left(\mathbf{u}_j, \boldsymbol{\theta}_{rigid}\right) = \mathbf{R}\mathbf{u}_j \tag{4.10}$$

where $\mathbf{u}_j$ and $\tilde{\mathbf{u}}_j$ are the original and rigid-transformed orientation vectors, respectively. The isotropic scaling and the translation are invariant to the directional data.

TRUS-derived SMM Transformation

For the TRUS-derived SMM, the motion can be reconstructed by Eq. 3.3 (defined in Section 3.3.1.1), where the shape parameters are the registration parameters. This transformation (Eq. 3.3) is rewritten as:

$$\tilde{\mathbf{x}} = \mathrm{T}_{SMM}(\mathbf{x}_0, \boldsymbol{\theta}_{SMM}) = \mathbf{x}_0 + \bar{\mathbf{d}} + \mathbf{P}\mathbf{b} \tag{4.11}$$

where the registration parameters $\boldsymbol{\theta}_{SMM}$ represent the weighting vector $\mathbf{b}$, and the original model locations and the mean motion over training data are denoted by $\mathbf{x}_0 = [{\mathbf{x}_1}^T, \dots, {\mathbf{x}_M}^T]_0^T$ and $\bar{\mathbf{d}}$, respectively. $\tilde{\mathbf{x}} = [{\tilde{\mathbf{x}}_1}^T, \dots, {\tilde{\mathbf{x}}_M}^T]^T$ contains the transformed locations so that:

$$\tilde{\mathbf{x}}_j = [\tilde{\mathbf{x}}]_{(3(j-1)+1,3j)} \tag{4.12}$$

The transformed surface normal is also dependent on the spatial locations of the surface, which is represented discretely by a triangulation discussed in Section 3.2.1.2. A valid transformation of sparse directional data has not been developed with respect to a general non-rigid spatial transformation. Therefore, the transformed directional data for the SMM is denoted by:

$$\tilde{\mathbf{u}}_j = \mathrm{T}_{SMM}(\mathbf{u}_j, \tilde{\mathbf{x}}_j) \tag{4.13}$$

In the case of the normal of a triangulated surface, this can be computed using the transformed vector $\tilde{\mathbf{x}}_j$ and updated triangulation.

MR-derived SMM Transformation

On the other hand, the MR-derived SMM has a slightly different form with respect to the rigidly aligned original model. Therefore, $\mathbf{x}_0$ is replaced by the vector-valued rigid transformation function, $[\mathrm{T}_{rigid}(\mathbf{x}_j, \boldsymbol{\theta}_{rigid})]_{j=1,..,M}$:

$$\tilde{\mathbf{x}} = \mathrm{T}_{SMM}([\mathbf{x}_j^T]_{j=1,..,M}^T, \boldsymbol{\theta}_{SMM}) = \left[[\mathrm{T}_{rigid}^T(\mathbf{x}_j, \boldsymbol{\theta}_{rigid})]_{j=1,..,M}\right]^T + \mathbf{Pb} \tag{4.14}$$

where the registration parameters $\boldsymbol{\theta}_{SMM}$ is now constituted by the shape parameters, the weighting vector $\mathbf{b}$, and the rigid transformation parameters $\boldsymbol{\theta}_{rigid}$. Individual transformed locations can again be extracted by Eq. 4.12.

4.2.1.4 Optimisation Scheme

The registration task may now be converted into an optimisation problem, by re-writing the optimisation as:

$$\hat{\boldsymbol{\theta}} = min_{\boldsymbol{\theta}}\, D_{spa}(\{\mathbf{y}_i\}, \mathrm{T}(\{\mathbf{x}_j\}, \boldsymbol{\theta})) \tag{4.15}$$

and

$$\hat{\boldsymbol{\theta}} = min_{\boldsymbol{\theta}}\, D_{dir}(\{\mathbf{v}_i\}, \mathrm{T}(\{\mathbf{u}_j\}, \boldsymbol{\theta})) \tag{4.16}$$

for spatial point features and directional features, respectively. Alternatively, these two distance measures can be combined by a scalar weighting parameter w_{dir}:

$$\widehat{\boldsymbol{\theta}} = min_{\boldsymbol{\theta}}[(1 - w_{dir})D_{spa}\left(\{\mathbf{y}_i\}, \mathrm{T}\left(\{\mathbf{x}_j\}, \boldsymbol{\theta}\right)\right) + w_{dir}D_{dir}\left(\{\mathbf{v}_i\}, \mathrm{T}\left(\{\mathbf{u}_j\}, \boldsymbol{\theta}\right)\right)] \quad (4.17)$$

where T can be any transformation defined in the last section. There are also a number of choices for the optimisers as discussed in Section 2.3.3.

To achieve a robust registration algorithm, a multi-resolution scheme is briefly described as follows:

(1) Initialise the prostate surface model by aligning the apex and base;
(2) Start with scale *s = 2 mm*,
(3) Optimise the objective function based on a modified cosine measure with respect to the rigid transformation parameters;
(4) Optimise the same objective function with respect to the rigid transformation parameters and shape parameters together;
(5) *Set s = s/2* and change the sampling rate accordingly;
(6) If *s > 0.5 mm* (three levels of multi resolution scheme), go back to (3).

Details of the initialisation in Step (1) are described in Section 4.2.3. The scale used in Steps (2), (5) and (6) is related to the standard deviation of Gaussian operator, described in Section 4.2.1.1. Figure 4.7 shows an example of the filtered images with a gradually decreasing scale used in the registration scheme. A rigid-only scheme can be implemented by leaving out the Step (4).

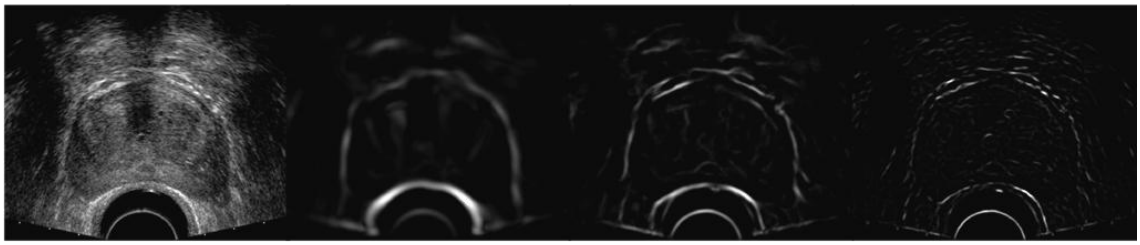

Figure 4.7 Example slices of original image, filtered images with *s=2mm*, *1mm* and *0.5mm*, from left to right, respectively, used in the multi-resolution registration scheme.

4.2.2 A Probabilistic Approach

4.2.2.1 Model-to-Image Noise Model

A framework for modelling image noise is first introduced, with which the model-to-image (or equivalently geometry-to-image) similarity measure can be later formulated. Assuming at a random voxel, i is a signal measured from a given image I; m is a measurement from model M; n is random image noise, the additive relation may be defined symbolically as follows (Boncelet 2005):

$$i = m + n \tag{4.18}$$

$$n = i - m \tag{4.19}$$

$$P_{noise}(n) = P(i - m) \tag{4.20}$$

The *probability of noise* P_{noise}, defined in Eq. 4.20, may be considered as the probability of the "difference" between an *image signal* and a *model*. The noise model also can be considered as a conditional probability of an image given a model:

$$P(i|m) \widehat{=} P(i - m) = P_{noise}(n = i - m) \tag{4.21}$$

Now, assuming *registration parameter* R, a model-to-image registration problem could be formed as:

$$R = arg\max_R[\log L(M, R|I)] = arg\max_R[\log P(I|M, R)] \tag{4.22}$$

Assuming all the voxels (image signals) are independent (Staib et al. 1992;Staib 1996), the following holds:

$$R = arg\max_R[\log \prod_I P(i|M, R)] \tag{4.23}$$

Further, assuming a generative (e.g. mixture[3]) distribution over the model $mixture_M$, with *distribution parameter* θ, leads to:

$$R = arg\max_R[\log \prod_I mixture_M[P(i|m, R, \theta)]] \tag{4.24}$$

[3] *Mixture model is one (possibly the simplest) choice of generative models. More complex model may be considered according to the specific application in hand. This is the type used in this thesis and described in Section 2.4.1.2.*

Then, m is substituted by a (transformed) model m_0, with a specific registration transformation T. Eq. 4.24 becomes:

$$R = arg\max_R[\log\prod_I mixture_M[P(i|m_0 = T(m,R),\theta)]] \quad (4.25)$$

In this formulation, optimising the registration parameters is equivalent to maximising the likelihood of the model given the observed image signals, but could also be interpreted as maximising the joint probability of the image given the model, which is a mixture of the noise models.

Intuitively, the probability of noise describes "how likely it is that this noise occurs". This ought to be maximised in order to find an "optimal" model to best describe the image.

4.2.2.2 The Maximum Likelihood Problem

To ensure that the registration scheme proposed here is robust to noise in the estimated surface normal vector field, $\mathbf{v}$, an approach similar to that described by *Staib and Duncan* (Staib et al. 1992) is adopted, since the model-to-image registration problem is equivalent to the boundary finding problem. In the framework proposed by Staib et al. (Staib et al. 1992), an image-extracted feature, such as the surface normal vector field in the context of this work (described in Section 4.2.1.1), may be considered to be a noise-corrupted version of the corresponding feature determined from a model. Hence, for the present problem, $\mathbf{v}$ may be assumed to be a noise-corrupted version of the surface normal vector field computed for the deformable model $\mathbf{m}$, defined in Section 3.3.1.

Now, the conditional probability that a surface normal vector $\mathbf{v} = \mathbf{v}_i$ is measured at the voxel i with co-ordinates $\mathbf{y} = \mathbf{y}_i = [x_i, y_i, z_i]^T, i \in \Omega_{image}$, given a particular SMM instance, defined by $\mathbf{m}$, can be expressed as a probability mixture model:

$$f_N(\mathbf{y}_i, \mathbf{v}_i|\mathbf{m}) = \sum_{j\in\Omega_{model}} h_j f_G(\mathbf{y}_i|\mathbf{x}_j) f_W(\mathbf{v}_i|\mathbf{u}_j) \quad (4.26)$$

where j is an index to a point in the model space, with co-ordinates $\mathbf{x} = \mathbf{x}_j = [x_j, y_j, z_j]^T, j \in \Omega_{model}$, h_j is a scalar parameter, which satisfies $\sum_j h_j = 1$ and f_G and f_W are probability density functions that describe the multivariate Gaussian and bipolar Watson distributions (Watson 1983), respectively. Explicitly, f_G is defined as:

$$f_G(\mathbf{y}_i|\mathbf{x}_j) = \frac{1}{(2\pi)^{\frac{3}{2}}|\mathbf{\Sigma}_j|^{\frac{1}{2}}} \cdot e^{-\frac{1}{2}(\mathbf{x}_j-\mathbf{y}_i)^T\mathbf{\Sigma}_j^{-1}(\mathbf{x}_j-\mathbf{y}_i)} \quad (4.27)$$

where $\mathbf{x}_j$ is considered as the distribution parameter, mean vector of the multivariate Gaussian, obtained from the model, together with the covariance matrix $\mathbf{\Sigma}_j$, that models the spatial distribution of the data, the co-ordinates of the image features, $\mathbf{y}_i$. In general, the further the feature of the image from the model point, the less likely this image feature was "generated" by the model point. Figure 4.8 shows the surfaces representing certain probability constants with an anisotropic covariance matrix.

Here, a special class of an anisotropic Gaussian with two parameters is used where the covariance matrix, $\mathbf{\Sigma}_j$, is defined by a set of orthogonal vectors $\mathbf{w}_d$ such that

$$\mathbf{\Sigma}_j = \sum_{d=1}^{3} \rho_d \mathbf{w}_d \mathbf{w}_d^T \quad (4.28)$$

where $\mathbf{w}_1 = \mathbf{u}_j$ and $\mathbf{w}_{d=2,3}$, represent the orientations of the ellipsoid surface of constant probability density. The two independent parameters, ρ_1 and $\rho_2 (= \rho_3)$, govern the extent of the capture range of the registration algorithm in the directions normal and tangential to the model surface, respectively. In the experiments described in this thesis, $\rho_1 = 2\rho_{d=2,3}$.

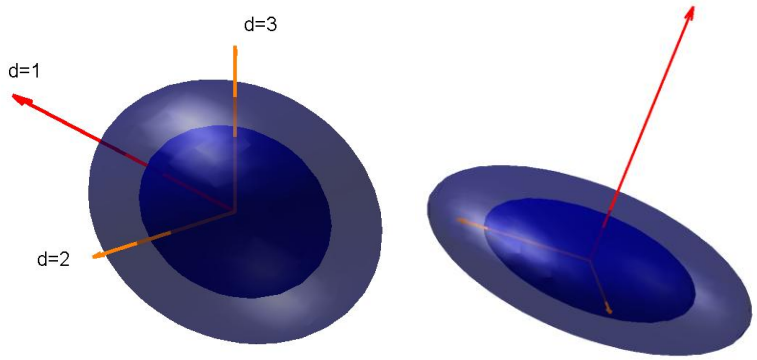

Figure 4.8 Plots of constant surfaces of Gaussian distributions with different values of *d*.

The bipolar Watson distribution f_W is defined as follows:

$$f_W(\mathbf{v}_i|\mathbf{u}_j) = C(k) \cdot e^{k\left(\mathbf{u}_j^T\mathbf{v}_i\right)^2} = C(k) \cdot e^{kcos^2\theta} \quad (4.29)$$

where, k is a scalar concentration parameter. In Figure 4.9, the PDFs are plotted with respect to different values of k, and the colour scaled points with respect to the mean vector (red line

segment) indicate likelihood values of the sampled data. In 3D, the normalising constant, $C(k)$, is defined by setting the integral of f_W over a sphere to unity, leading to:

$$C(k) = \left(2\pi \int_0^1 e^{kt^2} \cdot dt\right)^{-1} \tag{4.30}$$

The concentration parameter k is varied depending on the level of noise in $\mathbf{v}$ and is set to a small value ($0.1 < k < 0.5$) in order to weaken the contribution from strong local matches. In practice, $C(k)$ is computed by recursive integration. The parameter θ is the angle between the surface normal vector $\mathbf{u}_j$, computed at point j on the model surface, and the estimated normal vector $\mathbf{v}_i$, computed at the voxel i in the image.

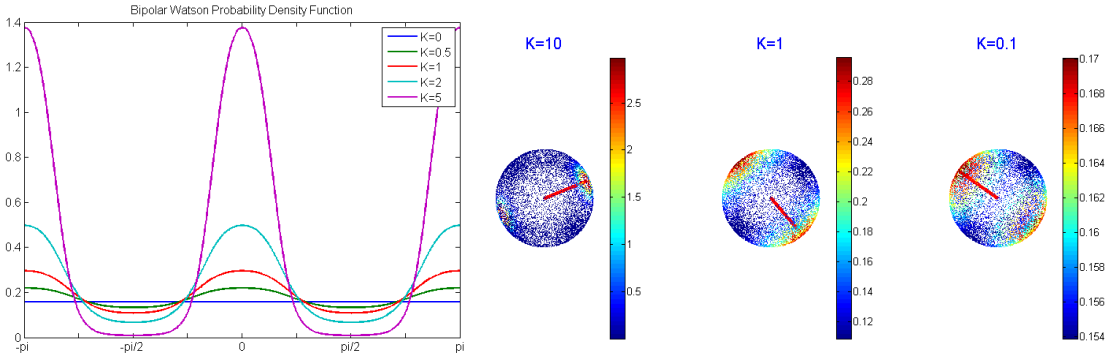

Figure 4.9 Left: plot of PDFs of the bipolar Watson distributions with different values of the parameter *k*. right: the coloured points on a unit sphere to represent the bipolar Watson distribution (colour scale indicates the likelihood of the data).

4.2.2.3 A Probabilistic Objective Function

The purpose of the registration algorithm is to find the optimal registration parameters which maximise the joint probability of the noise function, f_N (in Eq. 4.26), given a particular model shape (specified by the shape parameters of the SMM) and pose (specified by the parameters of a rigid-body transformation). Therefore, assuming that the noise values at different voxels are independent, the following log-likelihood function is a suitable objective function for efficient numerical optimisation using the EM algorithm (Dempster et al. 1977):

$$f_{obj} = \log\big(L(\mathbf{m}|\mathbf{I})\big) = log \prod_{\Omega_{image}} P(\mathbf{I}|\mathbf{m}) = log \prod_{i\in\Omega_{image}} f_N(\mathbf{y}_i, \mathbf{v}_i|\mathbf{m}) =$$
$$\sum_{i\in\Omega_{image}} log \sum_{j\in\Omega_{model}} h_j f_G\big(\mathbf{y}_i|\mathbf{x}_j\big) f_W\big(\mathbf{v}_i|\mathbf{u}_j\big) \tag{4.31}$$

where $\mathbf{I}$ indicates the surface normal features derived from the TRUS volume. A modified version of the standard EM algorithm was implemented using MATLAB, which iteratively

updates the registration parameters in order to maximise Eq. 4.31. Further details are provided in the following sections.

4.2.2.4 An Adapted Expectation Maximisation Algorithm

Rewriting Eq. 4.31, we have the objective log-likelihood function:

$$f_{obj} = \sum_{i=1}^{I} \log \sum_{j=1}^{M} h_j f_G(\mathbf{y}_i \mid \mathbf{x}_j) f_W(\mathbf{v}_i \mid \mathbf{u}_j) \tag{4.32}$$

where I is the number of voxel-based image features and M is the number of sampled points on the deformable surface model.

Therefore, the *E steps* are described as follows:

The posterior probability of the latent variable, also known as membership probability or responsibility, is given by:

$$\gamma_{ij}^{m} = \frac{h_j^m f_G(\mathbf{y}_i \mid \mathbf{x}_j^m) f_W(\mathbf{v}_i \mid \mathbf{u}_j^m)}{\sum_{k=1}^{M} h_k^m f_G(\mathbf{y}_i \mid \mathbf{x}_k^m) f_W(\mathbf{v}_i \mid \mathbf{u}_k^m)} \tag{4.33}$$

where the superscript *m* denotes the estimates in m^{th} step of the EM algorithm (*m = 0* at the start). Now, the expected complete-data log likelihood is:

$$\begin{aligned} Q^m &= \sum_{j=1}^{M}\sum_{i=1}^{I}(\gamma_{ij}^m \cdot \log h_j^m) + \sum_{j=1}^{M}\sum_{i=1}^{I}(\gamma_{ij}^m \cdot \log f_G(\mathbf{y}_i \mid \mathbf{x}_j^m)) + \sum_{j=1}^{M}\sum_{i=1}^{I}(\gamma_{ij}^m \cdot \log f_W(\mathbf{v}_i \mid \mathbf{u}_j^m)) \\ &= \sum_{j=1}^{M}\sum_{i=1}^{I}\{\gamma_{ij}^m \cdot [\log(h_j^m) + \log(\frac{1}{(2\pi)^{3/2}\left|\boldsymbol{\Sigma}_j\right|^{1/2}} \exp(-\frac{1}{2}(\mathbf{y}_i - \mathbf{x}_j^m)^T \boldsymbol{\Sigma}_j^{-1}(\mathbf{y}_i - \mathbf{x}_j^m))) + \log(C(\kappa)\exp(\kappa((\mathbf{u}_j^m)^T \mathbf{v}_i)^2))]\} \end{aligned} \tag{4.34}$$

The *M steps* are described as follows:

M1. Surrogate maximum likelihood estimators (MLEs)

As in the standard EM algorithm for a mixture density model (Bilmes 1997), if we let λ_m denote the Lagrange multiplier due to the constraint $\sum_j h_j = 1$, the updated mixing parameter is calculated by differentiating Eq.4.34 with respect to h_j, setting the resulting derivative to zero, and solving as follows:

$$\frac{\partial Q^m}{\partial h_j} = \frac{\partial}{\partial h_j}\{\sum_{j=1}^{M}\sum_{i=1}^{I}\gamma_{ij}^m \cdot \log h_j\} + \lambda_m(\sum_{j=1}^{M} h_j - 1)) = 0 \tag{4.35}$$

$$\Rightarrow \sum_{i=1}^{I}\frac{1}{h_j}\gamma_{ij}^m + \lambda_m = 0 \tag{4.36}$$

$$\Rightarrow h_j^{m+1} = \frac{1}{I}\sum_{i=1}^{I}\gamma_{ij}^m \tag{4.37}$$

To update the spatial parameters, we perform the procedure:

$$\frac{\partial Q^m}{\partial \mathbf{x}_j} = \frac{\partial}{\partial \mathbf{x}_j}\{\sum_{j=1}^{M}\sum_{i=1}^{I}\{\gamma_{ij}^m \cdot [-\frac{1}{2}(\log|\boldsymbol{\Sigma}_j|) - \frac{1}{2}(\mathbf{y}_i - \mathbf{x}_i)^T \boldsymbol{\Sigma}_j^{-1}(\mathbf{y}_i - \mathbf{x}_i)]\} = 0 \tag{4.38}$$

$$\Rightarrow \sum_{i=1}^{I}\gamma_{ij}^m \cdot \boldsymbol{\Sigma}_j^{-1}(\mathbf{y}_i - \mathbf{x}_j) = 0 \tag{4.39}$$

$$\Rightarrow \hat{\mathbf{x}}_j = \sum_{i=1}^{I}\gamma_{ij}^m \cdot \mathbf{y}_i \Big/ \sum_{i=1}^{I}\gamma_{ij}^m \tag{4.40}$$

To estimate directional parameters subject to the constraint $\mathbf{u}_j^T\mathbf{u}_j - 1$, if we let λ_w denote the Lagrange multiplier due to the normalised vector constraint, we have:

$$\frac{\partial Q^m}{\partial \mathbf{u}_j} = \frac{\partial}{\partial \mathbf{u}_j}\{\sum_{j=1}^{M}\sum_{i=1}^{I}\gamma_{ij}^m \cdot [\log(C(\kappa)) + \kappa(\mathbf{u}_j^T\mathbf{v}_i)^2] - \lambda_w(\mathbf{u}_j^T\mathbf{u}_j - 1)\} = 0 \tag{4.41}$$

$$\Rightarrow \sum_{i=1}^{I}\gamma_{ij}^m \cdot (2\kappa \cdot \mathbf{v}_i\mathbf{v}_i^T\mathbf{u}_j) - 2\lambda_w\mathbf{u}_j = 0 \tag{4.42}$$

Now, pre-multiplying by $\mathbf{u}_j^T$ gives:

$$\lambda_w = \kappa\sum_{i=1}^{I}\gamma_{ij}^m \cdot (\mathbf{u}_j^T\mathbf{v}_i\mathbf{v}_i^T\mathbf{u}_j) = 0 \tag{4.43}$$

It is shown by Figueiredo et al. (Figueiredo et al. 2006) that the MLE $\hat{\mathbf{u}}_j$ is the eigenvector associated with the largest eigenvalue of $\sum_{i=1}^{I} \gamma_{ij}^{m} \cdot \mathbf{v}_i \mathbf{v}_i^T$, such that

$$(\sum_{i=1}^{I} \gamma_{ij}^{m} \cdot \mathbf{v}_i \mathbf{v}_i^T)\hat{\mathbf{u}}_j = \hat{w}_j \hat{\mathbf{u}}_j \tag{4.44}$$

M2. Registration parameters

After the mixing, spatial and directional MLEs are updated. The registration parameters can be updated using a weighted least-squares scheme, as follows:

$$\hat{\boldsymbol{\theta}}_{rigid} = \arg\min_{\boldsymbol{\theta}_{rigid}} \sum_{j=1}^{M} h_j^{m+1} (\pi^{-1} \left\| \hat{\mathbf{x}}_j - \mathrm{T}_{rigid}(\mathbf{x}_j^0, \boldsymbol{\theta}_{rigid}) \right\|^2 + k \left\| \hat{\mathbf{u}}_j - \mathrm{T}_{rigid}(\mathbf{u}_j^0, \boldsymbol{\theta}_{rigid}) \right\|^2) \tag{4.45}$$

where T_{rigid} is a rigid-body transformation applied to the spatial and directional vectors given the parameter vector, $\boldsymbol{\theta}_{rigid}$, which contains rotation and translation (note that the directional vectors are invariant to translation). Variable π is the smaller eigenvalue of the covariance matrix so that the lower bound of the anisotropic Gaussian was used to enable a simple Procrustes analysis. The rigid-body parameters were therefore computed based on singular value decomposition (Myronenko et al. 2010;Umeyama 1991).

The shape parameters were updated using weighted least-squares (Luo et al. 2003). In this scheme, only the weighted sum of the squares of the residuals between rigid transformed locations and spatial MLEs were minimised:

$$\hat{\boldsymbol{\theta}}_{shape} = \arg\min_{\boldsymbol{\theta}_{shape}} \sum_{j=1}^{M} h_j^{m+1} \left\| \hat{\mathbf{x}}_j - \mathrm{T}_{shape}(\mathrm{T}_{rigid}(\mathbf{x}_j^0, \hat{\boldsymbol{\theta}}_{rigid}), \boldsymbol{\theta}_{shape}) \right\|^2 \tag{4.46}$$

where T_{shape} applies a shape transformation of spatial locations, given the shape parameters $\boldsymbol{\theta}_{shape}$ according to Section 4.2.1.3. It is assumed that the contribution of the shape transformation to the log-likelihood function with respect to vector reorientation is negligible in this step. Finally, we update $\mathbf{x}_j$ by $\mathbf{x}_j^{m+1} = \mathrm{T}_{shape}(\mathrm{T}_{rigid}(\mathbf{x}_j^0, \hat{\boldsymbol{\theta}}_{rigid}), \hat{\boldsymbol{\theta}}_{shape})$ and re-compute $\mathbf{u}_j^{m+1}$ using the updated $\mathbf{x}_j^{m+1}$ and the model surface triangulations.

Although a closed-form solution to find the registration parameters in the M steps may be possible, a numerical iterative scheme is a practical method for maximising the objective function. A similar approach was described by Ziyan et al. (Ziyan et al. 2008). However, a two step update, which employs an efficient least-squares method, was developed in this thesis. In practice, it was found that the updated parameters increased the value of the log-likelihood function before the registration stopping criterion, either by reaching a maximum number of iterations or a minimal change in the objective function. It should be noted that, in general, this approximation enables a fast implementation without guaranteeing convergence. Alternatively, an additional numerical optimiser could be executed after these updates in each M step to minimise the actual log-likelihood directly.

The user-defined parameters in the registration scheme are the filter parameters a and b, and the similarity measure parameters ρ_1 and k. Values for a and b were found by assessing the histogram of the filter responses on a case by case basis and manually setting the thresholds such that outlier features in the filtered image with low and high intensities were eliminated. These parameters were tuned for each of the TRUS scanners used in this work and remained fixed in the registration experiments. Excluding 10-30% of the lowest and highest intensities was found to produce visually optimal filtered images in which the gland surface was enhanced clearly.

Parameters k and ρ_1 were set to 0.1 and 3mm, respectively. The result of the registration algorithm was found to be insensitive to k for $0.1 < k < 0.5$ and setting $k \ll 1$ was found to significantly reduce the influence of strong boundaries of the bladder, rectum and pubic arch (sometimes visible in the TRUS images) by weighting the similarity measure in favour of surface normal vectors that are not perfectly aligned. Similarly, the algorithm is relatively insensitive to the value of ρ_1. This parameter determines the local search range for the algorithm, and was set to the average distance between surface node points.

4.2.3 Initialisation

Initialisation is important for image registration tasks. In particular, a multi-modal registration application, where two images have different co-ordinate systems, different orientations or scales representing an object of interest, requires initialisation to compensate for large translation, rotation and difference in positioning. Most registration algorithms find an optimal

solution near the initial search position, without the guarantee of finding a global minimum or maximum. Therefore, a separate initialisation stage is crucial for most cases.

In the case of the prostate gland, two anatomical landmarks, apex and base, are generally available in both TRUS and MR images. However, given two pairs of correspondent points, it is not sufficient to approximate a rigid transformation. Therefore, the constraint that no rotation is permitted about the axis defined by these two points is required to enable the transformation calculated by aligning these two axes together. Note that, in this case, a general solution (e.g. Procrustes analysis) is under-determined so it could produce an arbitrary rotation about the axis depending on the adopted algorithm. However, a direct transformation can be calculated as follows: 1) first compute the displacement vector by aligning the centres of the line segments bounded by apex and base; 2) compute angle differences in x-y, x-z and y-z planes; 3) find the rotation matrix using any two of these angles such that neither is zero; 4) depending on the problem, compute the scaling factor along the aligned axis. An example using this initialisation is shown in Figure 4.10. This is the method used for all the experiments reported in this thesis although other methods exist that provide equivalent initialisation, such as the use of bounding boxes and/or manual alignment.

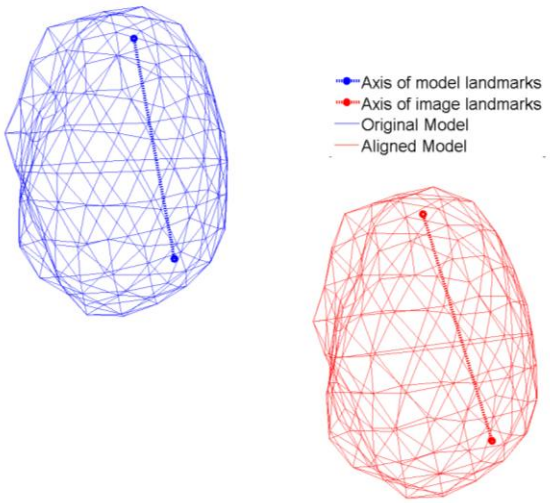

Figure 4.10 Illustration of aligned surface models using a two point initialisation.

Chapter 5 Validation Methods

Validation methodology plays a significant role in any medical image registration study. Assessing a registration method is difficult largely because the corresponding features should be independently selected to compute the validation error metric; the error computed on the features being used in the registration only reflects the performance of the optimisation algorithms. Some authors (Maintz et al. 1998) pointed out that the validation feature may be included in the registration if it is easy to obtain.

In this chapter, sensitivity analysis of material properties and an SMM comparison method is described in Section 5.1 and Section 5.2, respectively. These validations help to assess the motion models described in Chapter 3. The point-feature-based registration and the probabilistic registration approach have been applied to TRUS-to-TRUS and MR-to-TRUS registration tasks, respectively. The details of these experiments will be described in Chapter 6. The methods used to assess the accuracy, robustness and other aspects of the registration algorithms performance are described in Sections 5.3 and 5.4. In particular, an error analysis based on the quantitative relationship between target registration error (TRE) and clinical significance is developed in Section 5.4.2.

5.1 Sensitivity Analysis in Tissue Material Properties

To investigate the effect of errors in tissue parameters on the predicted gland motion using FE model, a sensitivity analysis was carried out in which, for each of the 5 patient datasets, 100 simulations were performed using varying values of the shear and bulk moduli (denoted by *G* and *K*, respectively) under identical boundary conditions. Three sets of simulations were performed using identical boundary conditions as follows:

Test 1: Both *G* and *K* were sampled from the ranges given in Table 3.1;

Test 2: Materials were assumed to be almost incompressible (K>>G);

Test 3: The materials were assigned with one fixed degree of freedom in material parameters (i.e. the "equivalent" Young's moduli, given by *9KG / (3K+G)*, were held constant throughout the simulations).

The difference between Test 1 and 2 and between Test 1 and 3 were compared directly by computing the relative displacements for each node. Tests 2 and 3 correspond to the assumptions applied commonly when predicting tissue displacements using FEA. This is a direct way to compute the difference between different configurations (material properties in this case) of the same FE model. The difference could reveal the significance of the sensitivity of the material property values to the simulated deformation.

5.2 Comparison for the Simplified Motion Models

The SMMs built using a simplified geometry (described in Section 3.2.5) are used in this section to introduce the comparison between different SMMs. The simplified models may be assessed without going through the whole registration process. A valid comparison should determine how much difference exists between the originally proposed SMM and the SMMs based on simplified geometric information. This section provides a framework to compare between different SMMs. The methodology may be extended to any other comparison between shape models.

5.2.1 Statistical Model Fitting

As explained in Sections 3.3.1 and 4.2.1.3, the SMM has the role of constraining the registration transformation that relates the SMM and the deformed prostate, represented by new image data (TRUS images in this case). The shape vector $\mathbf{b}$ can be thought of as containing the parameters of the SMM that are optimised to fit to the new data. In practice, these data can take a variety of forms, but in this case, a (surface) point representation was adopted, which can be derived from any other geometrical representation (for instance, by sampling from a surface).

The ability of different SMMs to fit to new observed data described by the displacement vector $\hat{\mathbf{d}}$ (which takes the same form as $\bar{\mathbf{d}}$) was evaluated. In practice, however, tissue displacements are only measurable at a limited number of locations. For example, in medical images, the surface of a deformed organ is usually available whereas the entire volumetric displacement field over the field-of-view is not. The model fitting process can be posed as finding the vector $\hat{\mathbf{b}}$ which minimizes a fitness (objective) function that quantifies how well the SMM fits the target data represented by the node co-ordinate vector, $\hat{\mathbf{x}}_{\text{target}}$. Three different forms of $\hat{\mathbf{x}}_{\text{target}}$ were considered, each of which requires a different method for finding $\hat{\mathbf{b}}$. The three different scenarios are considered in the following subsections.

5.2.1.1 Known Correspondence on Solid Nodes

In a simplest case, $\hat{\mathbf{x}}_{\text{target}}$ takes the same form as the training data, i.e. a vector containing of co-ordinates of all the FE mesh nodes within the prostate gland. Fitting the SMM – equivalent to solving for $\mathbf{b}$ in Eq. 4.11 – then becomes a linear least squares problem with the following solution:

$$\hat{\mathbf{b}} = (\mathbf{P}^T\mathbf{P})^{-1}\mathbf{P}^T\left(\hat{\mathbf{x}}_{\text{target}} - \mathbf{x}_0 - \bar{\mathbf{d}}\right) = \mathbf{P}^T\left(\hat{\mathbf{d}}_{\text{target}} - \bar{\mathbf{d}}\right) \tag{5.1}$$

where $\hat{\mathbf{d}}_{\text{target}} = \hat{\mathbf{x}}_{\text{target}} - \mathbf{x}_0$ is a vector that represents the displacements of the target data relative to the reference model.

5.2.1.2 Known Correspondence on Surface Nodes

In the present application, the very different appearance of MR and TRUS images results in a lack of common features being present within the prostate. This means that establishing the relative displacements of corresponding voxels across the gland is very challenging. However, it is possible to measure the location of the gland surface (capsule). For this reason, we also consider the second case where the observed data comprises only surface nodes, denoted by $(\hat{\mathbf{x}}_{\text{target}})_S$. The length of the vector $(\hat{\mathbf{x}}_{\text{target}})_S$ is $3S$, where S is the number of surface nodes. In this case, $\hat{\mathbf{b}}$ can still be found via a linear least squares solution if $S > L$. When this condition is satisfied, the parameter vector of the fitted SMM is given by:

$$\hat{\mathbf{b}} = \mathbf{P}_S^T\left((\hat{\mathbf{d}}_{\text{target}})_S - (\bar{\mathbf{d}})_S\right) \tag{5.2}$$

where the matrix $\mathbf{P}$ in Eq. 5.1 is replaced by the $3S \times L$ matrix $\mathbf{P}_s$ and the vectors $\hat{\mathbf{d}}_{\text{target}}$ and $\bar{\mathbf{d}}$ are replaced by the measured and mean surface displacement vectors, $(\hat{\mathbf{d}}_{\text{target}})_S$ and $(\bar{\mathbf{d}})_S$, respectively.

5.2.1.3 Unknown Correspondence

In the more general case where the correspondence between points on the SMM and target surfaces is unknown, the problem of finding $\hat{\mathbf{b}}$ can be posed as a non-linear numerical optimisation problem in which the Euclidean distance between the SMM and observed surface points are minimised, i.e.

$$\hat{\mathbf{b}} = \arg\min_{\mathrm{b}}\left\|\mathrm{D}(\mathbf{b}, (\hat{\mathbf{x}}_{\text{target}})_S)\right\| \tag{5.3}$$

where D is a vector-valued function that returns the distances between the surface of the prostate in the instantiation of the SMM, given the parameter vector $\mathbf{b}$, and the corresponding target surface points.

In this work, a MATLAB implementation of the standard Levenberg-Marquardt algorithm was used to solve Eq. 5.3. D was computed by calculating the distance between the each target node point and the nearest point in a densely sampled point set that represents the SMM prostate surface. To avoid over-fitting of the model to target data, resulting in highly implausible deformations, $\mathbf{b}$ was constrained during the optimisation so that $-3\sqrt{\lambda_i} \leq b_i \leq 3\sqrt{\lambda_i}$. This ensured that the values of the weights in $\mathbf{b}$ lie within three standard deviations ($\sqrt{\lambda_i}$) of the mean value determined by the training data. Imposing this constraint was found to be especially useful when the target data is subject to noise or contains outliers.

5.2.2 Performance Measures

Three different quantitative performance measures, described below, were computed for the SMMs. These were used as a basis for comparison between different SMMs.

5.2.2.1 Model Compactness

An important aspect of PCA-based SMMs is dimensionality reduction. The performance of this property may be represented by model compactness, the relative cumulative variance described by an SMM, defined as:

$$C(L) = \frac{\sum_{i=1}^{L \leq M} \lambda_i}{\sum_{j=1}^{M} \lambda_j} \tag{5.4}$$

where λ_i is the i^{th} eigenvalue of the covariance matrix of the training data, M is the number of all the nonzero eigenvalues.

5.2.2.2 Generalisation Ability

The generalisation ability of a model measures its ability to describe unseen data (Styner et al. 2003). This is arguably the most important performance measure since it relates closely to the most common intended application of SMMs, i.e. capturing organ motion to provide prior information for registering to unseen data. The generalisation ability can be defined as the average error between a statistical shape model and unseen data (Styner et al. 2003). A similar measure has also been derived in shape feature space (Jeong et al. 2008).

Here, a measure is defined as the RMS Euclidean distance between the node positions within the prostate gland of an instantiated SMM and the corresponding node positions of a ground truth deformed model. For the purposes of this work, the fully-specified FE model (SMM1 with MP1 and BC1 described in Section 3.2.5) was used to provide the ground truth tissue motion, assuming that this closely approximates the real tissue motion. When the RMS distance is computed on all nodes inside and on the surface of the prostate gland, this measure becomes analogous to the TRE, which is a widely adopted measure for evaluating the accuracy of image registration algorithms (Fitzpatrick et al. 1998).

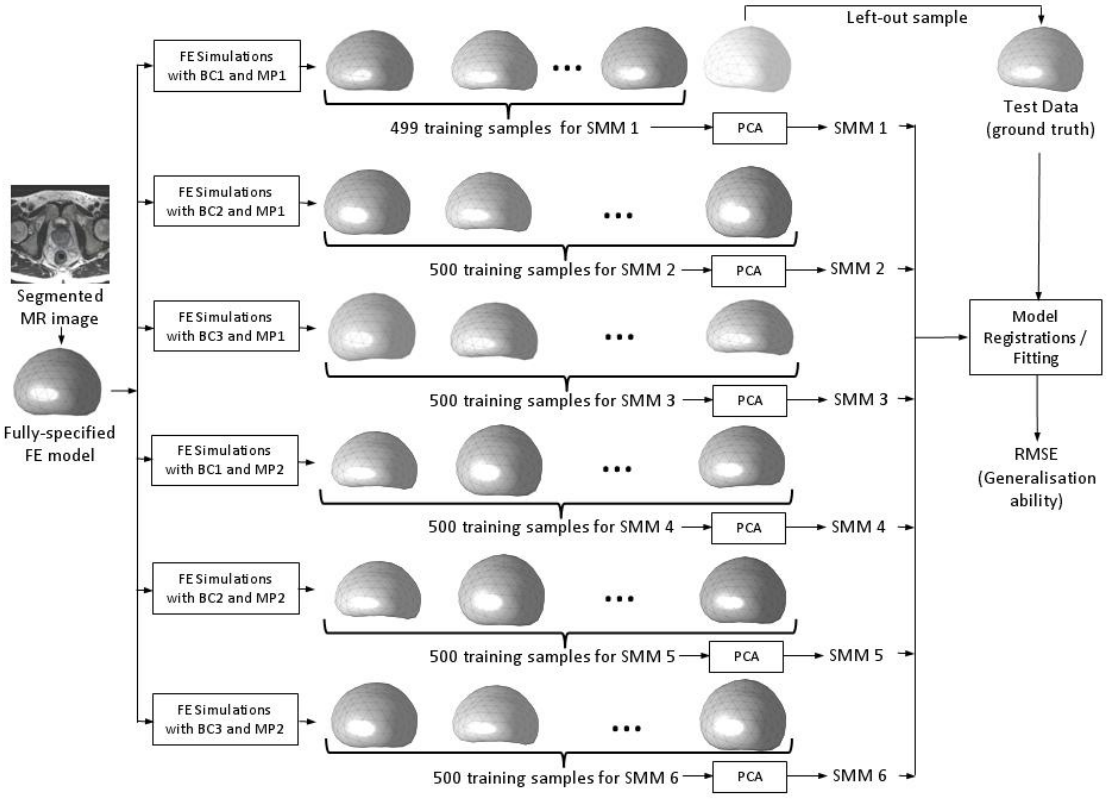

Figure 5.1 An overview of the leave-one-out method used to compare different SMMs by computing the generalisation ability with respect to a reference FE model as the ground truth.

The following "leave-one-out" scheme, illustrated in Figure 5.1, was adopted to avoid bias in the generalisation ability: Firstly, one of the 500 training samples was selected at random. The SMM was then built using the remaining 499 samples to generate the ground truth dataset, based on a FE simulation using the most geometrically accurate mesh (i.e. SMM 1) for that particular patient. In this way, the 6 SMMs could be compared directly in terms of RMS distance error.

In addition, for each of 6 patients, a clinician identified a region of interest (ROI) on the MR images in which biopsy-verified cancer was present. The absolute distance errors of these tumour ROIs were also computed using the same leave-one-out scheme as described above.

5.2.2.3 Specificity

Model specificity is another useful measure, which indicates the degree to which deformations of an SMM are constrained. This is significant because it is desirable for the model to be robust to corrupted data, for instance due to image artefacts or noise. Furthermore, the model should be able to predict missing data.

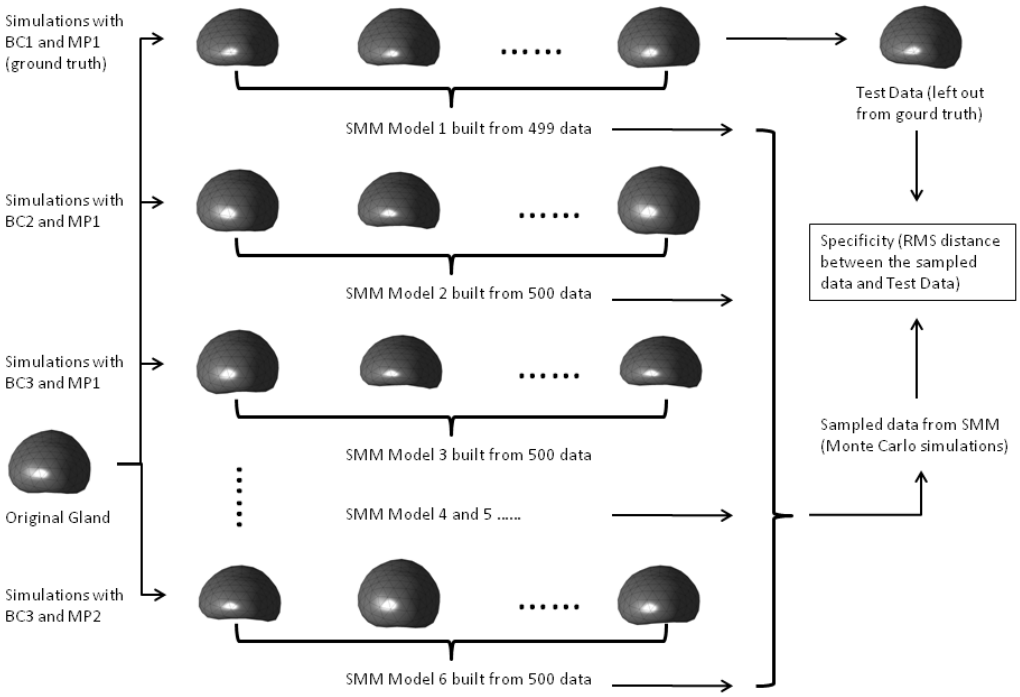

Figure 5.2 An overview of the leave-one-out methodology used to compare different SMMs by computing the specificity ability with respect to a deformed FE model as the ground truth. This figure complements with the Figure 5.1 to describe the Leave-one-out schemes to compute generalisation ability and specificity.

The framework, proposed by Styner et al. (2003) to quantify model specificity using Monte Carlo simulations, was adopted. Figure 5.2 show a schematic overview that describes the method used to compute SMM specificity. For each SMM, 500 instances were generated by setting each parameter b_i to a randomly selected value drawn from a zero-mean normal distribution with standard deviation λ_i. The model specificity was computed as follows: First, for each instantiated SMM, the RMS distance between the nodes of this model and the corresponding nodes of each of the simulated FE meshes in the training dataset was computed. The specificity

was then defined as the smallest RMS distance, which may be interpreted as a measure of how closely the SMM approximates the geometrically closest sample in the training dataset. The absolute distances for the tumour ROIs were also computed as an error measure for specificities.

5.3 Validation of TRUS-TRUS Registration

5.3.1 Accuracy Validation

To assess the effects of setting different degrees of freedom of motion on registration accuracy, three different TRUS-derived SMMs, denoted SMM1, SMM2 and SMM3, were constructed by varying the boundary conditions (summarised in Table 3.1) for each FE simulation: For SMM1, only the radius of the balloon, *R*, was varied between simulations (the pose of probe and pelvic model were fixed to their reference states). For SMM2, *R* and the position and orientation balloon/probe were varied between simulations (the size and position of the pelvis remained fixed). Hence, compared with SMM1, the training data for this model takes into account variation in the pose of the TRUS probe/balloon. Finally, in the simulations for SMM3, the pose and size of the CT-based pelvis model were varied in addition to the radius and pose of the TRUS balloon/probe.

5.3.1.1 Surface Alignment

Surface to point distance is a measure to assess registration accuracy. The alternative may be any other measurement to compute the volumetric overlap between registered ROIs. These are important accuracy measures for segmentation tasks. This type of measure also indicates the optimisation performance of the registration if it is based on surface alignment followed by prediction of the displacement field inside the surface, which is a common strategy in multi-modality image registration, as discussed in Chapter 2. The surface alignment, however, does not reflect the overall accuracy of the registration, in which the primary goal is to predict a location of interest. Therefore the TRE is still required to assess the clinical usefulness of the registration algorithm and it is analogous to the relationship between fiducial localisation error (FLE) (Fitzpatrick et al. 1998) and TRE. Nevertheless, comparison between surface alignment and final TRE reveals the relationship between the optimisation performance and the validation of the methodological assumptions such as similarity measures and transformation models.

The surface-to-surface distance may be simplified to a point-to-point distance, where the distance is approximated by the closest distance between densely sampled points on one or

both surfaces. This is similar to the distance metric used for point registration discussed in Section 4.2.1.2.

To test the robustness of the registration algorithm used (described in Section 5.2.1.3) against different manually defined surface points and to simulate a clinically practical protocol for defining a sparse set of target points during a TRUS-guided procedure, each target TRUS volume was re-sliced in 4 sagittal and 5 transverse planes corresponding to different TRUS views that would be obtainable by rotating or translating a bi-planar, side-firing, TRUS probe. Such probes are widely used for guiding urological procedures involving the prostate and surrounding organs. Then, 6-10 surface points were defined manually in each slice using the MATLAB GUI described in Section 3.2.1. A closed cubic spline was fitted to these points and 25 evenly spaced points are sampled from each contour (see Figure 4.4).

Point set	**Number of views used**		**Number of target points used**
	Transverse Views	**Sagittal Views**	
PS1	Tr1 Tr2 Tr3 Tr4 Tr5	Sa1 Sa2 Sa3 Sa4	225
PS2	Tr1 Tr2 Tr3 Tr4 Tr5	Sa2 Sa3	175
PS3	Tr2 Tr4	Sa2 Sa3	100
PS4	Tr3	--	25

Table 5.1 Combinations of TRUS views used for defining target points

To evaluate the comparative accuracy of assuming no gland deformation, surfaces were additionally registered rigidly to the target point set using the well-known ICP algorithm, described in Section 2.4.1.3. To assess the robustness of the registration, given point data from a decreasing number of TRUS views (contours), all of the registrations were repeated using the 4 subsets of the original 9 views specified in Table 5.1.

5.3.1.2 Landmark-based Target Registration Error

In contrast to MR-to-TRUS registration, where corresponding intraprostatic landmarks, visible in both imaging modalities, are relatively difficult to find, one advantage of using TRUS images as both the target and surrogate source images is that the displacement of many landmarks inside the gland can be measured. In this thesis, landmarks were defined as small, discrete echolucent or echogenic features, which correspond to small cysts and calcifications. For each patient, the 3D co-ordinates of corresponding point landmarks were identified manually in the source and target TRUS volumes using the MATLAB GUI, which enabled the centre of each landmark to be located in three orthogonal views, as shown in the example in Figure 5.3.

The landmarks defined in the source image were then propagated into the target image space using the displacement field produced by the SMM following surface-based registration. The new landmark 3D co-ordinates were calculated by interpolating the displaced mesh node point positions using tetrahedral shape function (Zienkiewicz et al. 2000). In practice, if the tetrahedral mesh is adequately dense, other (potentially faster) interpolation methods would make little difference in accuracy. The target point-to-surface error and the TRE, defined as the RMS Euclidean distance between manually defined and propagated landmark pair in the target image space, were calculated for each registration.

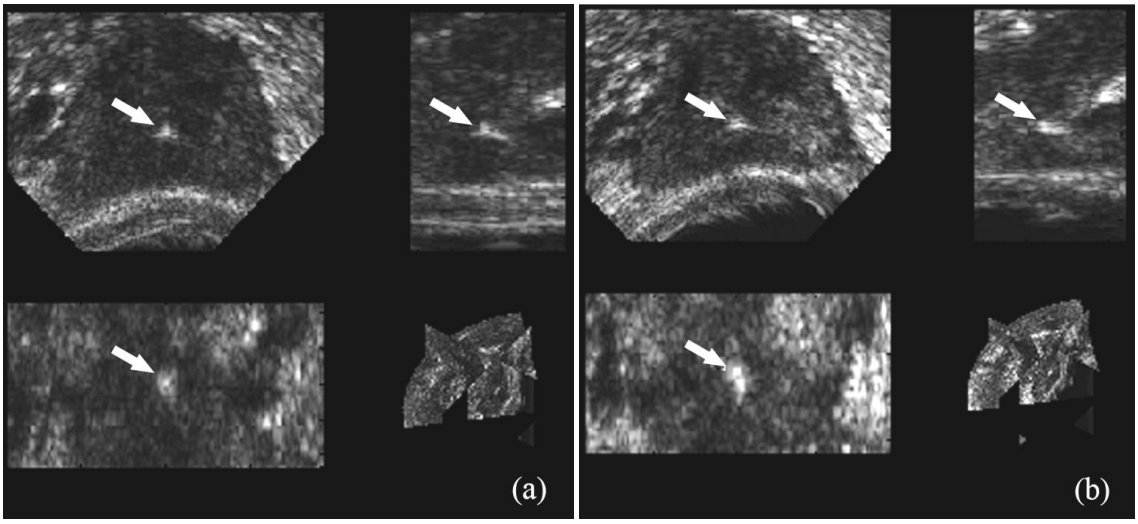

Figure 5.3 An example of an echogenic TRUS image feature, indicated by the arrow, used to evaluate registration accuracy. (a) and (b) illustrate the feature in 3 orthogonal views in the source and target images, respectively. The centre point of such features was defined manually.

5.3.2 Comparison with Alternative Methods

An alternative method for surface-driven deformable registration is to assume a simple elastic deformation within an organ (Bharatha et al. 2001;Haker et al. 2004). This is equivalent to performing a biomechanical simulation with boundary conditions specified by a force or displacement field at the surface. Typically, surface displacements are determined by an initial deformable registration of the source and target surfaces. In this work, elastic registrations were compared using surface displacements determined after first registering the surfaces using the RPM algorithm (in which the deformation is computed using thin-plate-splines) (Chui et al. 2002), and the CPD algorithm (Myronenko et al. 2010).

To ensure consistency with the SMM-based method, the FE model, derived from each source image (the un-deformed TRUS volume in this case) was used to compute the 3D displacement

field within the prostate gland. Biomechanical simulations were performed using the same non-linear solver as described earlier. Given the lack of published data on the difference in material properties of the prostate zones, the prostate was considered to behave as a homogenous material and, *G* and *K* were set to the median values of the corresponding ranges (*40.1kPa* and *1.67GPa*, respectively) used to generate the SMM described above for both inner and outer compartments of the gland .

5.4 Validation of TRUS-MR Registration

5.4.1 Landmark-based Accuracy Validation

To evaluate the performance of the proposed registration method, 100 MR-TRUS registrations were performed for each of eight patients. The model-to-image registration algorithm was implemented in MATLAB, and a quick and simple initialisation procedure was adopted in which two points at the apex and base of the gland were identified manually in the TRUS volume (see Section 4.2.3). Once registered, a dense displacement field (DDF) was computed from the final instance of the deformable FE mesh by interpolation.

In order to simulate variability in the initialisation base and apex points and to investigate the robustness of the registration algorithm given different model starting positions, a random starting position was set before each registration by adding a random error ≤ 5mm, drawn from a uniform probability distribution, to each of the *x*-, *y*-, and *z*-components of the original, manually identified apex and base points. The accuracy of each registration was quantified by computing the final TRE between corresponding anatomical landmark points, identified in the MR and TRUS images, following registration. The 3D co-ordinates of landmarks, defined in an MR image, were then transformed into TRUS co-ordinates using the DDF.

The landmarks used for estimating the TREs were identified manually by a urological surgeon with over five years experience in interpreting prostate ultrasound and MR images. For each prostate, the following three landmarks were defined in both the TRUS and MR volumes on three separate occasions: the point in the centre of the urethra as it enters and exits the prostate – i.e. at the base and apex of the gland – and the centre point where the ducts of the seminal vesicles emerge from the gland. In addition, the locations of the centres of small cysts and calcifications appearing inside the gland were identified, again on three separate occasions. In general, cysts appear as low-intensity (hypoechoic) features in the TRUS images and high-

intensity regions in the MR, whereas calcifications appear with high intensity (hyperechoic) in the TRUS images and low intensity in the MR. All landmarks were defined by identifying the image co-ordinates in three orthogonal slices. The gold standard position for each landmark was found by averaging the co-ordinates defined on three separate occasions.

For each pair of gold standard landmarks, the TRE was defined as the RMS Euclidean distance between the landmarks originally defined in TRUS co-ordinates and the location of the corresponding MR landmark following propagation into the TRUS space. MR images were also warped into the TRUS co-ordinate system using the DDF to allow visual assessment of the MR-TRUS registration.

To estimate the precision of localising individual landmarks, a landmark localisation error (LLE) was computed. For each landmark, the LLE was defined as the RMS distance between the gold standard (i.e. mean) landmark co-ordinates and each of the three landmark co-ordinates defined by the expert observer.

5.4.2 Clinical Targeting Criteria

Although real clinical workflow and processes are highly complex and case-dependent, quantifying the clinical relevant error is possible given some simplifying assumptions reflecting clinically important scenarios. For instance, adopting the widely used cut-off of 0.5 cm^3 for clinically significant tumour volume, and assuming that the centre of clinically significant target tumours can be localised with negligible error, negligible needle deflection, and, for simplicity, a spherical and pathologically homogeneous tumour, a targeted tumour will be hit when the system targeting error is less than 4.92mm (equal to the radius of a 0.5cm^3 sphere). Furthermore, assuming that the targeting error is normally distributed with variance σ^2 in each of the *x*-, *y*-, and *z*-components, the targeting error, defined as the distance between the true centre of the target tumour and a target point calculated by the image guidance system will follow a Maxwell-Boltzmann probability distribution. Using the analysis described below, it gives analytical expression of the distribution of the distance, i.e. targeting error.

Assuming that the errors, δ_x, δ_y, and δ_z, in each of the co-ordinates of a targeted point follow a normal distribution with zero mean and variance σ^2, the distance error x, in hitting the target is given by:

$$x = \sqrt{\delta_x^2 + \delta_y^2 + \delta_z^2} \tag{5.5}$$

and follows a Maxwell–Boltzmann probability distribution with PDF:

$$P(x;a) = \frac{1}{\sigma^3}\sqrt{\frac{2}{\pi}}x^2 \exp\frac{-x^2}{2\sigma^2}, x \in [0,\infty) \tag{5.6}$$

The corresponding cumulative probability distribution is:

$$D(x;a) = \operatorname{erf}\left(\frac{x}{\sqrt{2}\sigma}\right) - \frac{1}{\sigma^3}\sqrt{\frac{2}{\pi}}x \exp\frac{-x^2}{2\sigma^2}, x \in [0,\infty) \tag{5.7}$$

Now, the TRE, defined as the RMS value of x, is given by:

$$TRE = \sqrt{\frac{\int_0^\infty P(x)x^2dx}{\int_0^\infty P(x)dx}} = \sqrt{\frac{1}{\sigma^3}\sqrt{\frac{2}{\pi}}\int_0^\infty x^3 \cdot x \exp\left(\frac{-x^2}{2\sigma^2}\right)dx} \tag{5.8}$$

Integrating this expression by parts, we have:

$$TRE = \sqrt{\frac{1}{\sigma^3}\sqrt{\frac{2}{\pi}}\left[-\sigma^2 x^3 \exp\frac{-x^2}{2\sigma^2}\right]_0^\infty + 3\sigma^2\int_0^\infty x^2 \exp\frac{-x^2}{2\sigma^2}\mathrm{d}x} = \sqrt{3}\sigma \tag{5.9}$$

Setting a desired hit rate of 90% for hitting a spherical tumour region with a radius of 4.92mm, the upper limit on σ, denoted by σ_{max}, is given by:

$$\sigma_{max} = arg\max_\sigma [D(x \le 4.92;\sigma) \ge 0.9] \tag{5.10}$$

Since D is monotonically increasing with x and monotonically decreasing with σ, we obtain:

$$\sigma_{max} = arg[D(x = 4.92;\sigma) = 0.9] = 1.97 \tag{5.11}$$

Therefore, using the result from (5.9), the corresponding TRE threshold is $\sqrt{3}\sigma_{max}$= 3.41mm.

Given this distribution, the TRE, expressed as the RMS distance error, is equal to $\sqrt{3}\sigma$, given a particular threshold on the (clinically significant) tumour hit-rate, it is possible to derive the corresponding TRE threshold which any specified hit-rate will be achieved.

5.4.3 Comparison with Alternative Registration

As a comparison, the same model-based registration framework, with the same parameter settings, was used to rigidly register the original gland surface segmented from MR to the TRUS image, but where the step in which the shape parameters are estimated was omitted. Again, registrations were performed using the same random initialisations as used for the non-rigid registrations, and the TRE was computed by propagating the landmarks using the resulting rigid transformation.

One useful property of an SMM, unlike general-purpose non-rigid (or elastic) transformations, is that it ensures that prostate gland deformations are highly constrained and incorporate prior knowledge on the range of deformations expected during a procedure. This feature is particularly important for robust registration to ultrasound images because the low signal-to-noise ratio and artefacts associated with this modality. Alternative transformation models have been proposed, such as the linear-elastic volumetric warping methods used by Bhartha et al. (2001), Haker et al. (2004), and Narayanan et al. (2009). In these studies, a FE model was used directly to compute the image deformation field following a surface-based registration, which sets the boundary conditions at the surface of the gland. To compare other methods described in the literature with the approach proposed in this thesis, the accuracy of an alternative elastic registration algorithm is computed, in which the non-linear FE solver was used to determine the deformation field given surface displacements found by registering the MR-derived gland surface to the surface segmented manually from the TRUS image.

In this experiment, the prostate gland surface of the FE mesh used to build the SMM was chosen as the source surface. This was then registered to a dense set of TRUS target surface points using the CPD algorithm (Myronenko et al., 2006; 2009). The values of G and K for the interior of the gland were set to 40.1kPa and 1.67GPa, respectively. These values are the average values of the corresponding ranges shown in Table 3.1. As with the SMM-based method, the solution provides a volumetric displacement field across the gland, which is used to propagate landmarks. As before, TREs were computed by measuring the distance between each propagated landmark and the corresponding landmark identified in the target TRUS image.

Chapter 6 Experiments and Results

This chapter presents experimental results based on the evaluation methods introduced in Chapter 5. Experiments of material sensitivity analysis, model comparison and registration validations with associated quantitative and qualitative results are also presented in this chapter.

6.1 Experiments and Results for Sensitivity Analysis in Material Property

The data used in this analysis is the same as in the TRUS-to-TRUS experiment, with five patient data sets described in Section 6.3.1, and 100 simulations performed for each pair of images. Three tests, described in Section 5.1, were performed independently.

The influence of allowing *K* and *G* to vary (Test 1), compared with assuming incompressibility (Test 2) and with one degree of freedom in material properties fixed (Test 3), is indicated by the results in Table 6.1. Overall, it can be seen that allowing *K* and *G* to vary results in a significant relative node displacement with respect to the reference cases.

Patient	**Relative displacement (%)**			
	Difference between Test 1 and 2		**Difference between Test 1 and 3**	
	Median	**5^{th} – 95^{th} percentile**	**Median**	**5^{th} – 95^{th} percentile**
1	11.9%	2.48 - 57.8%	5.94%	1.30 - 35.7%
2	21.3%	4.87 - 102%	10.8%	2.35 - 49.0%
3	15.9%	3.19 - 72.2%	6.96%	1.66 - 29.6%
4	16.6%	3.39 - 71.1%	7.97%	1.39 - 36.4%
5	18.1%	3.38 - 70.9%	6.99%	1.58 - 31.3%

Table 6.1 Sensitivity of tissue displacements predicted by FE simulation due to changes in material properties

This result provides a motivation for including variation in *K* and *G* in the SMM training simulations so that an SMM built using these data represents the full range of deformations that might be encountered in reality.

6.2 Experiments and Results for Comparison of Statistical Motion Models

6.2.1 Data

T2-weighted MR images were acquired on 7 patients. The details of the acquisition of these images are provided in Section 6.4.1. Multiple organs were manually segmented as described in Section 3.2.1.2. These segmentations were used to generate the 6 different SMMs (five of which

were configured as a "simplified" model, as summarised in Table 3.2), and 500 FE simulations were performed for each model to provide training data. Each training sample was generated after randomly assigning material properties and boundary conditions based on the ranges given in Table 3.1.

All 3000 simulations were performed using a C++ implementation of a fast, non-linear FE solver (Taylor et al. 2008) on a desktop PC with a 2.33GHz Intel® Core™ dual CPU processor, 3GB of RAM, and a 256 MB NVIDIA® GeForce™ 8600 GT graphics processing unit (GPU) installed. Mesh node displacements were computed using the GPU. A four-node formulation was adopted to overcome the volumetric locking problem (Bonet et al. 1998;Joldes et al. 2009). Using this method, the time taken to complete 500 simulations was approximately 140 minutes. For example, simulations took on average 16 seconds to compute the deformation of an FE model containing on average 45,000 elements. These simulations together with the segmentations formed the data required in the comparison study.

6.2.2 Experiment and Result

After computing the compactness, the leave-one-out schemes were performed to compute generalisation ability and specificity. The procedures were described in Section 5.2 and illustrated in Figures 5.1 and 5.2.

6.2.2.1 Model Compactness

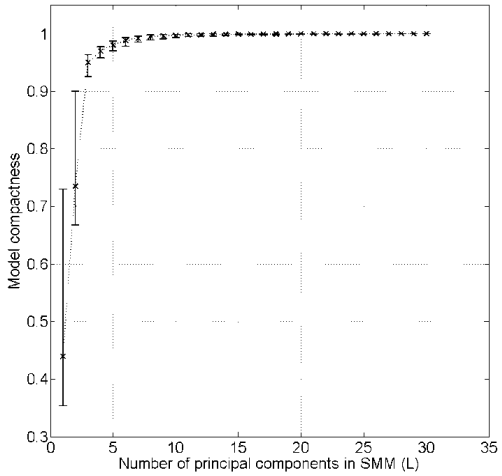

Figure 6.1 Plot of the median compactness (with 95% confidence interval) for all of the SMMs as a function of the number of principal components (*L*).

Total of 42 SMMs were generated for 7 patients using 6 different FE model configurations. Figure 6.1 shows the median and 95% confidence interval of the compactness, described in

Section 5.2.2.1, computed for different values of *L* (from 1 to 30). As can be seen from Figure 6.1, increasing the number of modes of variation of the SMM increases cumulative relative variance of the model compared with the training data, and the compactness converges to a value close to one for *L>9*. It was found that 99.5% of total tissue motion variance was captured for all of these models if *L*=12. This number was adopted when computing generalisation abilities and specificities presented below.

6.2.2.2 Generalisation Ability

The generalisation abilities, computed for each SMM, using the three model fitting methods described in Section 5.2.1 are plotted in Figure 6.2. There was found to be little difference between the accuracy of SMMs built using simplified FE models (SMM 2-6) and the SMM based on the fully-specified FE model (SMM 1) in terms of generalisation ability, with the latter SMM yielding the highest accuracy. Similar results were obtained when only surfaces were used to register the models. By comparing the results in Figure 6.2, very little difference was found between using the surface node points and all internal gland node points when point correspondence was known. The errors were slightly larger in the more realistic case when only a surface is used for registration and the point correspondence between the SMM and target surface is unknown.

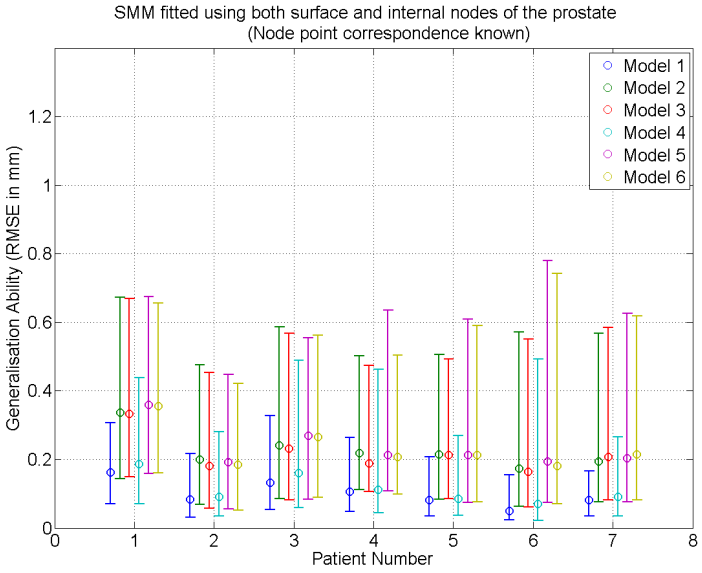

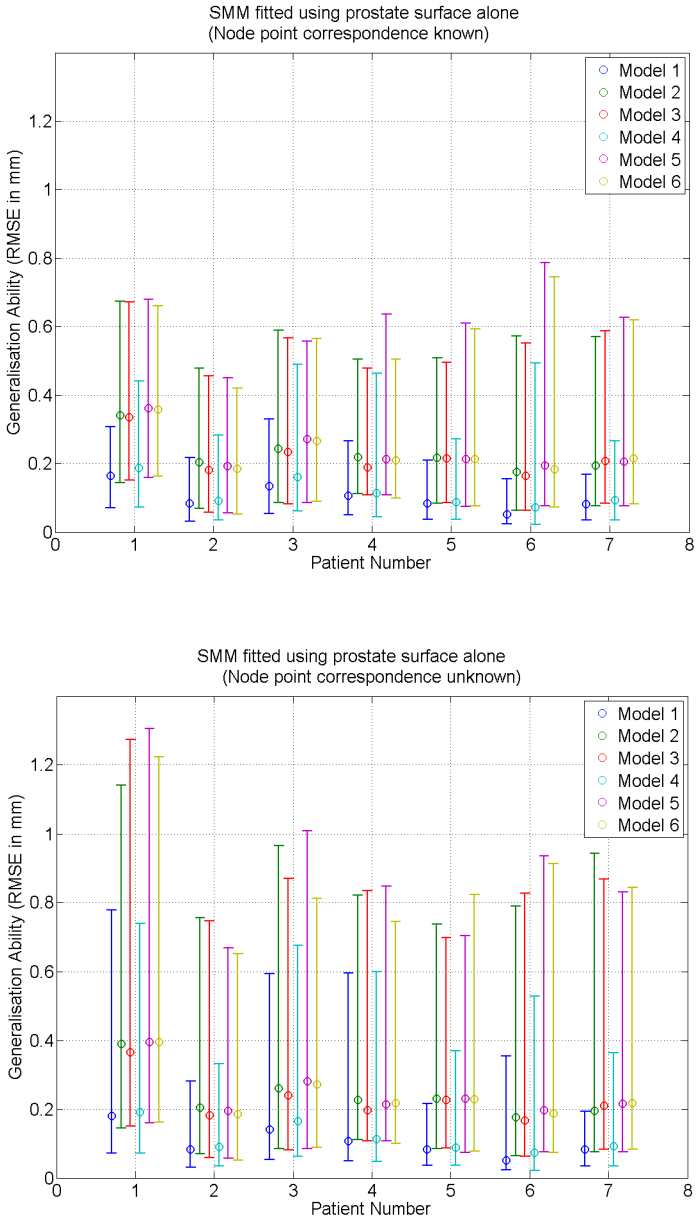

Figure 6.2 Generalisation abilities (described in Section 5.2.2.2) for 6 SMMs (summarised in Table 3.2) across 7 patients, shown as the median RMSE and 95% confidence interval, for three different model fitting methods (see Section 5.2.1).

Of the SMMs based on simplified FE models, SMM 4 was consistently found to be the most accurate. Since this model was based on an FE with anatomically realistic pelvic boundary conditions, this result suggests that that the model is sensitive to the geometry of the pelvis. However, the difference in median error between using an SMM based on a FE model with simplified pelvic boundary conditions and SMMs based on an FE model, which reflects the true anatomy of the pelvic bone, was small – between 0.1 and 0.2mm. Based on a review of the

relevant literature and discussion with collaborating clinicians, this level of error is acceptable for the MR-TRUS prostate registration application.

Further inspection of Figure 6.2 reveals very little difference between the accuracy of the different SMMs that were based on FE models with planar pelvic boundary conditions (SMMs 2, 3, 5 and 6). This result suggests that simply using the average positions from measurements made on a group of patients may be sufficient for the purposes of SMM generation. This insight naturally leads to a MR segmentation protocol in which only the prostate capsule would need to be segmented.

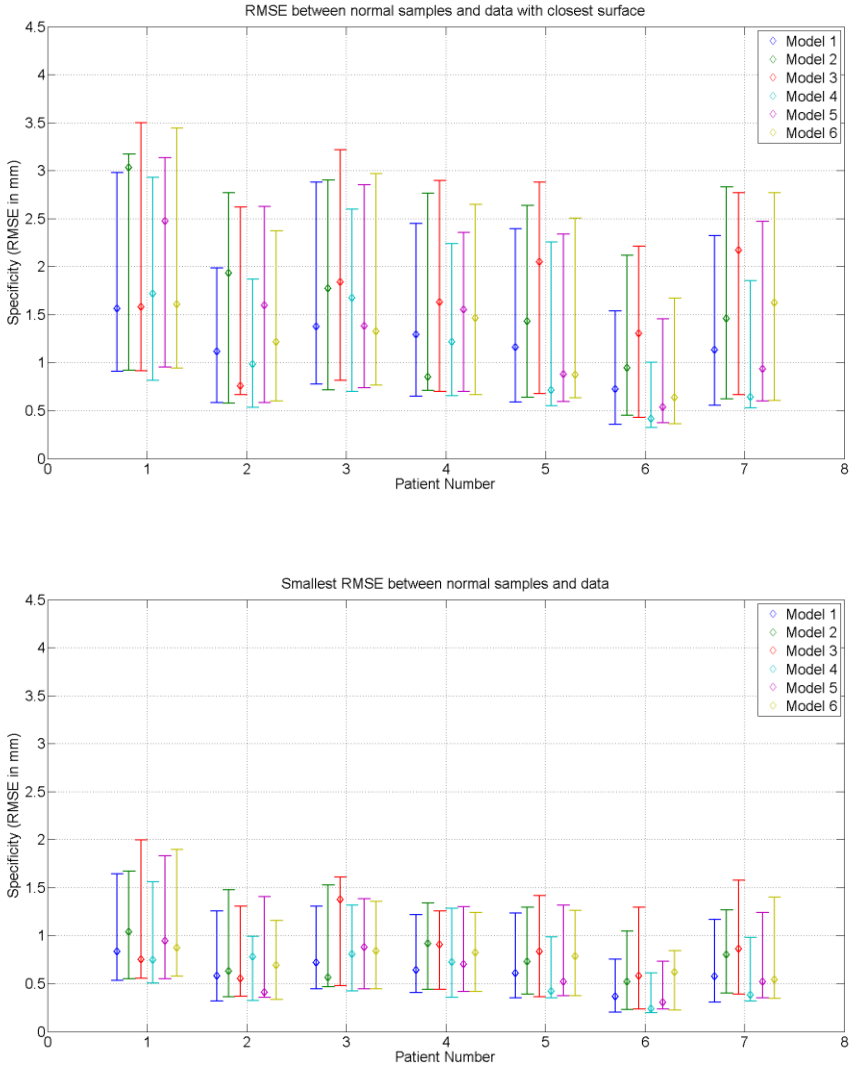

Figure 6.3 Model specificities (described in Section 5.2.2.3) for 6 SMMs (summarised in Table 3.2) across 7 patients, shown as the median RMSE and 95% confidence intervals.

6.2.2.3 Model Specificity

The model specificities are shown in Figure 6.3 compared with the generalisation ability, there was found to be a much smaller difference between the SMMs based on simplified FE models and the fully-specified SMM in terms of specificity.

6.2.3 Discussion

Combining biomechanical modelling and statistical shape modelling techniques to predict soft-tissue motion overcomes the problem of needing to specify accurate values for tissue material properties and application-specific boundary conditions by taking into account variations in these properties. Such techniques are particularly useful for time-critical applications, such as image-guided surgery, since SMMs are linear models with far fewer parameters than the underlying biomechanical model and therefore can be instantiated very rapidly.

However, the sensitivity of SMMs based on biomechanical simulations to the complexity of the biomechanical model is an important issue that has received very little attention in the literature. Conventional logic suggests that as accurate a biomechanical model as possible is desirable for this purpose, but often there is significant burden in creating such a model, particularly if a new model needs to be built for each new patient, as in this thesis. Since automatic, multi-organ segmentation tools are not widely available, this burden may have a significant impact on the clinical workflow required to use motion modelling techniques in clinical applications.

Since uncertainty is inherently taken into account by the statistical modelling, it can be argued that the accuracy of the underlying biomechanical model is of relatively little importance compared to its ability to capture the typical variation in organ motion. The results of this thesis support this hypothesis, and suggest that it is possible to simplify the FE model used to generate training data considerably without a significant impact on the accuracy of the associated SMM. This is based on both acceptable results of generalisation abilities and specificities reported in this work.

One limitation of this thesis is that a (fully-specified) FE model was used to compute the ground-truth deformation, which may not necessarily reflect true tissue motion. However, the success of this approach for image registration in initial work (Hu et al. 2011a;Hu et al. 2008a) suggests that is a reasonable approximation for the TRUS-probe-induced motion of the prostate gland.

Moreover, using patients' intraoperative data for validation could produce extra error due to registration method, which is beyond the scope of this comparison work, however, will be part of future investigation. It should be noted that the SMMs based on simplified geometry will not alter any of the procedures in using the previously proposed original SMMs.

6.3 Experiments and Results for TRUS-TRUS Registration

6.3.1 Data

Three-dimensional TRUS images of the prostate were acquired for five patients undergoing a template-guided, transperineal biopsy, or HIFU ablation or photodynamic therapy (PDT) for treatment of prostate cancer. All patients were recruited to clinical research studies at University College London Hospital, London, UK, and gave written, informed consent to participate in studies that were approved by the local research ethics committee. In the case of biopsy and PDT, a set of parallel transverse B-mode ultrasound images was obtained using a B-K ProFocus scanner (B-K Medical, Berkshire, UK) and a mechanical stepper mechanism (Tayman Medical Inc., MO, USA) to translate the probe (B-K 8658T, 5-7.5MHz transducer) axially through the rectum. Images were captured at 2mm intervals and stored on the ultrasound scanner. In the case of HIFU therapy, 3D volumes were acquired automatically using a Sonablate® 500 system (Focus Surgery, Inc., Indiana, USA).

Two volumes were acquired for each patient at the start of the procedure: one with the balloon at minimal expansion, and the other after expanding the balloon by injecting saline with a syringe in order to deform the prostate gland. Expanding the balloon in this way simulates one source of motion of the prostate gland that typically occurs during the placement of a TRUS probe (or, equivalently, an endorectal MR imaging coil). The first volume was chosen as the source image for building the TRUS-derived SMM, whilst the second was used as the target image for accuracy evaluation.

6.3.2 Experiment and Result

6.3.2.1 Model Generalisation Ability

The generalisation ability for each of the 15 models (3 models for each of 5 patients, described in Section 5.3.1) is plotted in Figure 6.4. As can be seen from the plot, the absolute value of RMS error in millimetres is numerically small, particularly when compared to the level of error obtained in the registration experiments, for instances, the results presented in Tables 6.3.

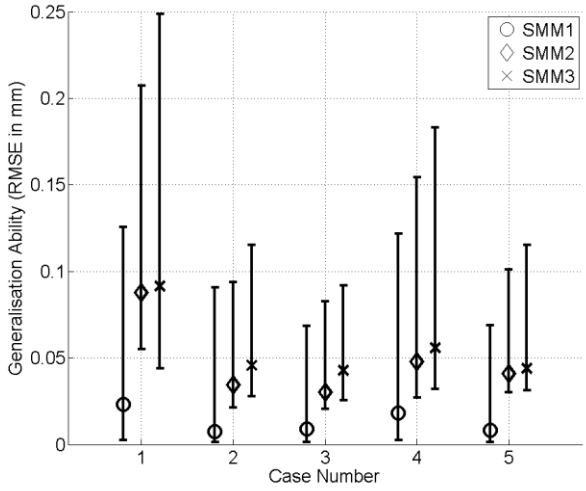

Figure 6.4 Generalisation ability for all the 15 SMMs generated in this thesis. The median and 5% - 95% percentiles are shown for each model.

6.3.2.2 Registration Accuracy

The target-point-to-surface distances following SMM-based and elastic/rigid registration algorithms are plotted in Figures 6.5 and 6.6, respectively. Comparing the results for the three SMMs presented in Figure 6.5, it can be seen that a better fit to the target points was obtained as the number of degrees of freedom included in the training data increased. There was, however, little difference between the errors for SMM2 and SMM3, indicating that including variability in the pose and size of the pelvic bone in the training FE model made little difference to the range of surface captured by the resulting SMM. In contrast, the point-to-surface errors are considerably higher for SMM1 compared with SMM2 and SMM3. This result suggests that introducing variability into the pose of the TRUS probe in the training data improves the ability of the SMM surface to fit the target points, even though the physical gland motion was due to an increase in balloon radius (modelled in the training data for SMM1). The most likely explanation for this is that some rotation of the gland may have occurred because of non-uniform deformation of the balloon or patient motion that is equivalent to a change in the pose of the probe/balloon.

Inspection of Figure 6.6 reveals that the CPD and RPM methods provide a better surface fit to the target points compared with the SMM-based and rigid registration methods, particularly when very few of points are used (point sets PS3 and PS4). This is due to the fact that the deformation permitted by the SMM is relatively constrained. Nevertheless, a point-to-surface distance within 3.5mm was achieved using all methods, including the rigid-registration.

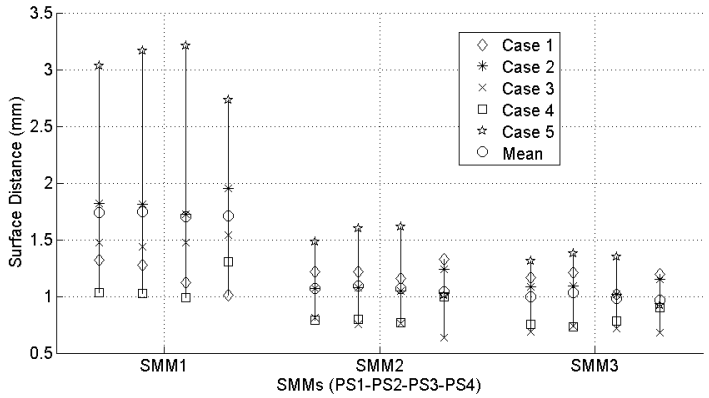

Figure 6.5 Final target-point-to-surface distances after registering models SMM1, SMM2 and SMM3 to target point sets PS1-PS4 (shown from left to right) for 5 patients.

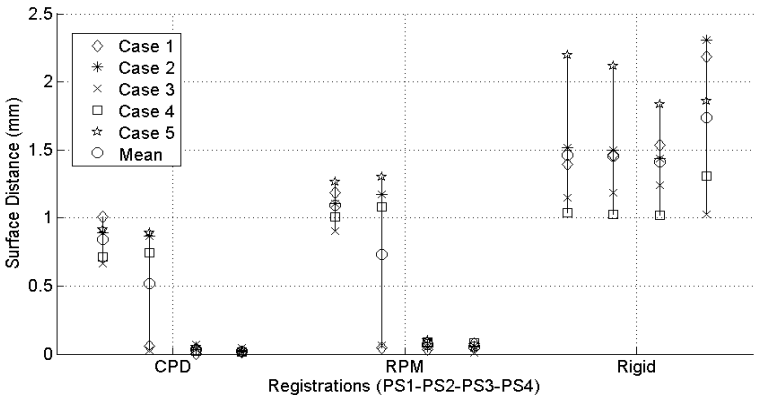

Figure 6.6 Final target-point-to-surface distances following surface-based registration to target point sets PS1-PS4 (from left to right) using the CPD, RPM and rigid ICP algorithms on 5 patient datasets.

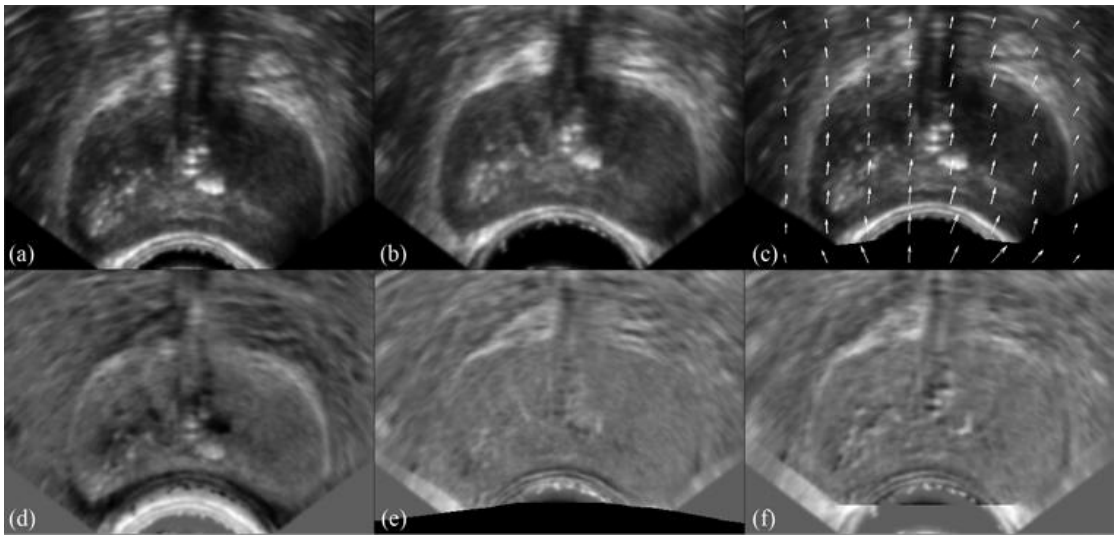

Figure 6.7 Example transverse slices through 3D TRUS images (Case 1). From top left: (a) Source image (balloon minimally expanded); (b) Target image (balloon maximally expanded); (c) Source image after warping using the interpolated displacement field (shown as white arrows), generated by registering the SMM; (d)-(f) show subtraction images: (d) target – source (b – a); (e) target – warped source (b – c); (f) target – source after rigid registration.

Figure 6.7 shows example slices through the source TRUS volume before and after registration to the target volume using the SMM-based method. The original source image (Figure 6.7a) has been warped using the displacement field after interpolating to find the displacement at the centre of each voxel. The initial landmark TREs are summarized in Table 6.2. The mean (± standard deviation) TRE was 5.80 (± 0.66) mm for all 71 landmarks across 5 patients. The landmark-based TREs for the SMM-based method are plotted in Figure 6.8 and a summary of the numerical errors is provided in Table 6.3. Inspection of the results reveals that in all cases the lowest TREs were achieved by using the SMM2 and SMM3 to constrain the deformable surface registration. Furthermore, the largest TREs were obtained when registering the smallest number of target points (PS4). However, for larger point sets (PS1-PS3), the number of points had very little influence on the TRE. No registrations failed and all were completed within 30s on a PC with a 2.33GHz Intel® Core™ dual CPU processor and 3GB RAM.

Case No.	**1**	**2**	**3**	**4**	**5**	**All**
Number of landmarks	17	12	15	15	12	71
Initial TRE (in mm)	6.48	5.24	5.17	5.58	6.54	5.80 ± 0.66 (Mean ± SD)

Table 6.2 Initial landmark TREs

Point Set	**Mean±SD TRE in mm**		
	SMM1	**SMM2**	**SMM3**
PS1	2.34±0.22	1.63±0.21	1.68±0.23
PS2	2.32±0.25	1.59±0.16	1.65±0.15
PS3	2.36±0.22	1.69±0.14	1.69±0.18
PS4	2.42±0.20	2.26±0.69	2.08±0.61
All	2.36±0.21	1.79±0.44	1.77±0.37

Table 6.3 Final TREs for SMM-based registrations

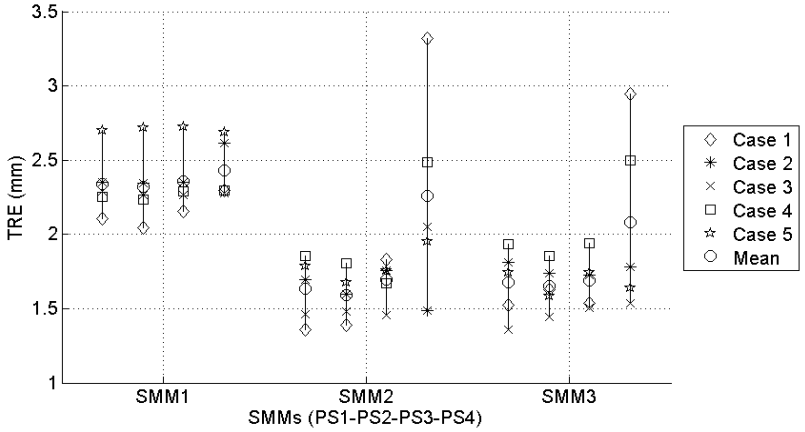

Figure 6.8 TREs after registering models SMM1, SMM2 and SMM3 with four target point set (from left, PS1-PS4 – see Table 5.1) for each of the 5 patient cases.

TREs for the elastic and rigid registrations are shown in Figure 6.9 and Table 6.4. Notably, the results show that in most cases the rigid registration was more accurate than the elastic registration methods, although considerably less accurate than the SMM-based registration method, overall. Intuitively, these observations may be explained by the fact that the rigid registration is the most constrained, allowing no deformation of the prostate model, whereas since the elastic registration is subject to purely geometric constraints governed by the initial surface registration, physically implausible shape changes are possible. This is particularly the case when a small number of target points are used. An example is illustrated in Figure 6.10 where although the fit to target points is typically very accurate, the shape of the deformed prostate surface is poorly representative of a real deformation. In a number of cases, this effect resulted in a failed registration due to an inability of the FE simulation to converge to a solution given poorly constrained boundary displacements. In contrast, the inherent shape constraints applied during SMM-based registrations avoid ill-posed boundary conditions, but permit physical deformations. This was verified by the fact that computing the Jacobian ratio at integration points of the tetrahedron elements following registration revealed no badly shaped elements (indicated by a negative or a large value >40).

Therefore, one advantage of using an SMM-based scheme as proposed in this thesis is that it is still possible to successfully register the model surface to a relatively small number of target surface points without introducing implausible shape changes or compromising the registration accuracy. This property may be especially useful in interventional applications, where the time available to define target surface points is usually limited during a procedure. When performed manually, contouring the entire gland surface in target TRUS images is particularly time-consuming, and this task may need to be repeated during the procedure. Therefore, the ability to register using sparse surface data reduces the need for automatic or semi-automatic segmentation tools, making the technique practical for interventional use.

Point Set	**Mean±SD TRE mm (number of failed registrations)**		
	CPD	**RPM**	**Rigid**
PS1	3.91±0.53	4.14±0.54	3.40±1.02
PS2	3.89±0.51	4.48±0.54 (2)	3.34±0.96
PS3	3.87±0.54	-- (5)	3.32±0.81
PS4	-- (5)	-- (5)	4.18±1.16
All	3.89±0.49 (5)	4.27±0.53 (12)	3.56±0.99

Table 6.4 Final TREs for elastic and rigid registration methods

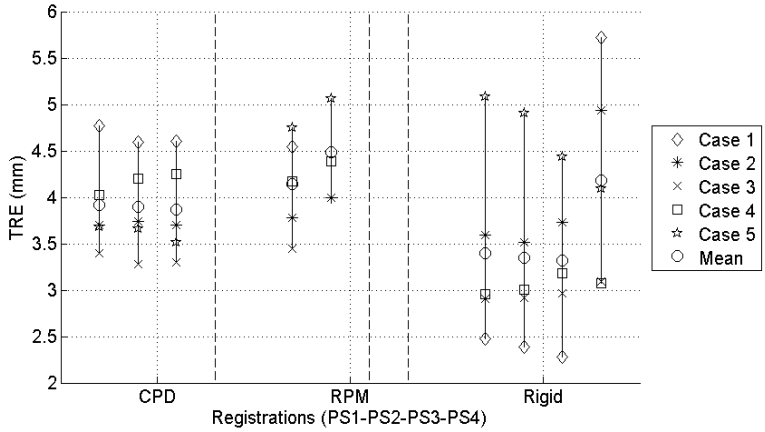

Figure 6.9 TREs after elastic registration using point correspondence determined using the CPD and RPM surface-based registration algorithms, compared with rigid-body registration using the ICP algorithm. Results are presented for the four target point sets (from left to right, PS1-PS4) for each of the 5 patient cases. The vertical dashed lines denote the cases where all of the registrations failed due to lack of convergence of the FE simulation.

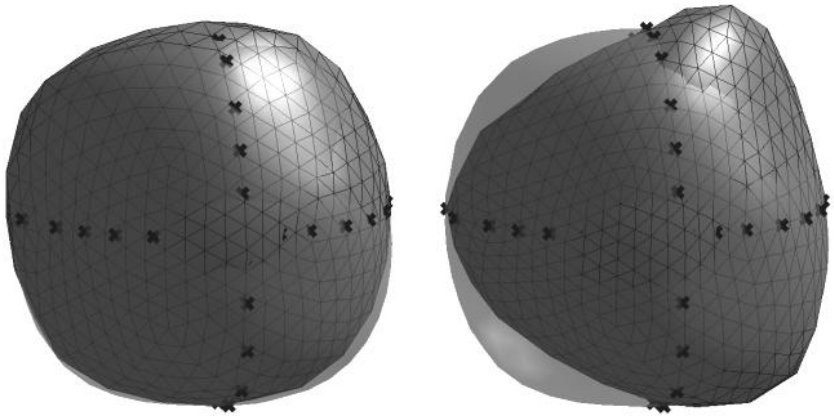

Figure 6.10 Example of registering a prostate gland surface to a small number of target points (shown as crosses) using an SMM (left, an SMM2 in this case) and the CPD method (right). Although a close fit to the target points is achieved in both cases, the CPD registration is relatively poorly constrained, leading to a physically implausible final shape.

6.3.3 Discussion

In Section 6.3.2, results were presented from a method that combines statistical motion modelling techniques with FEA to generate patient-specific, 3D deformable models of the prostate gland for use in a non-rigid image registration framework. The results indicate that the models have the desirable property that they deform in a physically plausible manner, but are sufficiently constrained to be registered rapidly and accurately using only a relatively small number of target surface points, for example, points identified from typical TRUS views.

As in previous related studies, linear SMMs were generated using PCA. The validity of using such a linear model for the data collected in this thesis was verified by computing the generalisation

ability for each model. This metric, expressed as an RMS error in node displacement, was found to be very small with a median value < 0.1mm. Therefore, it can be concluded that the accuracy of the linear, PCA-based SMM adopted in this thesis is sufficient to represent TRUS-probe-induced prostate deformations simulated by FE modelling with an acceptable error for this application. It is important to note that both high generalisation ability and high specificity (the ability to reject an implausible motion, see Section 5.2.2) are significant here, as this leads to a robust registration with respect to a sparse target data, as verified by the experiments. Such properties are key to successful motion models in the ultrasound-based registration tasks. For instance, as shown in Figure 6.8, the SMM2 and SMM3 produced significantly smaller registration errors than SMM1 except for the case of PS4. It is expected that the modelling accuracy would decrease when less information is provided. It appears that this is the point where the model provides most of its modelling ability to balance the demands of input information and maintain the acceptable registration accuracy,

From the comparison study carried out in the previous section, the established alternative approach of adopting an elastic deformation, driven by a surface-based registration, was found to be both considerably less accurate and more robust than the SMM-based method, particularly when registering to a limited number of target points.

A possible reason for the discrepancy between the accuracy of the elastic versus SMM-based method is that the former requires *a priori* assignment of tissue material properties within the gland, whereas the SMM-based method essentially learns deformations for a wide range of material properties. Given the known variability in tissue properties and the sensitivity of tissue displacements predicted by FE simulations to variation in these properties, this may be a significant limitation for elastic registration methods driven purely by surface displacements.

The TRE of approximately 4.0 ± 0.5mm for the elastic registration methods, computed after registering patient TRUS data, is comparable with a TRE of 3.1 ± 1.4mm for a MR-to-TRUS registration of a phantom prostate reported by Narayanan et al. (Narayanan et al. 2009). Furthermore, the superior registration errors calculated for the SMM-based method (TRE ~1.6 ± 0.2mm) compare favourably with errors recently reported for non-rigid MR-MR registration (Oguro et al. 2009). In that study, the mean fiducial registration error (FRE) – equivalent to the TRE metric adopted in this thesis – was 2.8 ± 1.8mm after registering preoperative 1.5T MR images of prostates of patients in the supine position to 0.5T interventional MR images acquired

during MR-guided brachytherapy with the patients in the lithotomy position. An intensity-based B-spline registration algorithm was used for this purpose, but it is difficult to see how this algorithm could be easily adapted to TRUS-MR image registration given the substantial differences in intensity characteristics typically found between these modalities.

Recent advances in diagnostic MR imaging and robotic needle insertion (e.g. (Xu et al. 2010)), mean that high-accuracy image registration is of increasing importance in achieving precisely targeted prostate cancer biopsy and treatments. Although a registration based on an SMM can be executed rapidly, making it well-suited for time-critical applications, there is a significant additional time overhead associated with generating the SMM. It is important to note, however, that this task is completed prior to a procedure, when there is generally more time flexibility. It is envisaged that in practice a patient-specific surface model would most likely be based on a preoperative MR image, for an MR-derived SMM, segmented either by a radiologist or a surgeon (Hu et al. 2009;Hu et al. 2012). This process could be performed manually, but it is now feasible to speed-up this process significantly using any of a number of computer-aided MR segmentation tools recently reported in the literature (Makni et al. 2009;Martin et al. 2010). As shown in this thesis, the FE simulation and SMM construction steps are then fully automatic and require no further input from a clinical expert.

In the experiments carried out for this thesis, TRUS-to-TRUS registration was adopted primarily to provide a well-controlled framework for validating the performance of TRUS-derived SMMs. However, it is possible that the method described here might be usefully applied for TRUS-TRUS registration, for example, if a preoperative 3D TRUS image is available, or as an intermediate step for multimodal image registration to account for gland motion during a procedure (Baumann et al. 2009). In this approach, new TRUS data is registered to an initial TRUS volume that has already been registered with a treatment/biopsy plan or image at the beginning of the procedure. Baumann et al. (Baumann et al. 2009) describe a fast, non-rigid intensity-based method for TRUS-to-TRUS registration, but it is unclear how well their approach is able to cope with progressive changes in ultrasound image intensity, for example due to needle injury or ablation during a procedure. As the model-based approach described here has been shown to be robust to sparse surface data, this method may have the advantage of being relatively insensitive to such changes. This issue will be investigated in future work.

The FE model and applied boundary conditions used to generate training data involved the following simplifying assumptions: firstly, it was assumed that the prostate gland can be modelled as a two-compartment structure, surrounded by homogeneous material. Also, tumours were not explicitly modelled as they were not directly visible in the TRUS data. Given the widely reported difference in stiffness between tumours and healthy soft-tissue this may limit the registration accuracy achievable, although it is likely that only large tumours (>1cc) would potentially have significant impact on simulated deformations. The effects of incorporating MR-derived information on tumours into the SMM are investigated in Section 6.4. Secondly, in this thesis only the relatively simple deformation case has been modelled where the balloon surrounding a TRUS probe is expanded and the probe itself is clamped to a stepping device. Nevertheless, this is an important source of motion during template-guided transperineal biopsy, HIFU therapy, and transperineal needle-based therapies, and successful compensation for this source of registration error represents a significant advance on the conventional assumption of rigid-body motion. The modelling framework described here could be readily adapted to model gland motion from transrectal biopsy, for example, by extending the ranges of probe positions and orientations modelled in the training data to reflect those that are likely to be encountered in practice, but this may necessitate a more complex contact FE model to model adequately prostate deformations as the probe/balloon slides over the rectal wall during these procedures. The training model could also be further extended to account for more complicated scenarios, such as changes in patient position between imaging sessions (Hirose et al. 2002).

Since full information on the shape and relative location of the pelvic bone was not available from the TRUS images, a generalised pelvic model was used to constrain the prostate deformation. However, comparing the TRE results for SMM2 and SMM3 in Table 6.3 and Figure 6.8 indicates that changing the dimensions and position of the pelvic bone in the FE model makes very little difference to the registration accuracy. A difference was found between the accuracy of SMM1 and SMM2/3, implying that modelling a simple TRUS balloon expansion alone (SMM1) achieved a less accurate registration compared with introducing additional variability in the pose of the TRUS probe/balloon, but this may be explained by the fact that although the physical deformation was caused by a balloon expansion, there may also have been additional tissue or patient motion, combined with some change in shape of the balloon itself, that is captured by SMM2 and SMM3.

A further important source of shape variation is due to differences in the manual segmentations produced by different observers. The impact of this variation was not investigated and remains the subject of future work. There is no fundamental reason, however, why this source of variation could not be included in the training data by building a model using prostate segmentations from multiple observers, or segmentations by the same observer on different occasions.

Furthermore, although forces exerted by the bladder are known to influence the position of the prostate (Byrne 2005), the bladder was not included in the FE model since again information on its shape and location were unavailable from the TRUS images. It was therefore assumed that the influence of bladder motion was negligible within the timescale of the deformations considered. Simulating changes in prostate shape due to bladder filling might however be useful, particularly for lengthy procedures such as HIFU ablation.

This work has adopted a constrained optimisation scheme that uses the diameter of the TRUS balloon to reduce the registration search space. Similarly, if the position and orientation of the TRUS probe can be estimated during a procedure – for example, by using a spatial tracking device – these measurements could also be used as a constraint, which may help in achieving real-time registration.

6.4 Experiments and Results for MR-TRUS Registration

6.4.1 Data

6.4.1.1 Image Acquisition

Like previously described experiments, all patient data used in this thesis was obtained from patients recruited to clinical research studies carried out at University College London Hospital. These studies were approved by the local research ethics committee, and all patients gave informed, written consent to participate. In this case, data from 8 patients with prostate cancer were used to validate the MR-TRUS registration method.

T2-weighted MR images were acquired on all the patients using a Siemens 1.5T MR scanner and a pelvic phased-array coil with the patients in the supine position. The 3D MR volumes had an in-plane resolution of between 0.3 and 0.4 mm/pixel with a slice thickness of 3.0-3.3 mm. MR

scans were performed prior to template-guided, transperineal needle biopsy procedures (seven patients) or, for one case, a HIFU ablation as a treatment for localised prostate cancer.

All procedures were performed under general anaesthesia and 3D TRUS images of the gland were acquired at the beginning of the procedure with the patient placed in the lithotomy position. The acquisition of these TRUS images is described in Section 6.3.1.

6.4.1.2 Data Processing

Following manual segmentation of the MR images and FE mesh generation, as outlined in Section 3.2.1.2, 500 biomechanical simulations were performed for each case using a nonlinear FE solver, described in Section 3.2 and Section 6.2.1.

The deformed FE models resulting from these simulations were then used to build a patient-specific MR-derived SMM for each case, as described in Section 3.3.1.2. The number of modes used in each SMM was determined by finding the value of L (see Eq. 3.3) that resulted in at least 99% of the variance in the training data being described by the model. For the purposes of registration, a high-density, triangulated surface mesh was also created for each SMM.

Each set of TRUS images was reconstructed into a volume with an isotropic voxel dimension of 1mm. An implementation of the sheetness filter (see Section 4.2.1.1) was coded using MATLAB. In this algorithm, the Hessian was computed using a frequency domain approach based on the fast Fourier transform.

6.4.2 Experiment and Result

The mean ± SD generalisation ability, defined in Section 5.2.2.2 and calculated over all SMMs generated for 8 patient datasets, was 0.30 ± 0.09 mm. This low value indicates that a linear SMM was able to capture the simulated prostate motion predicted by the FE model adopted in this thesis.

A summary of the initial and final landmark-based TREs for each patient case is given in Table 6.5. The initial TREs were calculated following initialisation by rigid alignment of the apex-base axes, as described in Section 4.2.3. Histograms of the initial and final RMS TREs are shown in Figure 6.11; a summary of the numerical TREs for each case is given in Table 6.5.

Case No.	*L*	No. of Landmarks	Initial RMS TRE (mm)		Final RMS TRE (mm) (Rigid)		Final RMS TRE (mm) (Deformable)		Deformation (RMS AND) (mm)		LLE mean ± SD (mm)	
			Median	95% CL	Median	95% CL	Median	95% CL	Rigid	Non-rigid	MR	Ultrasound
1	13	5	9.42	11.39	9.47	12.13	2.68	7.21	8.23	3.04	1.53±1.23	1.90±2.17
2	11	3	14.52	17.43	4.47	7.73	3.19	9.62	12.54	0.68	1.02±0.75	1.62±1.99
3	11	3	6.29	9.62	3.14	6.09	1.69	5.38	6.00	1.73	2.99±1.21	1.25±0.43
4	11	4	6.24	9.42	3.20	6.27	1.56	5.21	6.56	1.83	3.15±1.96	1.84±1.93
5	10	5	9.32	11.14	9.54	12.33	2.60	6.84	3.29	2.96	4.63±2.94	1.89±2.36
6	12	3	5.86	8.75	2.81	5.22	1.58	4.65	4.41	2.44	1.94±1.35	1.39±0.99
7	11	4	8.84	11.65	10.38	13.72	2.92	7.49	4.01	2.84	1.20±0.63	1.16±0.68
8	10	4	6.15	8.98	3.09	5.74	1.49	4.66	7.08	2.07	1.71±1.16	0.89±0.55
All	--	**31**	**8.13**	**15.02**	**5.11**	**12.05**	**2.40**	**6.19**	**7.32**	**2.19**	**2.35±1.92**	**1.53±1.52**

Table 6.5 TREs computed for registrations using the automatic rigid and deformable SMM-based method (Cases 1 to 7 were template-guided biopsies and Case 8 was a HIFU ablation) The LLE and contributions of the magnitude of the rigid and non-rigid components of the non-rigid transformation (expressed as AND – see text) resulting from the deformable registrations are also given for each case.

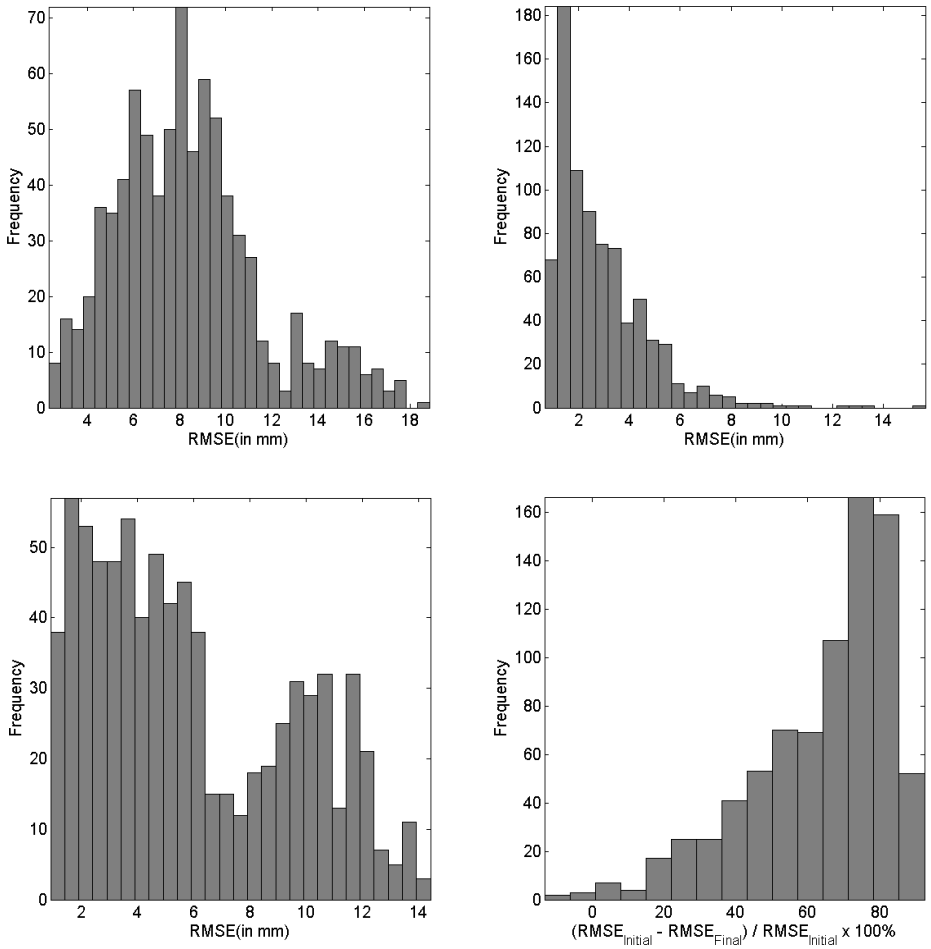

Figure 6.11 Histograms of the RMS TRE calculated before and after 800 registrations of MR-derived SMM and TRUS images (100 registrations per case). Top left: the initial TRE after manual rigid initialisation; Top right: the final TRE following registration using the automatic deformable SMM-based method; Bottom left: final TRE following automatic rigid registration of the SMM without allowing it to deform; Bottom right: relative change in TRE, expressed as a percentage reduction from initial to final TRE using the deformable registration method.

The overall median RMS TRE was 2.40 mm across the 8 patient cases using the deformable SMM-based method. The magnitudes of rigid and non-rigid components of the registration transformation were quantified by separately calculating the absolute node displacement (AND) for FE mesh nodes locations over the entire gland due to the rigid and shape transformations respectively. The results for each patient are also given in Table 6.5.

Inspection of Figure 6.11 and Table 6.5 reveals that a significant improvement in TRE was achieved by including the deformable component in the registrations, especially for cases 1, 5, and 7. Overall, the median RMS TRE was improved from 5.11 mm, obtained using rigid registration, to 2.40 mm, obtained using the proposed deformable registration scheme. This finding highlights the importance taking into account deformation between MR and TRUS imaging to achieve the highest accuracy.

The TREs computed for the surface-driven registration method are given in Tables 6.7 and 6.8. The median RMS TRE in this case was 5.4 mm. The result for this method compares with a mean TRE of 3.06 ± 1.41 for MR-to-TRUS registration of a phantom prostate reported by Narayanan et al. (2009). Comparing with the SMM-based method, although the surface fit was relatively good – the RMS point-to-surface distance ranged from 0.52 to 0.71mm – the TRE was approximately 45% higher than the SMM-based method. It is also important to note that this method requires segmentation of the target TRUS surface and is dependent on the accuracy of this segmentation. In contrast, segmentation of the capsule in TRUS images is not required by the automatic model-to-image technique proposed in this thesis.

Furthermore, inspection of the LLEs given in Tables 6.5 and 6.6 reveals no obvious relationship between these two measures, but the LLE was found to be larger for MR images compared with TRUS images. This may be attributed to the lower resolution of the MR images, particularly between slices, which introduces greater uncertainty in localising landmarks.

Landmark	No. of Landmarks	Initial RMS TRE (mm)		Final RMS TRE (mm)		LLE mean ± SD (mm)	
		Median	95% CL	Median	95% CL	MR	TRUS
Apex	8	9.88	11.80	3.62	6.09	2.12±1.83	2.72±2.00
Base	8	10.52	12.77	3.14	6.59	2.13±0.98	1.27±0.96
JGSV*	8	7.77	10.35	3.01	5.49	2.69±1.93	1.59±1.38
Cysts/Calcifications	7	5.83	7.22	1.92	3.74	2.49±2.97	0.39±0.25

* JGSV denotes the junction between the gland and the seminal vesicles as described in Section 5.4.1.

Table 6.6 TREs and LLEs calculated for registrations using the automatic SMM-based method, grouped according to the type of landmark.

Case No.	Final RMS TRE (mm)		MR-TRUS Surface distance (mm)
	Median	95% CL	RMS
1	3.62	4.33	0.68
2	2.25	4.27	0.57
3	5.71	7.04	0.59
4	5.76	7.50	0.71
5	10.03	10.55	0.61
6	8.44	9.33	0.53
7	3.48	4.59	0.52
8	6.51	8.67	0.57
All	5.45	9.95	0.60

Table 6.7 TREs and LLEs calculated for surface-driven registrations.

Landmark	Final RMS TRE (mm)	
	Median	95% CL
Apex	5.72	7.55
Base	6.68	7.62
JGSV	4.59	5.81
Cysts / Calcifications	7.77	9.22

Table 6.8 TREs calculated for surface-driven registrations, grouped according to the type of landmark.

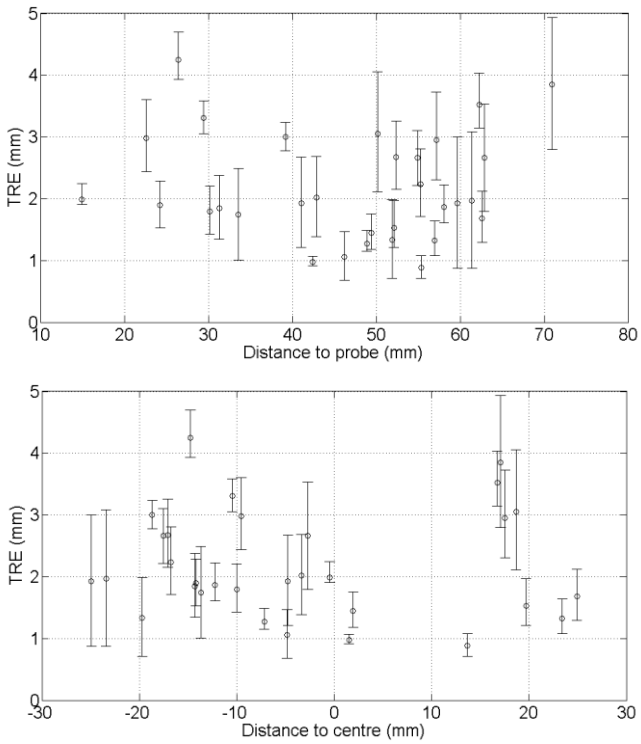

Figure 6.12 Plots of the spatial distribution of TRE: Left, the TRE is plotted against the perpendicular distance from the TRUS probe axis in the anterior-posterior direction; right, the TRE is plotted against the perpendicular distance from the mid-gland transverse plane (positive distances are near to the apex and negative distances are near to the base). In both cases, the errors are plotted as a median (circle) of 100 registration trials for 8 patients. The error bars indicate the 5th and 95th percentiles.

The spatial distribution of the registration error has important implications for the clinical application of MR-TRUS registration, since the peripheral zone of the prostate gland is known to be the most common site harbouring cancer (McNeal, et al., 1988). To investigate the spatial distribution of the TREs within the prostate, the TREs were plotted i) versus the perpendicular distance from the TRUS probe axis in anterior-posterior direction, and ii) versus the perpendicular distance from the mid-gland transverse plane. The results, shown in Figure 6.12, reveal no obvious relationship between the TRE and the distance from the probe axis, suggesting that the errors independent of spatial location. However, inspection of the second plot in Figure 6.12 indicates that the TRE was found to be significantly larger near to the apex of the gland. This observation may be attributed to the difficulty associated with accurately segmenting the prostate in the transverse MR slices at the ends of the gland, and in identifying the apex landmark point in the TRUS images, as suggested by the relatively high LLE computed for this landmark (see Table 6.5). Figure 6.13 illustrates the results of warping MR and target TRUS images using the DDF computed from two example registrations.

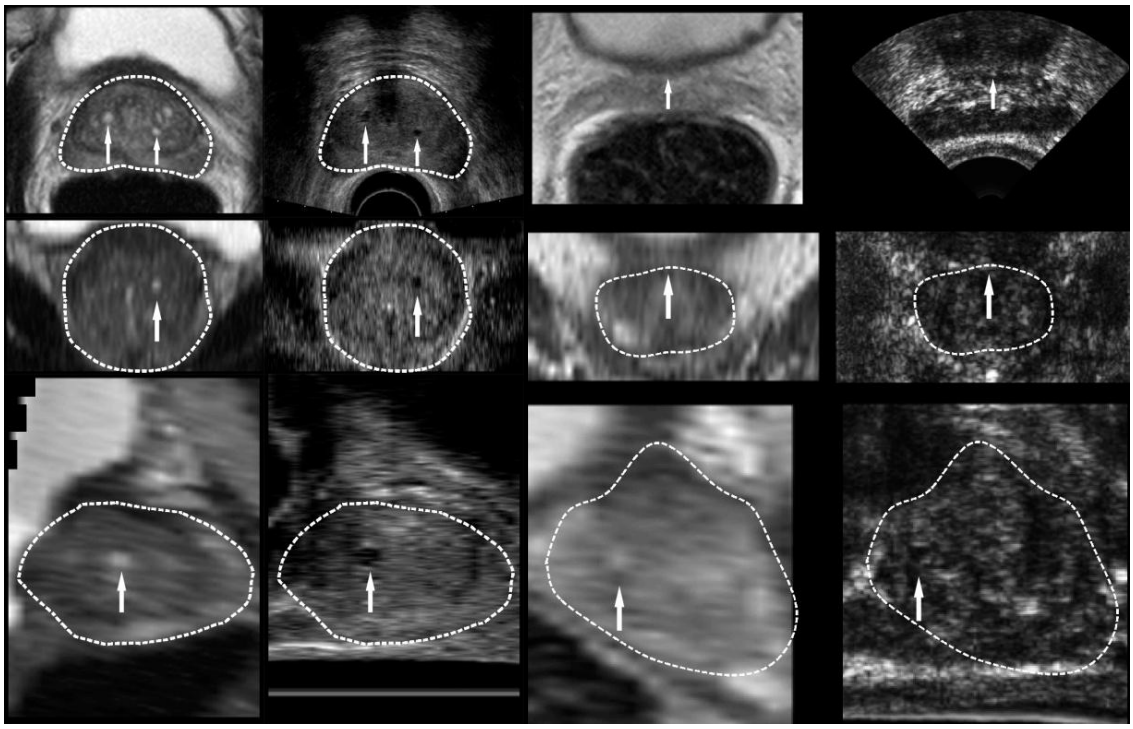

Figure 6.13 Examples of transverse (top row), coronal (middle row) and sagittal (bottom row) views through registered MR (left column) and TRUS (right column) volumes for Case 1 (left; biopsy case) and Case 8 (right; HIFU case). The MR volume has been warped using the dense displacement field calculated from the FE model. The arrows indicate landmarks which were well aligned following registration.

Following the discussion in Section 5.4.2, the TRE may be converted to a more clinically useful interpretation. For example, if a tumour hit-rate of 90% is set, the corresponding RMS TRE threshold is 3.41mm (see Section 5.4.2 and Figure 6.14). Figure 6.15 shows a graph of the percentage of the registrations performed in the experiments meeting a particular hit-rate for detecting a 0.5cc prostate tumour as a function of the hit-rate. Using this 90% hit-rate threshold, it is observed that over 93% of the registrations performed in this thesis met this criterion.

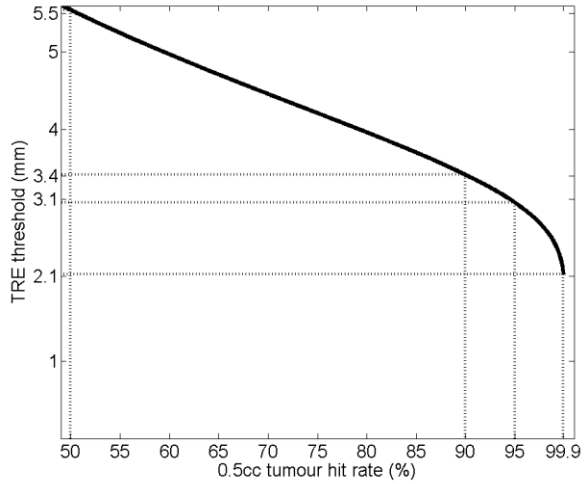

Figure 6.14 Plot shows the TRE threshold as a function of the hit-rate.

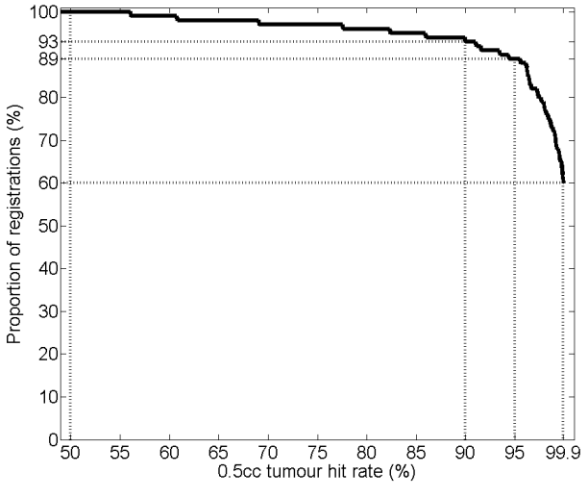

Figure 6.15 Plot shows a graph of the percentage of registrations meeting a particular hit-rate for detecting a 0.5cc prostate tumour as a function of the hit-rate.

6.4.3 Discussion

The potential for misclassification of clinically significant prostate cancer is a major problem with conventional transrectal biopsy schemes, and 5mm-grid-based saturation schemes have been

proposed to improve the detection of significant disease that would otherwise be missed by conventional methods (Epstein et al., 2005; Scattoni et al., 2007). MR-targeted biopsy offers an alternative approach with the potential benefit that the number of biopsy samples required to establish an accurate diagnosis is much lower than saturation schemes. The practical level of targeting accuracy necessary to make this approach clinically useful is as yet unknown and will depend on the tumour localisation accuracy of the MR imaging technique employed.

An important practical feature of the proposed method is the simple two-point initialisation which provides the initial rigid-body transformation (described in Section 4.2.3). This step can be carried out quickly and easily in the clinical setting. The registration method was found to be robust to different starting positions, simulated by adding a random error to two manually-defined starting points. However, it should be borne in mind that using a fixed level of error in this way for all cases does not result in equivalent initial TREs due to different sizes of prostate gland which means that the effect of introducing a random initialisation error on the initial TRE was greater for smaller glands than for larger glands.

Another important development in the aspect of validation analysis (see Section 5.4.2) is the chance that a targeting system hit the target. This is related to the traditional TRE adopted by the image registration community. This calculation provides a crude estimate of system performance in a clinical context. However, in practice, tumours are neither spherical nor homogeneous, and additional sources of errors will be present. How the performance of an MR-targeted biopsy system compares with conventional and saturation schemes under realistic conditions, together with the accuracy required to achieve disease control from ablative interventions, are beyond the scope of this thesis and are topics for future investigation.

Chapter 7 Conclusion and Future Work

7.1 Contributions of this Thesis

7.1.1 Primary Contributions

Three main contributions are summarised in this thesis:

Firstly, a framework for constructing combined statistical-biomechanical models has been developed and described in Chapter 3, which includes motion variance and variance in tissue mechanical properties. This framework can in principle be applied to other organs. Two models, derived from TRUS and MR images, have been described to constrain the prostate gland motion using anatomical information obtained from medical images. The performance of the models based on simplified geometric information – which could greatly reduce the effort required to construct the models – has been investigated and validated.

Secondly, a normal-vector-based registration algorithm has been proposed that allows efficient estimation of registration parameters, based on a probabilistic formulation of a mixture of joint spatial and directional data to align two vector-valued features, and solved by an adapted EM algorithm. This is implemented using a novel model-to-image registration approach and is described in Chapter 4.

Thirdly, the two techniques highlighted above have been applied successfully to register MR and TRUS images, acquired on patients undergoing biopsy and therapy, and a rigorous analysis of registration accuracy has been performed and presented in Chapters 5 and 6. At the time of submitting this thesis, registration software incorporating the innovations described above has been used to provide guidance for over 100 prostate biopsy and therapy procedures carried out as part of clinical studies at University College London Hospital.

7.1.2 Supplementary Contributions

During the work on the above contributions, some additional contributions have emerged: A clinically relevant error analysis has been reported to analyze the registrations based on a derivation of the distribution of “target hits” from the TRE (in Section 5.4.2); second, as part of the work described in Chapter 4, a new image noise model was developed for image registration (in Section 4.2.2.1), which lays the foundation of the main contribution above; and finally, an

analytical solution of the EM algorithm for a mixture of joint Gaussian and Watson distributions is described in Section 4.2.2.4.

7.2 Future Work

7.2.1 Motion Modelling

7.2.1.1 Organ Segmentation

A significant limitation of the model-to-image approach adopted here is the prerequisite for a geometric anatomical model of the organs of interest. Preoperative anatomical models which incorporate a surgical plan are widely used in many other image-guided interventions, such as orthopaedic surgery, since they provide an intuitive and easy-to-interpret representation of anatomy and treatment strategy. In the work presented in this thesis, a patient-specific FE model based on a segmented MR image was chosen. Once an FE model is obtained, processing to predict deformation is a relatively straightforward task, which can be performed automatically, with little or no user-interaction. However, it is clear that the generation of a model of this kind adds significant time and complexity to the clinical workflow. In the present application, this task is not time-critical since it can be performed at any time between MR imaging and a procedure, which in practice is usually a period of days to weeks. From a clinical workflow perspective, the most significant part of the model generation is the segmentation of the MR image, especially if manual segmentation is employed, as in this thesis (the FE mesh generation, the FEA simulations, and the TRUS-/MR-SMM generation processes are computationally intensive, but completely automatic). Manual segmentation arguably provides the most accurate data for FE model building and FEA, but requires significant anatomical knowledge, user-interaction and is time-consuming. Consequently, manual MR segmentation may be difficult to justify in some centres, although it is envisaged that such a procedure could be accepted, for instance, as part of a high-accuracy treatment planning protocol for patients undergoing targeted therapy for localised prostate cancer, particularly in a clinical research setting. Nevertheless, alternative, semi- or fully-automatic techniques are highly desirable.

Based on the present experience, the majority of the segmentation time is required to segment the pelvic bone, which has a complex geometry compared with that of the prostate. The simplified version of the MR-derived SMM has been compared with the original models and showed no significant difference, and hence that accurate segmentation of the pelvis is not

required. Compared with pelvis segmentation, segmenting the prostate alone is much less complicated and less time-consuming when performed manually. Nevertheless, this task would benefit from automatic segmentation, for example using the method described by Klein et al. (Klein et al. 2008). I am currently being involved in investigating statistical motion modelling techniques similar to those employed in this thesis to create generic, population-based models of the prostate gland, which could be used to automatically segment MR images using an adaptation of the model-to-image registration algorithm (see Section 7.2.1.3 below).

7.2.1.2 Computational Expense for Biomechanical Simulations

The computational burden of FEA simulations was reduced significantly by employing a parallelised, GPU-based implementation of the FEA solver, which meant that a single FE simulation could be performed within 20 seconds. To the best of my knowledge, this work is the first to report an image registration method that integrates the high-speed, GPU-based FE modelling with statistical shape modelling techniques to efficiently generate a physically-constrained deformable organ model for registration during image-guided intervention applications. The use of a physically-constrained model has considerable advantages over alternative methods as it leads to a registration that is robust to noise in the target image, but flexible enough to permit significant deformation.

7.2.1.3 Population-based Generic Modelling Approach

Progress has been made on the topic of a generic population based modelling (Hu et al. 2011b) for addressing both the segmentation and computational issues. The basic idea is first to build a population-based generic motion model to describe both variance due to subject difference and variance due to individual motion; then, given limited patient specific information (for example in the form of a few simple measurements, such as pelvic size and apex-to-base distance), to extract subject (or patient)-specific motion model from the generic model; and finally, to constrain the transformation using this 'fitted' model in the registration task.

In a published study, the feasibility of using a multilinear statistical shape model (MSSM) to predict patient-specific prostate gland motion was investigated (Hu et al. 2011b). An MSSM was trained using synthesized shape data, generated by modelling gland motion using a nonlinear finite-element model of the prostate and surrounding anatomy, which was in turn derived from an MR image for each patient. Once generated, the MSSM was used to predict the prostate motion for a new patient given unseen information on gland shape and size, derived from an

MR image. A set of deformed gland shapes, predicted by this model, was then used as training data for a linear SMM for the new patient, constructed using principal component analysis, which approximates the shape variation expected during a TRUS-guided surgical procedure for this particular patient. This approach showed promise by computing the error when using the final patient-specific SMM to model biomechanically simulated gland deformations for 14 patient datasets.

7.2.1.4 Gland Motion Analysis and Modelling

In the FE simulations of gland deformation, for simplicity, changes in shape of the prostate gland that may occur due to a change in patient position between the MR and TRUS imaging sessions have not been explicitly accounted for. Hirose et al. (2002) comment that a change in gland shape due to the change from the supine to the lithotomy position may be an important factor in the changes observed in their study, but since supine MR images were acquired using an endorectal MR coil, whilst MR images with the patient in the lithotomy position were acquired with a rectal obturator in place, it is impossible to determine the contribution to the gland shape change of the change in patient position relative to the forces imposed by these devices.

In the present research, it is assumed that any shape change due to the change in patient position is effectively modelled by considering a significantly wider range of TRUS probe poses than would be encountered in practice in the FE simulations. In this way, changes in the relative orientation of the anal-rectal and prostate (apex-base) axes due to a change in patient position are accounted for since the former governs the angle of insertion of the TRUS probe in the lithotomy position.

However, since the contribution to the total prostate gland deformation of a change from the supine position to the lithotomy position has not been quantified, the assumption that the contribution is negligible is speculative and requires further verification. Such verification was outside the scope of the present studies and might be the subject of future work. Furthermore, there has been no evidence showing that this could not be extended to model other situations, such as the removal of an endorectal coil used in some MR imaging protocols, or freehand motion of an end-firing TRUS probe during transrectal biopsy.

7.2.2 Model-to-image Registration

Based on the retrospective study described in this thesis and limited ongoing *in vivo* experience, the registration requires a relatively high quality target feature (e.g. organ surface boundary). However, the localisation of manual surface points is highly user dependent and the automatic image features are highly image quality dependent. The former approach needs the clinician follows the protocol to define the surface points carefully and in a number of slices (as discussed in Section 4.2.1.1), which could be time-consuming and/or requires extensive extra training, while the latter relies on having no significant artefacts and relatively high signal-to-noise ratio, which is difficult to maintain in practice and lacks measurable standards, especially for ultrasound data since ultrasound is widely recognised as a relatively challenging modality from the point-of-view of image registration.

One of the advantages of formulating the probabilistic objective function as in Section 4.2.2 is that the algorithm can be adapted in a mathematically principled fashion. For instance, prior knowledge and explicit treatment of outliers in data can be included. The first can be formulated by extra pairs of corresponding points or other known correspondence. The use of such a prior knowledge has been demonstrated in a different application using vessel-based registration (Hu et al. 2010). The effect of outliers is included by different methods, uniform probability density function (Hu et al. 2010;Myronenko et al. 2010) and a slack variable with column-row normalisation procedure (Chui et al. 2002) and the presented work. Such a probabilistic formulation provides a measurable, tuneable and interpretable approach to include outliers explicitly, via the weighting parameter. This advance of the modelling should be included in the future development to address the above difficulties.

Another possible extension to this algorithm is to identify outliers in the error distribution (see e.g. Figure 6.11), indicating less accurate registrations by including a feed-back loop system, so the low quality registrations will raise an alarm to the user. It is, in general, a difficult problem as no ground truth could be made available during the procedures. But many global constraints may be useful. For example, a limit may be set for magnitude of translation and rotation, since large translation or rotation is not expected after initial alignment, e.g. using a pair of apex and base points described in Section 4.2.3.

From a more algorithmic point of view, the direct optimisation approach (in Section 4.2.1) is more general-purpose as different transformation models, similarity measures and/or

optimisers may be employed. However, the probabilistic approach (in Section 4.2.2) is more difficult to adapt because it requires a specific probability density function to describe the similarity between different model and image features. This can be more complex for other vector-valued features; it also requires an explicit transformation model for the feature vector, which, in general, is unknown or difficult to approximate. In contrast, the feature can be estimated based on the spatial transformation using any suitable numerical interpolation schemes in a direct optimisation approach. Nevertheless, the probabilistic approach is still worthwhile for a number of reasons besides the flexibility discussed above. In particular, the posterior probability in the EM algorithm (in Section 4.2.2.4) can be approximated by either truncated cluster density or hard assignment without losing accuracy, which directly results in an efficient implementation.

7.2.3 Validation

One potential limitation of the validation of this thesis is the small sample size. For instance, only data from five patients are recruited in the TRUS-to-TRUS registration study. To investigate the implications of this, a statistical power analysis was conducted on the conclusions drawn from the results. Using a two-sample, two-sided t-test with a significance level of 5%, and assuming a normally distributed error, the statistical power, 1-β (where β is the probability of type II error), was calculated for the hypotheses that the TRE corresponding to the registration based on SMM2 is lower than the TRE for any of the elastic or rigid registrations. The statistical power was >0.8 in all cases, suggesting that 5 patients provided adequate statistical power to detect the difference between the TRE of the proposed method and the alternatives.

Furthermore, if a clinical error threshold of 4.92mm is assumed, equal to the radius of a 0.5cm^3 sphere representing an idealised tumour of clinically significant volume, a more clinically meaningful criterion becomes: Is the TRE less than 4.92mm? The statistical power was computed for this case by testing whether the mean TRE is significantly less than 4.92 mm, this time using a one-sample, two-sided t-test with a significance level of 5%. In this case, 1-β was 1.0 for registrations based on SMM2, suggesting strong statistical power to support the hypothesis that the proposed method can achieve a clinically useful accuracy. In contrast, the statistical power corresponding to alternative methods was less than 0.6, indicating that 5 patients may be insufficient to conclude that alternative methods did or did not achieve a

clinical useful level of accuracy. Therefore, further investigation is required using more patient datasets to evaluate properly the clinical utility of these alternative registration techniques.

In conclusion, the accuracy reported in Chapter 6 is based on the assumptions that the data used in this thesis can well represent the population data, and the assumption of the normal distribution of the error. Both of these assumptions cannot be verified unless more data are used in the validation. As a future extension of the work conducted in this thesis, more data will be analysed to test and improve the modelling, registration and targeting approaches.

Reference

Aarnink, R. G., Beerlage, H. P., de la Rosette, J. J. M. C., Debruyne, F. M. J., & WIJKSTRA, H. E. S. S. 1998, "Transrectal ultrasound of the prostate: innovations and future applications", *The Journal of Urology*, vol. 159, no. 5, pp. 1568-1579.

Abi-Nahed, J., Jolly, M. P., & Yang, G. Z. 2006, "Robust Active Shape Models: A Robust, Generic and Simple Automatic Segmentation Tool," in *Medical Image Computing and Computer-Assisted Intervention - MICCAI 2006*, vol. 4191 pp. 1-8.

Ahmed, H. U. & Emberton, M. 2008, "Active surveillance and radical therapy in prostate cancer: can focal therapy offer the middle way?", *World J.Urol.*, vol. 26, no. 5, pp. 457-467.

Ahmed, H. U., Kirkham, A., Arya, M., Illing, R., Freeman, A., Allen, C., & Emberton, M. 2009, "Is it time to consider a role for MRI before prostate biopsy?", *Nat.Rev.Clin.Oncol.*, vol. 6, no. 4, pp. 197-206.

Ahmed, H. U., Pendse, D., Illing, R., Allen, C., van der Meulen, J. H., & Emberton, M. 2007, "Will focal therapy become a standard of care for men with localized prostate cancer?", *Nat.Clin.Pract.Oncol.*, vol. 4, no. 11, pp. 632-642.

Ahmed, H. U., Akin, O., Coleman, J. A., Crane, S., Emberton, M., Goldenberg, L., Hricak, H., Kattan, M. W., Kurhanewicz, J., Moore, C. M., Parker, C., Polascik, T. J., Scardino, P., van As, N., Villers, A., & on behalf of the Transatlantic Consensus Group on Active Surveillance and Focal Therapy for Prostate Cancer (appendix) 2012, "Transatlantic Consensus Group on active surveillance and focal therapy for prostate cancer", *BJU International*, vol. 109, no. 11, pp. 1636-1647.

Ahmed, H. U., Hu, Y., Carter, T., Arumainayagam, N., Lecornet, E., Freeman, A., Hawkes, D., Barratt, D. C., & Emberton, M. 2011, "Characterizing Clinically Significant Prostate Cancer Using Template Prostate Mapping Biopsy", *The Journal of Urology*, vol. 186, no. 2, pp. 458-464.

Alexander, D. C., Pierpaoli, C., Basser, P. J., & Gee, J. C. 2001, "Spatial transformations of diffusion tensor magnetic resonance images", *Medical Imaging, IEEE Transactions on*, vol. 20, no. 11, pp. 1131-1139.

Alexander, D. C. & Gee, J. C. 2000, "Elastic Matching of Diffusion Tensor Images", *Computer Vision and Image Understanding*, vol. 77, no. 2, pp. 233-250.

Alterovitz, R., Goldberg, K., Pouliot, J., Hsu, I. C., Kim, Y., Noworolski, S. M., & Kurhanewicz, J. 2006, "Registration of MR prostate images with biomechanical modeling and nonlinear parameter estimation", *Med Phys.*, vol. 33, no. 2, pp. 446-454.

Arindam, B., Inderjit, D., Joydeep, G., & Suvrit, S. "Generative model-based clustering of directional data", ACM, Washington, D.C., pp. 19-28.

Audette, M. A., Ferrie, F. P., & Peters, T. M. 2000, "An algorithmic overview of surface registration techniques for medical imaging", *Medical Image Analysis*, vol. 4, no. 3, pp. 201-217.

Aus, G. 2006, "Current status of HIFU and cryotherapy in prostate cancer--a review", *Eur.Urol.*, vol. 50, no. 5, pp. 927-934.

Ballester, M. A., Linguraru, M. G., Aguirre, M. R., & Ayache, N. "On the adequacy of principal factor analysis for the study of shape variability", 1 edn, F. Michael & M. R. Joseph, eds., SPIE, pp. 1392-1399.

Balmes, E., Bianchi, J. P., & Leclere, J. M. OpenFEM - A Matlab based Finite Element Toolbox. 2010.

Baowei, F., Corey, K., & David, L. W. 2003, "A comparative study of warping and rigid body registration for the prostate and pelvic MR volumes", *Computerized medical imaging and graphics : the official journal of the Computerized Medical Imaging Society*, vol. 27, no. 4, pp. 267-281.

Barratt, D. C., Chan, C. S. K., Edwards, P. J., Penney, G. P., Slomczykowski, M., Carter, T. J., & Hawkes, D. J. 2008, "Instantiation and registration of statistical shape models of the femur and pelvis using 3D ultrasound imaging", *Medical Image Analysis*, vol. 12, no. 3, pp. 358-374.

Barzell, W. E. & Melamed, M. R. 2007, "Appropriate Patient Selection in the Focal Treatment of Prostate Cancer: The Role of Transperineal 3-Dimensional Pathologic Mapping of the Prostate--A 4-Year Experience", *Urology*, vol. 70, no. 6, Supplement 1, p. S27-S35.

Baumann, M., Mozer, P., Daanen, V., & Troccaz, J. 2009, "Prostate Biopsy Assistance System with Gland Deformation Estimation for Enhanced Precision," in *Medical Image Computing and Computer-Assisted Intervention - MICCAI 2009*, LNCS 5761 edn, G. Z. Yang et al., eds., Springer Berlin / Heidelberg, pp. 67-74.

Besl, P. J. & McKay, H. D. 1992, "A method for registration of 3-D shapes", *Ieee Transactions on Pattern Analysis and Machine Intelligence*, vol. 14, no. 2, pp. 239-256.

Bharatha, A., Hirose, M., Hata, N., Warfield, S. K., Ferrant, M., Zou, K. H., Suarez-Santana, E., Ruiz-Alzola, J., D'Amico, A., Cormack, R. A., Kikinis, R., Jolesz, F. A., & Tempany, C. M. 2001, "Evaluation of three-dimensional finite element-based deformable registration of pre- and intraoperative prostate imaging", *Med Phys.*, vol. 28, no. 12, pp. 2551-2560.

Bilmes, J. <[05] Pub Date>, "A Gentle Tutorial on the EM Algorithm and its Application to Parameter Estimation for Gaussian Mixture and Hidden Markov Models".

Bishop, C. M. 2006, "Mixture Model and EM," in *Pattern Recognition and Machine Learning*, Springer, pp. 423-455.

Boncelet, C. 2005, "Image Noise Models," in *Handbook of Image and Video Processing*, A.C.Bovik et al, ed., Academic Press, pp. 397-409.

Bonet, J. & Burton, A. J. 1998, "A simple average nodal pressure tetrahedral element for incompressible and nearly incompressible dynamic explicit applications", *Communications in Numerical Methods in Engineering*, vol. 14, no. 5, pp. 437-449.

Bookstein, F. L. 1989, "Principal warps: thin-plate splines and the decomposition of deformations", *Pattern.Analysis.and Machine.Intelligence., IEEE Transactions.on*, vol. 11, no. 6, pp. 567-585.

Braeckman, J., Autier, P., Garbar, C., Marichal, M. P., Soviany, C., Nir, R., Nir, D., Michielsen, D., Bleiberg, H., Egevad, L., & Emberton, M. 2008, "Computer-aided ultrasonography (HistoScanning): a novel technology for locating and characterizing prostate cancer", *BJU.Int.*, vol. 101, no. 3, pp. 293-298.

Broit, C. 1981, *Optimal Registration of Deformed Images,* University of Pennsylvania.

Byrne, T. E. 2005, "A review of prostate motion with considerations for the treatment of prostate cancer", *Med.Dosim.*, vol. 30, no. 3, pp. 155-161.

Cachier, P., Bardinet, E., Dormont, D., Pennec, X., & Ayache, N. 2002, "Iconic feature based nonrigid registration: the PASHA algorithm", *Computer.Vision and Image Understanding.*, vol. 89, no. 2-3, pp. 272-298.

Cachier, P., Mangin, J. F., Pennec, X., Riviere, D., Papadopoulos-Orfanos, D., Regis, J., & Ayache, N. 2001, "Multisubject Non-rigid Registration of Brain MRI Using Intensity and Geometric Features," in *Medical Image Computing and Computer-Assisted Intervention MICCAI 2001*, 2208 edn, W. Niessen & M. Viergever, eds., Springer Berlin / Heidelberg, pp. 734-742.

Cahill, N., Noble, J., & Hawkes, D. 2009, "A Demons Algorithm for Image Registration with Locally Adaptive Regularization," pp. 574-581.

Canny, J. 1986, "A computational approach to edge detection", *IEEE Trans.Pattern Analysis and Machine Inteligence*, vol. 8, pp. 679-714.

Carter, T., Tanner, C., Beechey-Newman, N., Barratt, D., & Hawkes, D. 2008, "MR navigated breast surgery: method and initial clinical experience", *MICCAI 2008*, vol. 11, no. Pt 2, pp. 356-363.

Carter, T. J., Sermesant, M., Cash, D. M., Barratt, D. C., Tanner, C., & Hawkes, D. J. 2005, "Application of soft tissue modelling to image-guided surgery", *Med Eng Phys.*, vol. 27, no. 10, pp. 893-909.

CGAL. Computational Geometry Algorithms Library. 2009.

Chi, Y., Liang, J., & Yan, D. 2006, "A material sensitivity study on the accuracy of deformable organ registration using linear biomechanical models", *Medical Physics*, vol. 33, no. 2, pp. 421-433.

Christensen, G. E., Rabbitt, R. D., & Miller, M. I. 1996, "Deformable templates using large deformation kinematics", *Image Processing, IEEE Transactions.on*, vol. 5, no. 10, pp. 1435-1447.

Chui, H. & Rangaramjan, A. "A Feature Registration Framework using Mixture Models", in *IEEE Workshop on Mathematical Methods in Biomedical Image Analysis*, pp. 190-197.

Chui, H. & Rangarajan, A. 2002, "A new point matching algorithm for non-rigid registration", *Computer Vision and Image Understanding*, vol. 89, no. 2-3, pp. 114-141.

Cochlin, D., Dubbins, P., Goldberg, B., & Halpern, E. 2010, *Urogenital ultrasound - a text atlas, second edition* Taylor & Francis, London.

Cootes, T., Hill, A., Taylor, C., & Haslam, J. 1993, "The use of active shape models for locating structures in medical images," pp. 33-47.

Cootes, T. F., Taylor, C. J., Cooper, D. H., & Graham, J. 1995, "Active Shape Models - Their Training and Application", *Computer Vision and Image Understanding*, vol. 61, no. 1, pp. 38-59.

Cosio, F. A. 2008, "Automatic initialization of an active shape model of the prostate", *Med.Image Anal.*, vol. 12, no. 4, pp. 469-483.

Crouch, J. R., Pizer, S. M., Chaney, E. L., Hu, Y. C., Mageras, G. S., & Zaider, M. 2007, "Automated finite-element analysis for deformable registration of prostate images", *IEEE Trans.Med.Imaging*, vol. 26, no. 10, pp. 1379-1390.

Crum, W. R., Griffin, L. D., Hill, D. L. G., & Hawkes, D. J. 2003, "Zen and the art of medical image registration: correspondence, homology, and quality", *NeuroImage*, vol. 20, no. 3, pp. 1425-1437.

Crum, W. R., Camara, O., Rueckert, D., Bhatia, K. K., Jenkinson, M., & Hill, D. L. G. 2005, "Generalised Overlap Measures for Assessment of Pairwise and Groupwise Image Registration and Segmentation," in *MEDICAL IMAGE COMPUTING AND COMPUTER-ASSISTED INTERVENTION – MICCAI 2005*, 3749 edn, pp. 99-106.

Dam, E. B., Fletcher, P. T., & Pizer, S. M. 2008, "Automatic shape model building based on principal geodesic analysis bootstrapping", *Med.Image Anal.*, vol. 12, no. 2, pp. 136-151.

Davatzikos, C., Shen, D., Mohamed, A., & Kyriacou, S. K. 2001, "A framework for predictive modeling of anatomical deformations", *IEEE Trans.Med.Imaging*, vol. 20, no. 8, pp. 836-843.

Davis, M. H., Khotanzad, A., Flamig, D. P., & Harms, S. E. 1997, "A physics-based coordinate transformation for 3-D image matching", *Medical Imaging, IEEE Transactions on*, vol. 16, no. 3, pp. 317-328.

Dempster, A. P., Laird, N. M., & Rubin, D. B. 1977, "Maximum Likelihood from Incomplete Data Via Em Algorithm", *Journal of the Royal Statistical Society Series B-Methodological*, vol. 39, no. 1, pp. 1-38.

Denmeade, S. R. & Isaacs, J. T. 2002, "A history of prostate cancer treatment", *Nat Rev Cancer*, vol. 2, no. 5, pp. 389-396.

Descoteaux, M., Audette, M., & Chinzei, K. &. S. K. 2006, "Bone enhancement filtering: application to sinus bone segmentation and simulation of pituitary surgery", *Comput Aided Surg*, vol. 11, no. 5, pp. 247-255.

Dickinson, L., Hu, Y., Ahmed, H. U., Allen, C., Kirkham, A. P., Emberton, M., & Barratt, D. 2013, "Image-Directed, Tissue-Preserving Focal Therapy of Prostate Cancer: A Feasibility Study of a Novel Deformable MR-US Registration System", *BJU International, in press*.

Ding, M., Chiu, B., Gyacskov, I., Yuan, X., Drangova, M., Downey, D. B., & Fenster, A. 2007, "Fast prostate segmentation in 3D TRUS images based on continuity constraint using an autoregressive model", *Med.Phys.*, vol. 34, no. 11, pp. 4109-4125.

Djavan, B. & Margreiter, M. 2007, "Biopsy standards for detection of prostate cancer", *World J.Urol.*, vol. 25, no. 1, pp. 11-17.

du Bois, d. A., De, C. M., Haker, S., Weisenfeld, N., Tempany, C., Macq, B., & Warfield, K. 2004, "Improved Non-rigid Registration of Prostate MRI", *Med.Image Comput.Comput.Assist.Interv.MICCAI 2004.*, vol. 3216, pp. 845-852.

Eggener, S. E., Scardino, P. T., Carroll, P. R., Zelefsky, M. J., Sartor, O., Hricak, H., Wheeler, T. M., Fine, S. W., Trachtenberg, J., Rubin, M. A., Ohori, M., Kuroiwa, K., Rossignol, M., & Abenhaim, L. 2007, "Focal therapy for localized prostate cancer: a critical appraisal of rationale and modalities", *J.Urol.*, vol. 178, no. 6, pp. 2260-2267.

El-Hamalawi, A. 2001, "Mesh generation - application to finite elements", *Engineering Construction and Architectural Management*, vol. 8, no. 3, pp. 234-235.

Feldmar, J., Declerck, J., Malandain, G., & Ayache, N. 1997, "Extension of the ICP Algorithm to Nonrigid Intensity-Based Registration of 3D Volumes", *Computer Vision and Image Understanding*, vol. 66, no. 2, pp. 193-206.

Figueiredo, A. & Gomes, P. 2006, "Performance of the EM Algorithm on the Identification of a Mixture of Watson Distributions Defined on the Hypersphere", *Statistical Journal*, vol. 4, no. 2, pp. 111-130.

Fitzpatrick, J. M., West, J. B., & Maurer, C. R., Jr. 1998, "Predicting error in rigid-body point-based registration", *IEEE Trans.Med.Imaging*, vol. 17, no. 5, pp. 694-702.

Frangi, A., Niessen, W., Vincken, K., & Viergever, M. 1998, "Multiscale vessel enhancement filtering," in *Medical Image Computing and Computer-Assisted Intervention - MICCAI '98*, LNCS 1496 edn, pp. 130-137.

Futterer, J. J. 2007, "MR imaging in local staging of prostate cancer", *Eur.J.Radiol.*, vol. 63, no. 3, pp. 328-334.

Futterer, J. J., Scheenen, T. W., Heijmink, S. W., Huisman, H. J., Hulsbergen-van de Kaa CA, Witjes, J. A., Heerschap, A., & Barentsz, J. O. 2007, "Standardized threshold approach using three-dimensional proton magnetic resonance spectroscopic imaging in prostate cancer localization of the entire prostate", *Invest Radiol.*, vol. 42, no. 2, pp. 116-122.

General Register Office for Scotland 2010, *Deaths Time Series Data, Deaths in Scotland in 2010*, 2010 Deaths Time Series Data: Deaths in Scotland in 2010.

Giannopoulos, P. & Veltkamp, R. 2002, "A Pseudo-Metric for Weighted Point Sets," pp. 89-114.

Gold, S., Rangarajan, A., Lu, C. P., Pappu, S., & Mjolsness, E. 1998, "New algorithms for 2D and 3D point matching: pose estimation and correspondence", *Pattern Recognition*, vol. 31, no. 8, pp. 1019-1031.

Golub, G. H. & Van Loan, C. F. 1996, *Matrix Computation*, 3rd edn, The Johns Hopkins University Press, Baltimore, Maryland.

Gonzalez, R. C. & Woods, R. E. 2008, *Digital Image Processing - 3rd ed.* Pearson Prentice Hall, London.

Goshtasby, A. A. 2005, *2-D and 3-D Image Registration For Medical, Remote Sensing, and Industrial Applications* Wiley Blackwell.

Haber, E. & Modersitzki, J. 2006, "Intensity Gradient Based Registration and Fusion of Multi-modal Images," pp. 726-733.

Hajnal, J. V., Hill, D. L., & Hawkes, D. J. 2001, *Medical Image Registration* CRC Press.

Hajnal, J. V., Saeed, N., Soar, E. J., Oatridge, A., Young, I. R., & Bydder, G. M. 1995, "A Registration and Interpolation Procedure for Subvoxel Matching of Serially Acquired MR Images", *Journal of Computer Assisted Tomography*, vol. 19, no. 2, pp. 289-296.

Haker, S., Warfield, S. K., & Tempany, C. M. C. 2004, "Landmark-Guided Surface Matching and Volumetric Warping for Improved Prostate Biopsy Targeting and Guidance," in *Medical Image Computing and Computer-Assisted Intervention - MICCAI 2004*, LNCS 3216 edn, C. Barillot, D. R. Haynor, & P. Hellier, eds., Springer Berlin / Heidelberg, pp. 853-861.

Halpern, E. 2006, "The Prostate and Seminal Vesicles," in *Urogenital Ultrasound - A Text Atlas*, L. D. Cochlin et al., eds., Martin Dunitz Ltd., London, pp. 155-182.

Halpern, E. J., Cochlin, D. L., & Goldberg, B. B. 2002, *Imaging of the Prostate* Martin Dunits Ltd., London.

Halpern, E. J., Ramey, J. R., Strup, S. E., Frauscher, F., McCue, P., & Gomella, L. G. 2005, "Detection of prostate carcinoma with contrast-enhanced sonography using intermittent harmonic imaging", *Cancer*, vol. 104, no. 11, pp. 2373-2383.

Hambrock, T., Somford, D. M., Hoeks, C., Bouwense, S. A. W., Huisman, H., Yakar, D., van Oort, I. M., Witjes, J. A., Futterer, J. J., & Barentsz, J. O. 2010, "Magnetic Resonance Imaging Guided Prostate Biopsy in Men With Repeat Negative Biopsies and Increased Prostate Specific Antigen", *The Journal of Urology*, vol. 183, no. 2, pp. 520-528.

Haralick, R. M., Joo, H., Lee, C., Zhuang, X., Vaidya, V. G., & Kim, M. B. 1989, "Pose estimation from corresponding point data", *Systems., Man.and Cybernetics., IEEE Transactions.on*, vol. 19, no. 6, pp. 1426-1446.

Hawkes, D. J., Barratt, D., Blackall, J. M., Chan, C., Edwards, P. J., Rhode, K., Penney, G. P., McClelland, J., & Hill, D. L. 2005, "Tissue deformation and shape models in image-guided interventions: a discussion paper", *Med Image Anal.*, vol. 9, no. 2, pp. 163-175.

Hecht, F. FreeFEM. 2009.

Heidenreich, A., Aus, G., Bolla, M., Joniau, S., Matveev, V. B., Schmid, H. P., & Zattoni, F. 2008, "EAU Guidelines on Prostate Cancer", *European Urology*, vol. 53, no. 1, pp. 68-80.

Heimann, T. & Meinzer, H. P. 2009, "Statistical shape models for 3D medical image segmentation: a review", *Med.Image Anal.*, vol. 13, no. 4, pp. 543-563.

Hensel, J. M., Menard, C., Chung, P. W., Milosevic, M. F., Kirilova, A., Moseley, J. L., Haider, M. A., & Brock, K. K. 2007, "Development of multiorgan finite element-based prostate deformation model enabling registration of endorectal coil magnetic resonance imaging for radiotherapy planning", *Int.J.Radiat.Oncol.Biol.Phys.*, vol. 68, no. 5, pp. 1522-1528.

Hill, D. L. G. & Hawkes, D. J. "Voxel Similarity measures for automated image registration", pp. 205-216.

Hill, D. L. G., Batchelor, P. G., Holden, M., & Hawkes, D. J. 2001, "Medical image registration", *Physics in Medicine and Biology*, vol. 46, no. 3, pp. 1-45.

Hirose, M., Bharatha, A., Hata, N., Zou, K. H., Warfield, S. K., Cormack, R. A., D'Amico, A., Kikinis, R., Jolesz, F. A., & Tempany, C. M. 2002, "Quantitative MR imaging assessment of prostate gland deformation before and during MR imaging-guided brachytherapy", *Acad.Radiol.*, vol. 9, no. 8, pp. 906-912.

Ho-Le, K. 2001, "Finite element mesh generation methods: a review and classification", *Computer.-Aided Design.*, vol. 20, no. 1, pp. 27-38.

Hogg, R. V., McKean, J. W., & Craig, A. T. 2005, *Introduction to Mathematical Statistics*, 6th edn, Pearson Education, London.

Holden, M. 2008, "A Review of Geometric Transformations for Nonrigid Body Registration", *Medical Imaging, IEEE Transactions on*, vol. 27, no. 1, pp. 111-128.

Hu, Y., Carter, T., Ahmed, H., Emberton, M., Allen, C., Hawkes, D., & Barratt, D. 2011a, "Modelling Prostate Motion for Data Fusion during Image-guided Interventions", *Medical Imaging, IEEE Transactions on*, vol. 30, no. 11, pp. 1887-1900.

Hu, Y., Rijkhorst, E.-J., Manber, R., Hawkes, D., & Barratt, D. 2010, "Deformable vessel-based registration using landmark-guided coherent point drift," in *MIAR'10 Proceedings of the 5th international conference on Medical imaging and augmented reality*, vol. 6326 Springer, Beijing, pp. 60-69.

Hu, Y., Ahmed, H. U., Pendsé, D., Sahu, M., Allen, C., Emberton, M., & Hawkes, D. &. B. D. 2009, "MR to ultrasound image registration for guiding prostate biopsy and interventions," in *Medical*

Image Computing and Computer-Assisted Intervention - MICCAI 2009, LNCS 5761 edn, Springer, pp. 787-794.

Hu, Y., Ahmed, H. U., Taylor, Z., Allen, C., Emberton, M., Hawkes, D., & Barratt, D. 2012, "MR to ultrasound registration for image-guided prostate interventions", *Medical Image Analysis*, vol. 16, no. 3, pp. 687-703.

Hu, Y. & Barratt, D. "Learning Patient-specific Motion based on Decomposing a Multilinear Shape Model", in *2nd International Conference on Mathematical and Computational Biomedical Engineering*, pp. 237-240.

Hu, Y., Morgan, D., Ahmed, H., Pendsé, D., Sahu, M., Allen, C., Emberton, M., & Hawkes, D. &. B. D. 2008a, "Modelling Prostate Gland Motion for Image-guided Interventions," in *Biomedical Simulation*, LNCS 5104 edn, Springer, pp. 79-88.

Hu, Y., Morgan, D., Ahmed, H. U., Pendsé, D., Sahu, M., Allen, C., Emberton, M., & Hawkes, D. &. B. D. 2008b, "A Statistical Motion Model based on Biomechanical Simulations for Data Fusion during Image-guided Prostate Interventions," in *MICCAI 2008*, LNCS 5241 edn, Springer, pp. 737-744.

Huggins, C., Scott, W. W., & Heinen, J. H. 1942, "Chemical composition of human semen and of the secretions of the prostate and seminal vesicles", *Am J Physiol*, vol. 136, pp. 467-473.

Hyvarinen, A., Hurri, J., & Hoyer, P. O. 2009, "Independent Component Analysis," pp. 151-175.

Jeong, J.-Y., Ray, S., Han, Q., Liu, X., Muller, E. K., & Pizer, S. M. 2008, "Goodness of Prediction for Principal Components of Shape", *International Journal of Computer Vision*.

Jian, B. & Vemuri, B. C. 2005, "A Robust Algorithm for Point Set Registration Using Mixture of Gaussians", *Proc.IEEE Int.Conf.Comput.Vis.*, vol. 2, pp. 1246-1251.

John, M. S., Michael, G. H., Jon, J. K., & Thomas, M. P. 2005, "Prostate position relative to pelvic bony anatomy based on intraprostatic gold markers and electronic portal imaging", *International journal of radiation oncology, biology, physics*, vol. 63, no. 3, pp. 800-811.

Joldes, G. R., Wittek, A., & Miller, K. 2009, "Non-locking tetrahedral finite element for surgical simulation", *Communications in Numerical Methods in Engineering*, vol. 25, no. 7, pp. 827-836.

Joldes, G. R., Wittek, A., Warfield, S. K., & Miller, K. 2012, "Performing Brain Image Warping Using the Deformation Field Predicted by a Biomechanical Model Computational Biomechanics for Medicine," P. M. F. Nielsen, A. Wittek, & K. Miller, eds., Springer New York, pp. 89-96.

Jolliffe, I. T. 2002, *Principal Component Analysis*, second edn, Springer-Velag, New York.

Kaplan, I., Oldenburg, N. E., Meskell, P., Blake, M., Church, P., & Holupka, E. J. 2002, "Real time MRI-ultrasound image guided stereotactic prostate biopsy", *Magn Reson.Imaging*, vol. 20, no. 3, pp. 295-299.

Kirkham, A. P., Emberton, M., & Allen, C. 2006, "How good is MRI at detecting and characterising cancer within the prostate?", *Eur.Urol.*, vol. 50, no. 6, pp. 1163-1174.

Klein, S., van der Heide, U. A., Lips, I. M., van, V. M., Staring, M., & Pluim, J. P. 2008, "Automatic segmentation of the prostate in 3D MR images by atlas matching using localized mutual information", *Med.Phys.*, vol. 35, no. 4, pp. 1407-1417.

Klotz, L. 2005, "Active Surveillance for Prostate Cancer: For Whom?", *Journal of Clinical Oncology*, vol. 23, no. 32, pp. 8165-8169.

Krouskop, T. A., Wheeler, T. M., Kallel, F., Garra, B. S., & Hall, T. 1998, "Elastic moduli of breast and prostate tissues under compression", *Ultrasonic imaging*, vol. 20, no. 4, pp. 260-274.

Lemieux, L., Jagoe, R., Fish, D. R., Kitchen, N. D., & Thomas, D. G. T. 1994, "A patient-to-computed-tomography image registration method based on digitally reconstructed radiographs", *Medical Physics*, vol. 21, no. 11, pp. 1749-1760.

Loch, A., Bannowsky, A., Baeurle, L., Grabski, B., Konig, B., Flier, G., Schmitz-Krause, O., Paul, U., & Loch, T. 2007, "Technical and anatomical essentials for transrectal ultrasound of the prostate", *World Journal of Urology*, vol. 25, no. 4, pp. 361-366.

Lorenz, C., Carlsen, I., Buzug, T., Fassnacht, C., & Weese, J. 1997, "Multi-scale line segmentation with automatic estimation of width, contrast and tangential direction in 2D and 3D medical images," pp. 233-242.

Luo, B. & Hancock, E. R. 2001, "Structural graph matching using the EM algorithm and singular value decomposition", *Pattern Analysis and Machine Intelligence., IEEE Transactions on*, vol. 23, no. 10, pp. 1120-1136.

Luo, B. & Hancock, E. R. 2003, "A unified framework for alignment and correspondence", *Computer Vision and Image Understanding*, vol. 92, no. 1, pp. 26-55.

Maes, F., Collignon, A., Vandermeulen, D., Marchal, G., & Suetens, P. 1997, "Multimodality image registration by maximization of mutual information", *Medical Imaging, IEEE Transactions on*, vol. 16, no. 2, pp. 187-198.

Maintz, J. B. A. & Viergever, M. A. 1998, "A survey of medical image registration", *Medical Image Analysis*, vol. 2, no. 1, pp. 1-36.

Makni, N., Puech, P., Lopes, R., Dewalle, A. S., Colot, O., & Betrouni, N. 2009, "Combining a deformable model and a probabilistic framework for an automatic 3D segmentation of prostate on MRI", *Int.J.Comput.Assist.Radiol.Surg.*, vol. 4, no. 2, pp. 181-188.

Marberger, M., Carroll, P. R., Zelefsky, M. J., Coleman, J. A., Hricak, H., Scardino, P. T., & Abenhaim, L. L. 2008, "New treatments for localized prostate cancer", *Urology*, vol. 72, no. 6 Suppl, pp. 36-43.

Marsland, S., Twining, C. J., & Taylor, C. J. 2008, "A minimum description length objective function for groupwise non-rigid image registration", *Image and Vision Computing*, vol. 26, no. 3, pp. 333-346.

Martin, S., Baumann, M., Daanen, V., & Troccaz, J. 2010, "MR prior based automatic segmentation of the prostate in TRUS images for MR/TRUS data fusion," in *IEEE International Symposium on Biomedical Imaging,* IEEE, Rotterdam, Netherlands, pp. 640-643.

Maurer, C. R., Jr., Aboutanos, G. B., Dawant, B. M., Maciunas, R. J., & Fitzpatrick, J. M. 1996, "Registration of 3-D images using weighted geometrical features", *Medical.Imaging, IEEE Transactions.on*, vol. 15, no. 6, pp. 836-849.

McNeal, J. E., Redwine, E. A., Freiha, F. S., & Stamey, T. A. 1988, "Zonal Distribution of Prostatic Adenocarcinoma: Correlation with Histologic Pattern and Direction of Spread", *The American Journal of Surgical Pathology*, vol. 12, no. 12, pp. 897-906.

Melbourne, A., Ridgway, G., & Hawkes, D. J. "Image similarity metrics in image registration", B. M. Dawant & D. R. Haynor, eds., SPIE, San Diego, California, USA, pp. 762335-1-10.

Modat, M., Taylor Z.A., R. G. R., Barnes, J., Wild, E. J., Hawkes, D. J., Fox, N. C., & Ourselin, S. "Nonlinear elastic spline registration: evaluation with longitudinal huntington's disease data", in *WBIR 2010*, B. Fischer, B. Dawant, & C. Lorenz, eds., Springer-Verlag, Berlin Heidelerg, pp. 128-139.

Mohamed, A., Davatzikos, C., & Taylor, R. 2002, "A Combined Statistical and Biomechanical Model for Estimation of Intra-operative Prostate Deformation," in *Medical Image Computing and Computer-Assisted Intervention – MICCAI 2002*, LNCS 2489 edn, pp. 452-460.

Moradi, M., Abolmaesumi, P., Siemens, R., Sauerbrei, E., Boag, A., & Mousavi, P. 2009, "Augmenting Detection of Prostate Cancer in Transrectal Ultrasound Images Using SVM and RF Time Series", *IEEE Trans.Biomed.Eng*, vol. 56, no. 9, pp. 2214-2224.

Myronenko, A. & Song, X. 2010, "Point Set Registration: Coherent Point Drift", *IEEE Transactions.on Pattern.Analysis.and Machine.Intelligence.*, vol. 32, no. 12, pp. 2262-2275.

Myronenko, A., Song, X., & Carreira-Perpinan, M. A. "Non-rigid point set registration: Coherent Point Drift", MIT Press.

Narayanan, R., Kurhanewicz, J., hinohara, K., rawford, E. D., imoneau, A., & uri, J. S. "MRI-ultrasound registration for targeted prostate biopsy", IEEE Press, Boston, Massachusetts, USA, pp. 991-994.

National Cancer Institute 2012, *Cancer Trends Progress Report – 2011/2012 Update*, National Cancer Institute, NIH, DHHS, Bethesda, MD.

Neal, R. M. & Hinton, G. E. 1998, "A View of The EM Algorithm That Justifies Incremental, Sparse, and Other Variants," in *Learning in graphical models*, pp. 355-367.

Nocedal, J. & Wright, S. J. 1999, *Numerical Optimization* Springer.

Northern Ireland Statistics and Research Agency 2010, *Registrar General Annual Report 2010*.

Office for National Statistics Mortality Statistics 2011, *Mortality Statistics: Deaths registered in 2010, England and Wales*, Office for National Statistics Mortality Statistics: Deaths registered in 2010, England and Wales. London: National Statistics; 2011.

Oguro, S., Tokuda, J., Elhawary, H., Haker, S., Kikinis, R., Clare, M. C. T., & Hata, N. 2009, "MRI signal intensity based B-Spline nonrigid registration for pre- and intraoperative imaging during prostate brachytherapy", *Journal of Magnetic Resonance Imaging*, vol. 30, no. 5, pp. 1052-1058.

Onik, G. & Barzell, W. 2008, "Transperineal 3D mapping biopsy of the prostate: an essential tool in selecting patients for focal prostate cancer therapy", *Urol.Oncol.*, vol. 26, no. 5, pp. 506-510.

Ourselin, S., Roche, A., Prima, S., & Ayache, N. 2000, "Block Matching: A General Framework to Improve Robustness of Rigid Registration of Medical Images," in *MEDICAL IMAGE COMPUTING AND COMPUTER-ASSISTED INTERVENTION – MICCAI 2000*, 1935 edn, pp. 557-566.

P.D.Sozou, T.F.Cootes, C.J.Taylor, & Di, M. "A non-linear generalisation of PDMs using polynomial regression", BMVA Press, Univ. of York, York, United Kingdom, pp. 397-406.

Papademetris, X., Jackowski, A., Schultz, R., Staib, L., & Duncan, J. 2004, "Integrated Intensity and Point-Feature Nonrigid Registration," in *Medical Image Computing and Computer-Assisted Intervention - MICCAI 2004*, vol. 3216 C. Barillot, D. Haynor, & P. Hellier, eds., Springer Berlin / Heidelberg, pp. 763-770.

Pearson, K. 1901, "On lines and planes of closest fit to systems of points in space", *Philosophical Magazine*, vol. 2, pp. 559-572.

Per-Olof, P. & Strang, G. 2006, "A Simple Mesh Generator in Matlab", *SIAM.Review*, vol. 46, no. 2, pp. 329-345.

Pinkstaff, D. M., Igel, T. C., Petrou, S. P., Broderick, G. A., Wehle, M. J., & Young, P. R. 2005, "Systematic transperineal ultrasound-guided template biopsy of the prostate: three-year experience", *Urology*, vol. 65, no. 4, pp. 735-739.

Pinto, P. A., Chung, P. H., Rastinehad, A. R., Baccala, J., Kruecker, J., Benjamin, C. J., Xu, S., Yan, P., Kadoury, S., Chua, C., Locklin, J. K., Turkbey, B., Shih, J. H., Gates, S. P., Buckner, C., Bratslavsky, G., Linehan, W. M., Glossop, N. D., Choyke, P. L., & Wood, B. J. 2011, "Magnetic Resonance Imaging/Ultrasound Fusion Guided Prostate Biopsy Improves Cancer Detection Following Transrectal Ultrasound Biopsy and Correlates With Multiparametric Magnetic Resonance Imaging", *The Journal of Urology*, vol. 186, no. 4, pp. 1281-1285.

Pizer, S. M., Fletcher, P. T., Joshi, S., Thall, A., Chen, J. Z., Fridman, Y., Fritsch, D. S., Gash, A. G., Glotzer, J. M., Jiroutek, M. R., Lu, C., Muller, K. E., Tracton, G., Yushkevich, P., & Chaney, E. L. 2003, "Deformable M-Reps for 3D Medical Image Segmentation", *International Journal of Computer Vision*, vol. 55, no. 2, pp. 85-106.

Pluim, J. P. W., Maintz, J. B. A., & Viergever, M. A. 2003, "Mutual-information-based registration of medical images: a survey", *Medical Imaging, IEEE Transactions on*, vol. 22, no. 8, pp. 986-1004.

Pondman, K. M., Futterer, J. J., ten, H. B., Schultze Kool, L. J., Witjes, J. A., Hambrock, T., Macura, K. J., & Barentsz, J. O. 2008, "MR-guided biopsy of the prostate: an overview of techniques and a systematic review", *Eur.Urol.*, vol. 54, no. 3, pp. 517-527.

Rangarajan, A., Mjolsness, E., Pappu, S., Davachi, L., Goldman-Rakic, P., & Duncan, J. 1996, "A robust point matching algorithm for autoradiograph alignment," pp. 277-286.

Rathi, Y., Dambreville, S., & Tannenbaum, A. "Statistical shape analysis using kernel PCA", in *Image Processing: Algorithms and Systems, Neural Networks, and Machine Learning*, SPIE, San Jose, CA, USA.

Ravizzini, G., Turkbey, B., Kurdziel, K., & Choyke, P. L. 2009, "New horizons in prostate cancer imaging", *Eur.J.Radiol.*, vol. 70, no. 2, pp. 212-226.

Roche, A., Malandain, G., & Ayache, N. 2000, "Unifying maximum likelihood approaches in medical image registration", *International Journal of Imaging Systems and Technology*, vol. 11, no. 1, pp. 71-80.

Roche, A., Malandain, G., Pennec, X., & Ayache, N. 1998, "The Correlation Ratio as a New Similarity Measure for Multimodal Image Registration," in *MICCAI '98 Proceedings of the First International Conference on Medical Image Computing and Computer-Assisted Intervention*, pp. 1115-1124.

Rueckert, D., Frangi, A., & Schnabel, J. 2010, "Automatic Construction of 3D Statistical Deformation Models Using Non-rigid Registration," pp. 77-84.

Rueckert, D., Sonoda, L. I., Hayes, C., Hill, D. L. G., Leach, M. O., & Hawkes, D. J. 1999, "Nonrigid registration using free-form deformations: application to breast MR images", *Medical.Imaging, IEEE Transactions.on*, vol. 18, no. 8, pp. 712-721.

Sato, Y., Nakajima, S., Atsumi, H., Koller, T., Gerig, G., Yoshida, S., & Kikinis, R. 1997, "3D multi-scale line filter for segmentation and visualization of curvilinear structures in medical images," in *CVRMED-MRCAS'97*, vol. 1205 pp. 213-222.

Scardino, P. T. & Abenhaim, L. L. 2008, "Focal therapy for prostate cancer: analysis by an international panel", *Urology*, vol. 72, no. 6 Suppl, p. S1-S2.

Schmid, D. T., John, H., Zweifel, R., Cservenyak, T., Westera, G., Goerres, G. W., von Schulthess, G. K., & Hany, T. F. 2005, "Fluorocholine PET/CT in Patients with Prostate Cancer: Initial Experience1", *Radiology*, vol. 235, no. 2, pp. 623-628.

Schnabel, J., Rueckert, D., Quist, M., Blackall, J., Castellano-Smith, A., Hartkens, T., Penney, G., Hall, W., Liu, H., Truwit, C., Gerritsen, F., Hill, D., & Hawkes, D. 2001, "A Generic Framework for Non-rigid Registration Based on Non-uniform Multi-level Free-Form Deformations," pp. 573-581.

Scholkopf, B., Smola, A., & Muller, K. R. 1998, "Nonlinear Component Analysis as a Kernel Eigenvalue Problem", *Neural Computation*, vol. 10, no. 5, pp. 1299-1319.

Schouten, M., Bomers, J., Yakar, D., Huisman, H., Rothgang, E., Bosboom, D., Scheenen, T., Misra, S., & F++tterer, J. 2012, "Evaluation of a robotic technique for transrectal MRI-guided prostate biopsies", *Eur Radiol*, vol. 22, no. 2, pp. 476-483.

Shao, W., Wu, R., Ling, K. V., Thng, C. H., Ho, H. S. S., & Cheng, C. W. S. &. N. W. S. 2006, "Evaluation on similarity measures of a surface-to-image registration technique for ultrasound images," in *Medical Image Computing and Computer-Assisted Intervention – MICCAI 2006*, LNCS 4191 edn, Springer, pp. 742-749.

Shen, D., Zhan, Y., & Davatzikos, C. 2003, "Segmentation of prostate boundaries from ultrasound images using statistical shape model", *IEEE Trans.Med.Imaging*, vol. 22, no. 4, pp. 539-551.

Shlens, J. A Tutorial on Principal Component Analysis. 2009.

Si, H. TetGen A Quality Tetrahedral Mesh Generator and Three-Dimensional Delaunay Triangulator V1.4 User's Manual. 2006.

Sim, H. G. & Cheng, C. W. S. 2005, "Changing demography of prostate cancer in Asia", *European Journal of Cancer*, vol. 41, no. 6, pp. 834-845.

Singh, A. K., Kruecker, J., Xu, S., Glossop, N., Guion, P., Ullman, K., Choyke, P. L., & Wood, B. J. 2008, "Initial clinical experience with real-time transrectal ultrasonography-magnetic resonance imaging fusion-guided prostate biopsy", *BJU Int.*, vol. 101, no. 7, pp. 841-845.

Staib, L. H. 1996, "Model-based deformable surface finding for medical images", *IEEE Trans Med Imaging*, vol. 15, no. 5, pp. 720-731.

Staib, L. H. & Duncan, J. S. 1992, "Boundary Finding with Parametrically Deformable Models", *Ieee Transactions on Pattern Analysis and Machine Intelligence*, vol. 14, no. 11, pp. 1061-1075.

Studholme, C., Hill, D. L. G., & Hawkes, D. J. 1999, "An overlap invariant entropy measure of 3D medical image alignment", *Pattern Recognition*, vol. 32, no. 1, pp. 71-86.

Styner, M., Rajamani, K., Nolte, L. P., Zsemlye, G., Szekely, G. Ã., Taylor, C., & Davies, R. 2003, "Evaluation of 3D Correspondence Methods for Model Building," pp. 63-75.

Sung, K. H., In, H. C., Byung, K. H., Ji, H. Y., June, H. H., Seong, J. J., Hyeon, J., Seok-Soo, B., Hak, J. L., & Sang, E. L. 2007, "Impact of Variations in Bony Pelvic Dimensions on Performing Radical Retropubic Prostatectomy", *Urology*, vol. 69, no. 5, pp. 907-911.

Taylor, Z. A., Cheng, M., & Ourselin, S. 2008, "High-speed nonlinear finite element analysis for surgical simulation using graphics processing units", *IEEE Trans.Med.Imaging*, vol. 27, no. 5, pp. 650-663.

Tempany, C., Straus, S., Hata, N., & Haker, S. 2008, "MR-guided prostate interventions", *J Magn Reson Imaging*, vol. 27, no. 2, pp. 356-367.

Thirion, J. P. 1998, "Image matching as a diffusion process: an analogy with Maxwell's demons", *Medical.Image Analysis.*, vol. 2, no. 3, pp. 243-260.

Thompson, S., Penney, G., Buie, D., Dasgupta, P., & Hawkes, D. 2008, "Use of a CT statistical deformation model for multi-modal pelvic bone segmentation," in *Medical Imaging 2008*, 6914 edn, vol. 6914 J. M. Reinhardt & J. P. W. Pluim, eds., SPIE, pp. 6914-1-10.

Tompson, J. C., Wood, J., & Feuer, D. 2007, "Prostate cancer: palliative care and pain relief", *British Medical Bulletin*, vol. 83, pp. 341-354.

Tsai, A., Wells, W., Tempany, C., Grimson, E., & Willsky, A. 2004, "Mutual information in coupled multi-shape model for medical image segmentation", *Med.Image Anal.*, vol. 8, no. 4, pp. 429-445.

Tsai, A., Yezzi, A., Jr., Wells, W., Tempany, C., Tucker, D., Fan, A., Grimson, W. E., & Willsky, A. 2003, "A shape-based approach to the segmentation of medical imagery using level sets", *IEEE Trans.Med.Imaging*, vol. 22, no. 2, pp. 137-154.

Turkbey, B., Albert, P. S., Kurdziel, K., & Choyke, P. L. 2009a, "Imaging localized prostate cancer: current approaches and new developments", *AJR Am.J.Roentgenol.*, vol. 192, no. 6, pp. 1471-1480.

Turkbey, B., Pinto, P. A., & Choyke, P. L. 2009b, "Imaging techniques for prostate cancer: implications for focal therapy", *Nat.Rev.Urol.*, vol. 6, no. 4, pp. 191-203.

Tutar, I. B., Gong, L., Narayanan, S., Pathak, S. D., Cho, P. S., Wallner, K., & Kim, Y. M. 2008, "Seed-based transrectal ultrasound-fluoroscopy registration method for intraoperative dosimetry analysis of prostate brachytherapy", *Med Phys.*, vol. 35, no. 3, pp. 840-848.

Tutar, I. B., Pathak, S. D., Gong, L., Cho, P. S., Wallner, K., & Yongmin, K. 2006, "Semiautomatic 3-D Prostate Segmentation from TRUS Images Using Spherical Harmonics", *Medical Imaging, IEEE Transactions on*, vol. 25, no. 12, pp. 1645-1654.

Umeyama, S. 1991, "Least-squares estimation of transformation parameters between two point patterns", *Pattern.Analysis.and Machine.Intelligence., IEEE Transactions.on*, vol. 13, no. 4, pp. 376-380.

van de Ven, W., Litjens, G., Barentsz, J., Hambrock, T., & Huisman, H. 2011, "Required Accuracy of MR-US Registration for Prostate Biopsies," in *Prostate Cancer Imaging. Image Analysis and Image-Guided Interventions*, 6963 edn, A. Madabhushi et al., eds., Springer Berlin / Heidelberg, pp. 92-99.

Venkataraman, P. 2002, *Applied Optimization with MATLAB Programming* John Wiley & Sons.

Villers, A., Lemaitre, L., Haffner, J., & Puech, P. 2009, "Current status of MRI for the diagnosis, staging and prognosis of prostate cancer: implications for focal therapy and active surveillance", *Curr.Opin.Urol.*, vol. 19, no. 3, pp. 274-282.

Villers, A., Puech, P., Mouton, D., Leroy, X., Ballereau, C., & Lemaitre, L. 2006, "Dynamic contrast enhanced, pelvic phased array magnetic resonance imaging of localized prostate cancer for predicting tumor volume: correlation with radical prostatectomy findings", *J.Urol.*, vol. 176, no. 6 Pt 1, pp. 2432-2437.

Viola, P. & Wells III, W. M. 1997, "Alignment by Maximization of Mutual Information", *International Journal of Computer Vision*, vol. 24, no. 2, pp. 137-154.

Wachinger, C. & Navab, N. 2009, "Alignment of Viewing-Angle Dependent Ultrasound Images," pp. 779-786.

Wang, Y. & Staib, L. H. 2000, "Physical model-based non-rigid registration incorporating statistical shape information", *Medical.Image Analysis.*, vol. 4, no. 1, pp. 7-20.

Watson, G. S. 1983, *Statistics on Spheres* Wiley, New York.

Wei, Z., Ding, M., Downey, D., & Fenster, A. 2005, "3D TRUS Guided Robot Assisted Prostate Brachytherapy," in *Medical Image Computing and Computer-Assisted Intervention MICCAI 2005*, 3750 edn, J. Duncan & G. Gerig, eds., Springer Berlin Heidelberg, pp. 17-24.

Weinreb, J. C., Blume, J. D., Coakley, F. V., Wheeler, T. M., Cormack, J. B., Sotto, C. K., Cho, H., Kawashima, A., Tempany-Afdhal, C. M., Macura, K. J., Rosen, M., Gerst, S. R., & Kurhanewicz, J. 2009, "Prostate cancer: sextant localization at MR imaging and MR spectroscopic imaging before prostatectomy--results of ACRIN prospective multi-institutional clinicopathologic study", *Radiology*, vol. 251, no. 1, pp. 122-133.

Wells III, W. M., Viola, P., Atsumi, H., Nakajima, S., & Kikinis, R. 1996, "Multi-modal volume registration by maximization of mutual information", *Medical Image Analysis*, vol. 1, no. 1, pp. 35-51.

Wilt, T. J., MacDonald, R., Rutks, I., Shamliyan, T. A., Taylor, B. C., & Kane, R. L. 2008, "Systematic Review: Comparative Effectiveness and Harms of Treatments for Clinically Localized Prostate Cancer", *Annals of Internal Medicine*, vol. 148, no. 6, pp. 435-448.

Wu, R. Y., Ling, K. V., & Ng, W. S. 2000, "Automatic prostate boundary recognition in sonographic images using feature model and genetic algorithm", *J.Ultrasound Med.*, vol. 19, no. 11, pp. 771-782.

Wu, R., Ling, K. V., Shao, W., & Ng, W. S. 2003, "Registration of organ surface with intra-operative ultrasound image using genetic algorithm," in *Medical Image Computing and Computer-Assisted Intervention – MICCAI 2003*, LNCS 2878 edn, Springer, pp. 383-390.

Xu, H., Lasso, A., Vikal, S., Guion, P., Krieger, A., Kaushal, A., Whitcomb, L. L., & Fichtinger, G. 2010, "MRI-guided robotic prostate biopsy: a clinical accuracy validation," LNCS 6363 edn, pp. 383-391.

Xu, S., Kruecker, J., Turkbey, B., Glossop, N., Singh, A. K., Choyke, P., Pinto, P., & Wood, B. J. 2008, "Real-time MRI-TRUS fusion for guidance of targeted prostate biopsies", *Computer Aided Surgery*, vol. 13, no. 5, pp. 255-264.

Yang, J. C., Tang, J., Li, J., Luo, Y., Li, Y., & Shi, H. 2008, "Contrast-enhanced gray-scale transrectal ultrasound-guided prostate biopsy in men with elevated serum prostate-specific antigen levels", *Acad.Radiol.*, vol. 15, no. 10, pp. 1291-1297.

Yang, W. Y., Cao, W., Chung, T.-S., & Morris, J. 2005, *Applied Numerical Methods using Matlab* John Wiley & Sons.

Zacharopoulos, A. D. 2005, *Three-dimensional shape-based reconstructions in medical imaging,* PhD Thesis, University College London, United Kingdom.

Zhang, M., Nigwekar, P., Castaneda, B., Hoyt, K., Joseph, J. V., di, S. A., Messing, E. M., Strang, J. G., Rubens, D. J., & Parker, K. J. 2008, "Quantitative characterization of viscoelastic properties of human prostate correlated with histology", *Ultrasound Med.Biol.*, vol. 34, no. 7, pp. 1033-1042.

Zhang, Z. 1994, "Iterative point matching for registration of free-form curves and surfaces", *International Journal of Computer Vision*, vol. 13, no. 2, pp. 119-152.

Zhou, K., Bao, H., & Shi, J. 2004, "3D surface filtering using spherical harmonics", *Computer-Aided Design*, vol. 36, no. 4, pp. 363-375.

Zhuang, X., Gu, L., & Xu, J. 2005, "Medical Image Alignment by Normal Vector Information," in *COMPUTATIONAL INTELLIGENCE AND SECURITY*, vol. 3801 pp. 890-895.

Zienkiewicz, O. C. & Taylor, R. L. 2000, *The Finite Element Method*, 5th edn, Butterworth-Heinemann, Elsevier.

Zitova, B. & Flusser, J. 2003, "Image registration methods: a survey", *Image and Vision Computing.*, vol. 21, no. 11, pp. 977-1000.

Ziyan, U. & Westin, C. F. 2008, "Joint segmentation of thalamic nuclei from a population of diffusion tensor MR images", *Med Image Comput Comput Assist.Interv.Int.Conf.Med Image Comput Comput Assist.Interv.*, vol. 11, no. Pt 1, pp. 279-286.